SuperDARN data simulation, processing, access, and use in analysis of midlatitude convection

Alvaro John Ribeiro

Dissertation submitted to the Faculty of the
Virginia Polytechnic Institute and State University
in partial fulfillment of the requirements for the degree of

Doctor of Philosophy
in
Electrical Engineering

J. Michael Ruohoniemi, Co-Chair
Joseph B. H. Baker Co-Chair
Scott M. Bailey
Gregory D. Earle
Robert W. McGwier
Kevin A. Shinpaugh

October 28, 2013
Blacksburg, Virginia

Keywords: SuperDARN, Radar, Ionosphere, Midlatitude Convection

SuperDARN data simulation, processing, access, and use in analysis of midlatitude convection

Alvaro John Ribeiro

ABSTRACT

Super Dual Auroral Radar Network (SuperDARN) data is a powerful tool for space science research. Traditionally this data has been processed using a routine with known limitations. A large issue preventing the development and implementation of new processing algorithms was the lack of a realistic test dataset. We have implemented a robust data simulator based on physical principles which is presented in Chapter 2. The simulator is able to generate SuperDARN data with realistic statistical fluctuations and known input Doppler velocity and spectral width. Using the simulator to generate a test data set, we was able to test new algorithms for processing SuperDARN data. The algorithms which were tested included the traditional method (FITACF), a new approach using the bisection method (FITEX2), and the Levenberg-Marquardt algorithm for nonlinear curve fitting (LMFIT). FITACF is found to have problems when processing data with high (> 1 km/s) Doppler velocity, and is outperformed by both FITEX2 and LMFIT. LMFIT is found to produce slightly better fitting results than FITEX2, and is thus my recommendation to be the standard SuperDARN data fitting algorithm.

The construction of the new midlatitude SuperDARN chain has revealed that nighttime, quiet-time plasma irregularities with low Doppler velocity and spectral width are a very common ($> 50\%$ of nights) occurrence. Following on previous work, we have conducted a study of nighttime midlatitude convection using SuperDARN data. First, the data are processed into convection patterns, and the results are presented. The drifts are mainly zonal and westward throughout the night. The plasma drifts also display significant seasonal variability. Additionally, a large latitudinal gradient is observed in the zonal velocity during the winter months. This is attributed to processes in the conjugate hemisphere, and possible causes are discussed.

During my graduate studies, we have been part of the development of a software package for enabling and accelerating space science research known as DaViTpy. This software package is completely free and open source. It allows access to several different space science datasets through a single simple interface, without having to write any code for reading data files. It also incorporates several space science models in a single install. The software package represents a paradigm shift in the space science community, and is presented in Appendix A.

The authors thank the National Science Foundation for support under grants ATM-0849031 and ATM-0946900.

Dedication

I would like to thank my parents Alice and Joao for your love and support. I could never have gotten to this point without you. I want to thank Nana, my godparents, and my cousins for everything you have done for me. I would like to thank Allison for all of your support and encouragement.

I want to thank my advisors Mike and Jo for giving me a chance and for all of the help guidance you've given my over the past five years. I would like to thank Pasha for all of the help and advice you've given me over the past few years. I want to thank my lab-mates for always being ready to have our Friday evening group meetings, and for all of the help you're always ready to give me.

I'd like to thank all the rest of my friends and family. I'd like to thank all of the teachers and professors I've had throughout my academic career.

Contents

List of Figures

List of Tables

Attribution

For the first three manuscripts (Chapters 2, 3, and 4), I was the primary researcher as well as the primary author. The fourth manuscript (Appendix A) was a team effort when it came to doing the work, although the majority of it was done my myself and Sebastien de Larquier. The writing of the manuscript was also broken up between us, with myself writing half and Sebastien writing half.

Chapter 1

Introduction

The research which will be presented in this dissertation follows three distinct tracks. The second and third chapters discuss some technical work involving simulation and processing of radar data. The fourth chapter discusses a more scientific topic of midlatitude ionospheric convection patterns derived from SuperDARN data. The fifth chapter describes a software package which was developed during my PhD program, which encompasses space science data and model access/integration and visualization. These three topics all bear on the application of SuperDARN radar data to space science research but are somewhat distinct and will be dealt with in separate sections in this Introduction.

1.1 The Ionosphere

1.1.1 Basic structure and composition

The earth's ionosphere is a layer of weakly ionized plasma starting at about 60 km altitude which envelops the entire planet [*Rishbeth and Garriott*, 1969; *Kelley*, 2009; *Schunk and Nagy*, 2009]. Because it is comprised of charged particles, electric and magnetic effects must be considered in addition to neutral fluid dynamics in order to analyze it. To first order, the ionosphere is horizontally stratified due to gravity. As shown in Figure 1.1, the ionosphere is best organized by plasma density. The ionosphere is generally divided into D (60-90 km), E (90-130 km), and F (above 130 km) regions because each region has distinct characteristics. In the D region, charged particle motions are dominated by collisions with neutral particles. In the E region, ions collide frequently with neutrals, but electrons motions are mostly determined by electromagnetic forces. Because of this, currents can flow in the E region. The F region is generally divided into $F1$ and $F2$ regions. At these altitudes, charged particle motions are mostly electromagnetically driven. In Chapter 4 we will specifically be discussing F region dynamics and thus will focus on the F region in this Introduction. In the presence of an electric field, $\mathbf{E}$, and a magnetic field, $\mathbf{B}$, plasma at F region altitudes and higher drifts at a velocity, $\mathbf{v}$, such that $\mathbf{v} = \mathbf{E} \times \mathbf{B}/B^2$

Figure 1.2 shows the atomic and molecular composition of the ionosphere with altitude. The main source of ionization responsible for creating the ionosphere is photoionization by incoming solar photons which maximizes at local noon [*Rishbeth and Garriott*, 1969; *Kelley*, 2009; *Schunk and Nagy*, 2009]. Another source of ionization, particularly at auroral latitudes, is corpuscular ionization by precipitating charged particles or magnetospheric origin. The

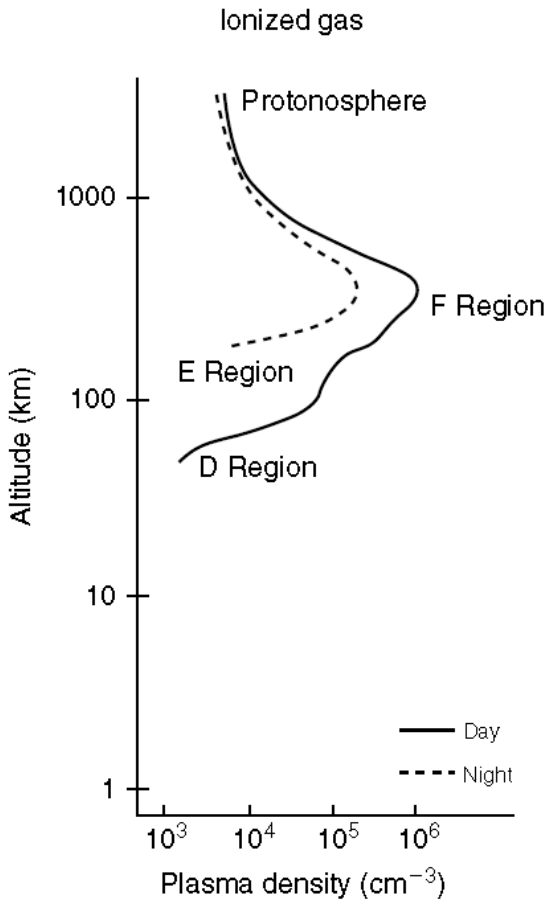

Figure 1.1: A vertical profile of the ionosphere. From *Kelley* [2009]

effects of this process can be seen in Figure 1.3, which shows the spatial distribution of auroral emission and a latitudinal slice of electron density measurements. The auroral oval exists because of charged particles precipitating into the atmosphere. These particles then can then ionize neutrals, and this effect can be seen in the the electron density inset in Figure 1.3.

Ion production and loss in the ionosphere can be modeled using Chapman Theory [*Chapman*, 1931; *Rishbeth and Garriott*, 1969]. Chapman Theory assumes that (I) a beam of monochromatic radiation is incident on (II) a plane, horizontally stratified neutral atmosphere which

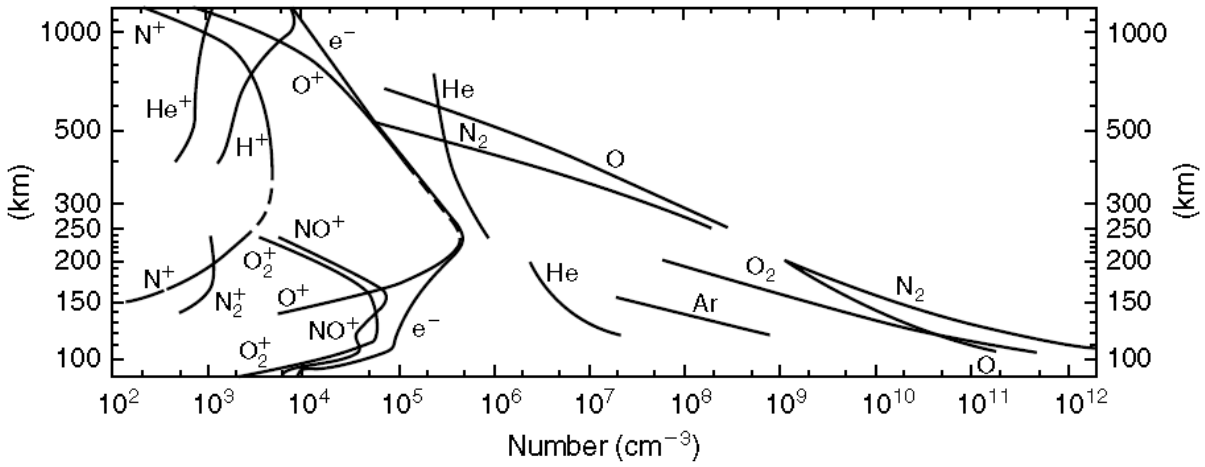

Figure 1.2: Nighttime atomic and molecular composition of the atmospheric temperature (left) and ionospheric plasma density (right) with altitude. The data re from mass spectrometer measurements above White Sands, New Mexico (32° N, 106° W) From *Kelley* [2009]

(III) consists of a single neutral species. The result of Chapman Theory is the Chapman Production Function:

$$q(z,\chi) = \frac{\eta I_\infty}{eH} exp[1 - z - e^{-z} sec\chi] \tag{1.1}$$

where q is the production rate, η is the ionization efficiency, I_∞ is the solar flux at the top of the ionosphere, H is scale height, z is reduced height, and χ is solar zenith angle. A plot of the normalized Chapman Production Function as a function of reduced height is shown in Figure 1.4. The E and $F1$ regions are well approximated as Chapman layers. This is because photoionization is the main production mechanism, and transport processes are not important in these regions. Conversely, in the $F2$ region, transport is an important process, and thus it is not well approximated as a Chapman layer.

In addition to production, ionization must also be lost, or else the neutral atmosphere would eventually disappear. A major loss process is dissociative recombination, which can be

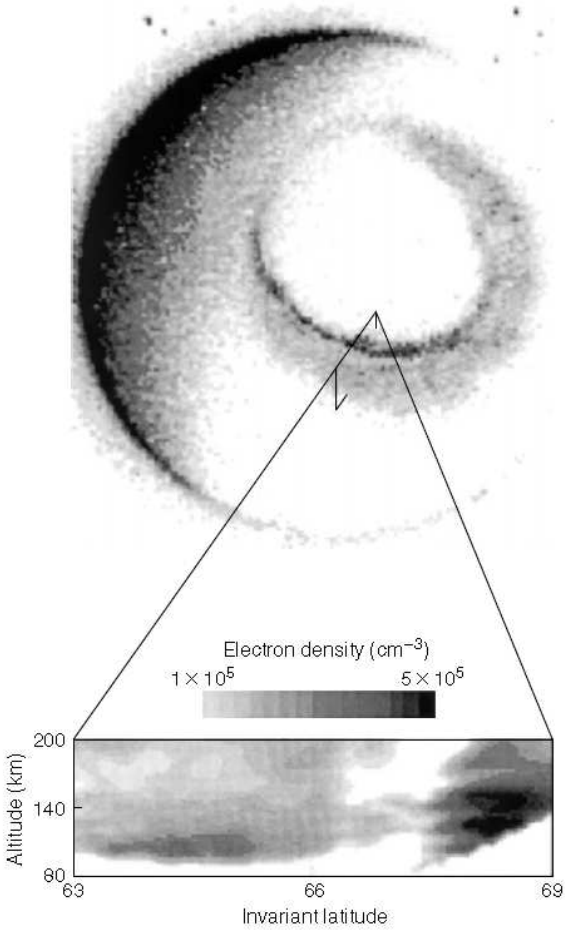

Figure 1.3: An image of the auroral oval taken by the Dynamics Explorer 1 (DE1) satellite. Inset is a plot of a latitudinal slice of electron density measurements gathered from an incoherent scatter radar. Note the correlation between where auroral emission is strongest and where electron density is greatest. From *Kelley* [2009]

described with the equation:

$$e^- + XY^+ \rightarrow X + Y \tag{1.2}$$

where X and Y are arbitrary constituent atoms or molecules [*Kelley*, 2009; *Schunk and Nagy*, 2009; *Rishbeth and Garriott*, 1969]. In dissociative recombination, a free electron recombines with a molecular ion to produce two neutrals. Another type of recombination is

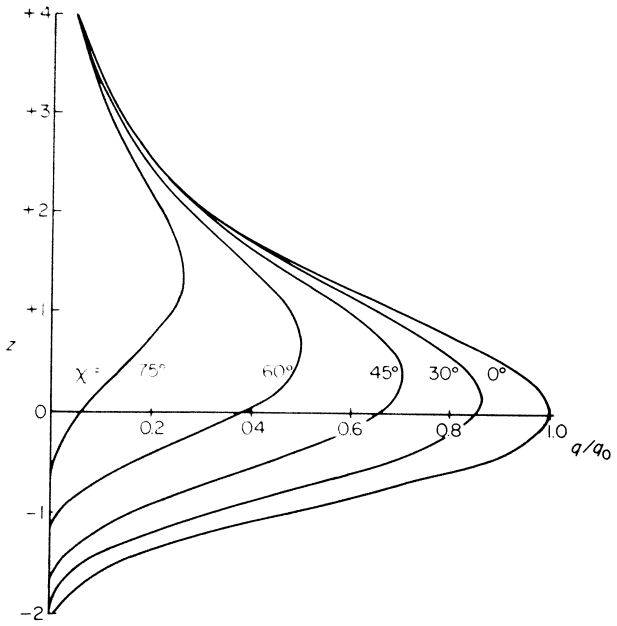

Figure 1.4: A plot of the normalized Chapman Production Function as a function of reduced height. From *Rishbeth and Garriott* [1969].

radiative recombination, which can be described by

$$e^- + X^+ \rightarrow X + h\nu \tag{1.3}$$

where $h\nu$ is a photon, h is Planck's constant, and ν is the frequency of the photon. In radiative recombination, an electron recombines with an ion to create a neutral, and the emission of a photon conserves energy and momentum. Transport of plasma into and out of a volume can also change local ion density. Transport can be described by the divergence term in the continuity equation. Putting together production, loss, and transport, we arrive at the continuity equation

$$\frac{dn}{dt} = P - L - \nabla \cdot (n\mathbf{v}). \tag{1.4}$$

where $\frac{dn}{dt}$ is the rate of change of plasma density in a volume, P is the production term, L is the loss term, n is the plasma density, and $\mathbf{v}$ is vertical ion velocity.

Production, loss, and transport are responsible for the formation of the different ionospheric regions. The distinct layers form because different processes have differing effectiveness at varying altitudes [*Schunk and Nagy*, 2009]. In the E region, photochemistry is dominant, and the principal ions are molecular. In the $F1$ region, photochemistry again dominates, but the prevalent ion is O^+. In the $F2$ region, there is a transition from photochemistry to transport (diffusion) dominance. Above the F region peak, transport processes dominate over photochemistry.

1.1.2 The F Region

The F region is the layer of the ionosphere above about 130 km altitude where the magnetic field dominates charged particle motions [*Rishbeth and Garriott*, 1969; *Schunk and Nagy*, 2009; *Kelley*, 2009]. The F region is typically split into the $F1$ and $F2$ regions. Photochemistry is dominant in the $F1$ region, and thus it is well modeled as a Chapman layer. The $F2$ density peak is also the peak density for the entire ionosphere. Transport processes are important in the $F2$ region, where vertical transport allows plasma to flow from the ionosphere into the plasmasphere during the day, and from the plasmasphere into the ionosphere at night, to help maintain density.

1.1.3 The Midlatitude Ionosphere

The midlatitude ionosphere is a transition region between the auroral region which has mainly vertical field lines and the equatorial region which has mainly horizontal field lines [*Rishbeth and Garriott*, 1969; *Schunk and Nagy*, 2009; *Kelley*, 2009]. At midlatitudes, the earth's magnetic field makes an angle of around 45° with the terrestrial surface (dip angle),

and thus, the combined effects of electric fields, neutral winds, gravity, and pressure gradients are more complicated when analyzing plasma dynamics in the region.

During the day, photochemistry dominates the plasma profile in the E and F regions [*Rishbeth and Garriott*, 1969; *Schunk and Nagy*, 2009; *Kelley*, 2009]. The plasma density begins to increase in the E region, and reaches a peak in the F region at about 300 km. This is due to a combination of production, loss, and transport processes. In the inner magnetosphere, the closed magnetic field lines which have footpoints in the midlatitude ionosphere act as a reservoir for dense plasma, and this is called the plasmasphere. The plasmasphere is bounded by the plasmapause, which is indicated by a sharp decrease in plasma density with altitude. This can be seen at $R_e = 4$ in Figure 1.5, which shows the average equatorial electron density profile. The plasmapause separates the region where flux tubes approximately corotate with the earth from the auroral region which has convection driven by magnetospheric sources.

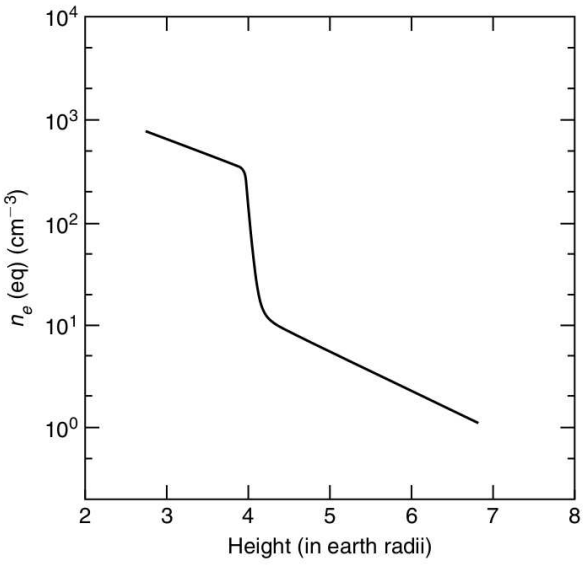

Figure 1.5: Average plasmasphere equatorial electron density profile versus altitude. From *Kelley* [2009], after *Angerami and Carpenter* [1966].

Ionospheric plasma at midlatitudes must, to first order, corotate with the earth [*Kelley*,

2009]. If the plasma did not corotate, there would be a neutral wind, $\boldsymbol{U_R}$ in the nonrotating plasma frame. This wind would drive an electric current, $\boldsymbol{J} = \boldsymbol{\sigma} \cdot (\boldsymbol{U_R} \times \boldsymbol{B})$, where $\boldsymbol{\sigma}$ is the conductivity. This current is not divergence free because conductivity varies with altitude, and thus an electric field would build up until the current vanished, which happens when the plasma $\boldsymbol{E} \times \boldsymbol{B}$ drifts at the same velocity as the rotation speed of the earth.

Of particular interest in the context of this dissertation are the electric field-driven plasma flows in the earth-fixed reference frame, because these flows are measured by ground-based radars such as SuperDARN. SuperDARN in fact measures plasma flows that are due to non-corotation. *Kelley* [2009] compares these flows to neutral winds in atmospheric weather, because they are also measured in the rotating frame. The main driver of these plasma flows at midlatitudes is the dynamo action of the neutral wind. The basic idea behind dynamo theory is as follows: (I) neutral winds drive currents in regions with appreciable conductivity which (II) are not divergence-free because of spatial variability in conductivity. (III) Electrostatic fields are set up to modify the flow of current, which, (IV) map along magnetic field lines due to their high parallel conductivity [*Rishbeth and Garriott*, 1969]. Large scale electric fields map along magnetic field lines with little attenuation [*Kelley*, 2009].

1.2 Radar

1.2.1 Background

The word radar is an acronym for **Ra**dio **D**etection **A**nd **R**anging. Thus, at its most basic, a radar is a system whose purpose is to detect and locate "targets" [*Skolnik*, 2001]. The

nature of the target varies depending on the application, but some typical examples include aircraft, cars, and weather. In the case of this dissertation, the targets are ionospheric plasma irregularities in the E and F regions of the ionosphere. What exactly these are will be discussed later in the chapter.

A radar works by transmitting a signal from an antenna and then listening for a reflected return signal [*Skolnik*, 2001]. Typically, the signal which is transmitted is a pulse of electromagnetic radiation. This process is illustrated in Figure 1.6. Assuming the speed of propagation is the speed of light, c, one can then time the delay between transmission and reception, and determine the range to the target as:

$$R = \frac{cT_r}{2} \tag{1.5}$$

where T_r is the time delay between transmission and reception, and the factor of two takes account of travel to the target and back. One cannot gather much information from a single radar pulse, such as whether a target is moving or not, and thus sequential pulses are emitted at some time interval, T_p. In this case, the maximum unambiguous range is:

$$R_{un} = \frac{cT_p}{2}. \tag{1.6}$$

Besides ranging targets, many radars are also capable of determining the Doppler velocity of targets. When the electromagnetic wave emitted by the radar is incident on a moving target, that target imparts a Doppler shift on the frequency of the reflected signal. This occurs because the reflected waveform is either compressed (motion towards the radar) or spread out (motion away from the radar) by a moving target. Doppler frequency, f_d is

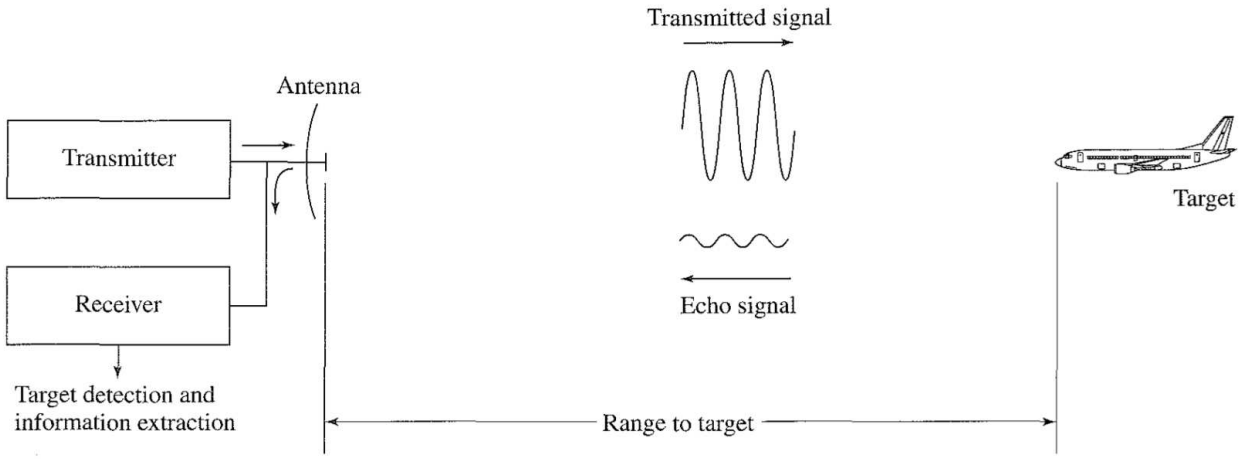

Figure 1.6: A simple illustration of how a radar works. From *Skolnik* [2001]

defined as:

$$f_d = \frac{2v_r}{\lambda} \tag{1.7}$$

where v_r is the radial velocity of the target, and λ is the transmit wavelength.

As was noted previously, for a radar to have a large maximum unambiguous range, it must also have a long inter-pulse period. This is because a reflected sample from the maximum range or the radar must be given time to return to the antenna before the next pulse is sent out. However, in order to measure large Doppler velocities, it must have a short inter-pulse period. Specifically, samples must be recorded at twice the maximum Doppler frequency, known as the Nyquist frequency. The reason for this is illustrated in Figure 1.7. In this figure, the top curve represents the received Doppler signal. The oversampling line shows that the signal can be easily recovered if sampling is performed at more than twice the Doppler frequency. The Nyquist frequency plot shows the minimum sampling frequency which is required to recover the original signal. The undersampling plot shows a regime in which sampling is performed too slowly to recover the original signal.

Note that if a radar is made to detect targets at large ranges from the radar, traveling at

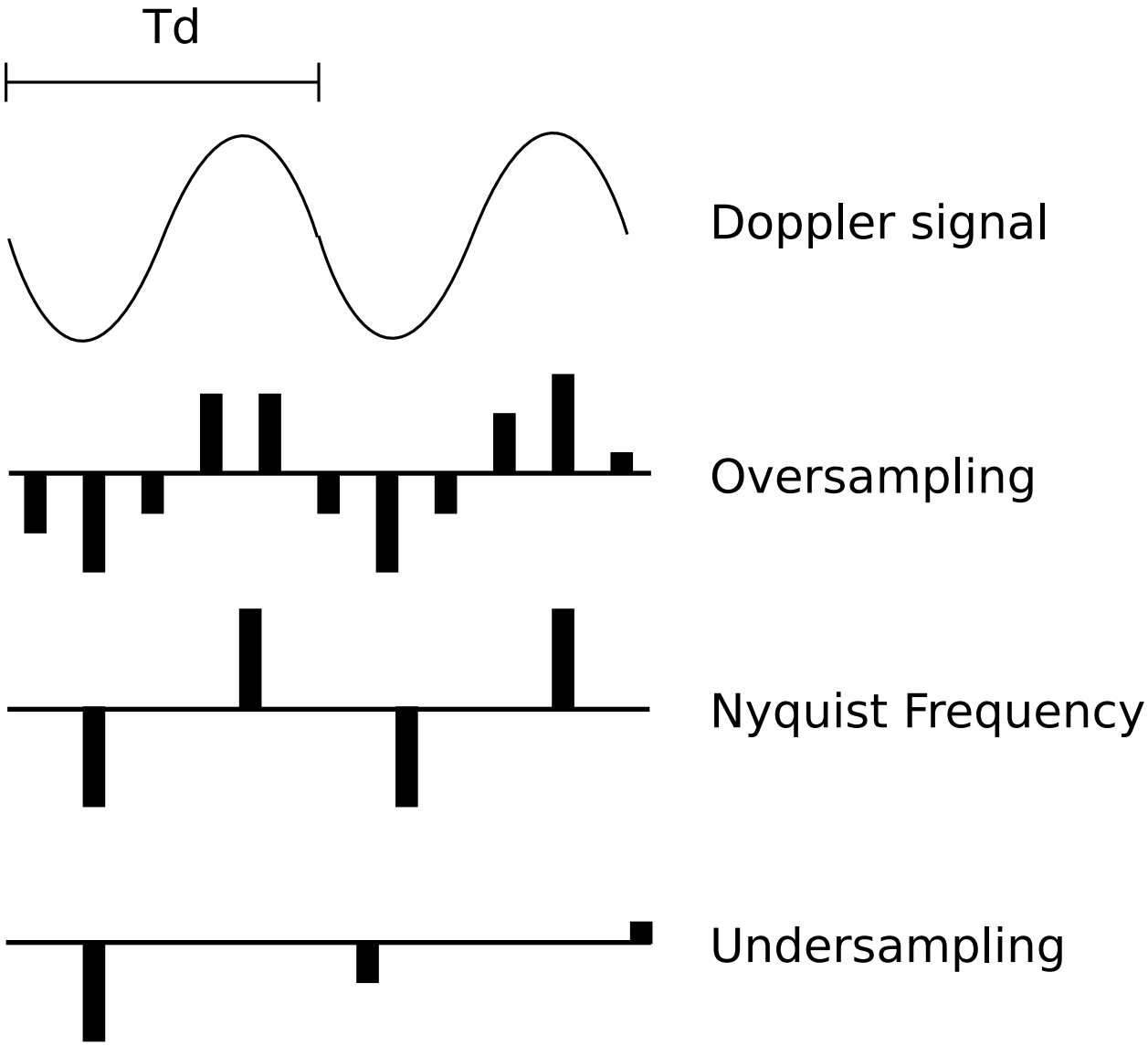

Figure 1.7: An illustration which demonstrates the complexity of sampling a Doppler signal. The top curve shows the signal itself. The second line shows an example of oversampling where the returned signal is easily recovered. the second line plot shows sampling at the Nyquist frequency, which is the minimum frequency required for recovering the signal. The third line plot illustrates sampling at a frequency which is much less than the Doppler frequency, and the signal cannot be recovered.

large Doppler velocities, there are mutually exclusive requirements imposed on the inter-pulse separation. This is precisely the case with SuperDARN radars. In order to solve this problem, the radars use what is known as a multi-pulse sequence. Multi-pulse sequences will

be discussed in the next section as well as in Chapters 2 and 3.

1.2.2 SuperDARN Radars

The Super Dual Auroral Radar Network (SuperDARN) is an international network of high-frequency (HF, 8-20 MHz) radars which monitor plasma convection at E and F region heights [*Greenwald et al.*, 1985; *Chisham et al.*, 2007]. The radars operate at HF in order to take advantage of refraction in the ionosphere to gain access to backscatter from ionospheric irregularities and maximize the range of the radars. Refraction occurs because there is a gradient in electron density, and thus refractive index, in the ionosphere. This is illustrated in Figure 1.8. Note how some rays (gray lines) are capable of being refracted from the ionosphere, to the terrestrial surface, and back to the ionosphere. Returns from the earth's surface are called "ground scatter", and returns from the ionosphere are referred to as "ionospheric scatter". SuperDARN antennas are arranged in of phased arrays which can be electronically steered in 16-24 look directions (beams) separated by 3.24° of azimuth and obtain backscatter from 75-100 range gates along each beam with a separation of 45 km.

SuperDARN receivers utilize both an in-phase (I), and quadrature (Q) component. That is, a received signal is split into two signals, and one of them is phase shifted by 90 degrees.In order to resolve targets at large distances unambiguously, one requires a long inter-pulse period so that the signal from a target at the maximum desired distance has returned before the next pulse is transmitted. In order to resolve velocities of up to 2 km/s at a range of up to 4000 km (which impose mutually exclusive restrictions on the inter-pulse separation, T_p) the radars utilize multi-pulse sequences (e.g., Figure 3.2). By combining returns from the same range gate from different pulses, one can generate an autocorrelation function (ACF), as seen in Figure 1.9. The phase shift between lags of the ACF is used to solve for the

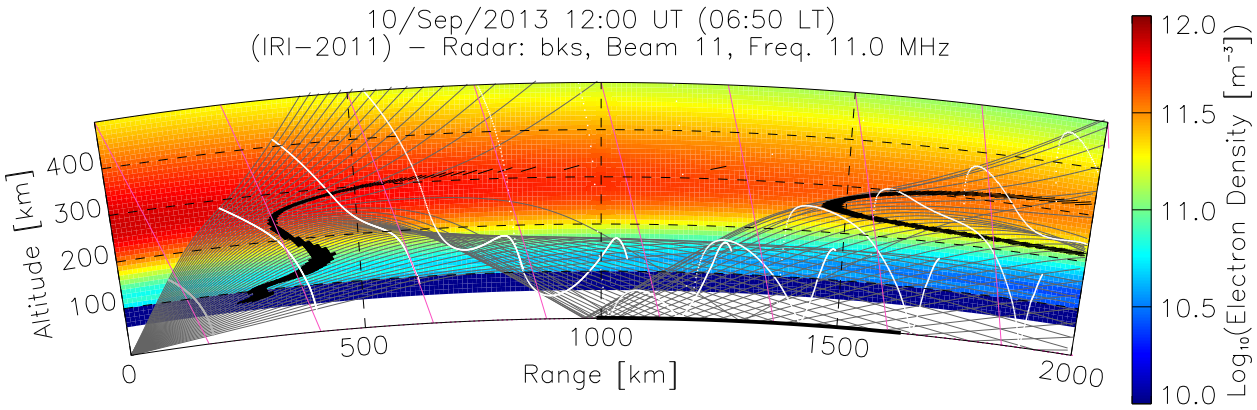

Figure 1.8: A ray-tracing plot for the Blackstone, VA radar. The gray lines represent the radar rays. The ionosphere is color-coded by electron density, according to the International Reference Ionosphere (IRI) Model. The pink lines represent the earth's magnetic field, and the black sections represent the locations where the rays are approximately orthogonal to the magnetic field (the condition for backscatter from ionospheric irregularities). Note how the radar utilizes refraction to increase the maximum range of the radar. Figure courtesy of Sebastien de Larquier.

Doppler velocity of the target according to (1.8).

$$V_D = \frac{\lambda}{4\pi}\frac{\delta\phi}{\delta\tau} \tag{1.8}$$

In this equation, λ is the radar wavelength, and $\frac{\delta\phi}{\delta\tau}$ is the phase shift between lags of the ACF. The decay of signal amplitude with time is used to solve the spectral width as shown in (1.9).

$$W = \frac{\lambda}{2\pi t_d} \tag{1.9}$$

In this equation, λ is the radar wavelength, and t_d is the e-folding time of the amplitude of the ACF. More information about SuperDARN data sampling and processing can be found in Chapters 2 and 3 as well as *Sterne* [2010].

The primary backscatter targets of SuperDARN radars are ionospheric plasma irregularities in the E and F regions of the ionosphere. These ionospheric irregularities are structures in

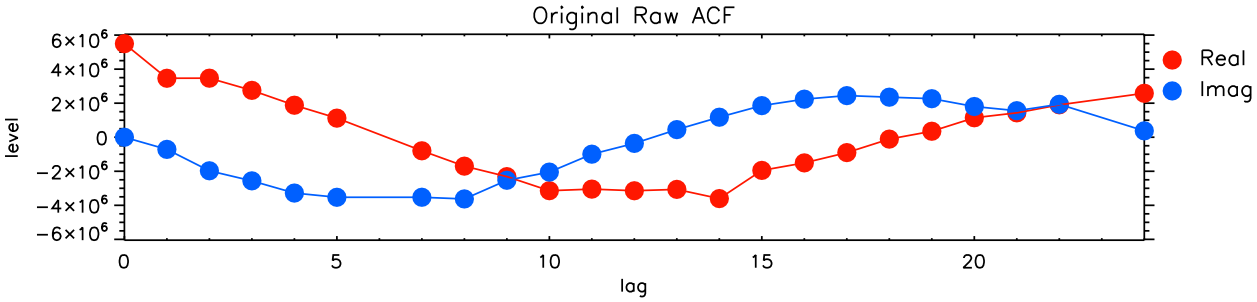

Figure 1.9: An example of a SuperDARN ACF. The data are from beam 10, range gate 18 of the east array of the Fort Hays, Kansas radar, from 17 March 2013 at 10 UT.

ionospheric plasma density which are amplified by instability processes [*Fejer and Kelley*, 1980; *Keskinen and Ossakow*, 1983; *Tsunoda*, 1988]. They can range in spatial scale from centimeters up to kilometers. An important factor in the growth or damping of irregularities are electric fields. At high latitudes, the dominant F region instability process is thought to be the Gradient Drift Instability, which occurs when an electric field acts on a plasma with a gradient in plasma density [*Baker et al.*, 1986; *Hosokawa et al.*, 2001]. At midlatitudes, it has been suggested that a possible instability process is the Temperature Gradient Instability (TGI), which occurs when there are opposing temperature and density gradients within a plasma [*Hudson and Kelley*, 1976; *Greenwald et al.*, 2006].

1.3 Software Development

Appendix A focuses on the development of a software package for space science research, and so it is appropriate here to give some background on how this came about. SuperDARN has historically used a centralized single programmer model for software development. Effectively, this meant one person was responsible for writing/maintaining all of the code, fixing bugs, providing documentation and support, etc. Additionally, when a bug got fixed, users were required to wait for a major release (once or twice a year) to actually get the fix.

Much of the analysis and most of the visualization of SuperDARN data has traditionally been done using the Interactive Data Language (IDL[1]), which is closed source and has an expensive license. As SuperDARN continued to grow, the single programmer model and the use of non-free software became increasingly problematic and cumbersome.

In 2012, it was decided to try and remedy the situation by developing a new software library, called DaViTpy (**Da**ta **Vi**sualization **T**oolkit-**Py**thon. Throughout the project the freedoms outlined in the Free Software Definition[2] have been adopted. These freedoms are as follows:

0 The freedom to run the program for any purpose.

1 The freedom to study how the program works, and change it to make it do what you wish.

2 The freedom to redistribute copies so you can help your neighbor.

3 The freedom to improve the program, and release your improvements (and modified versions in general) to the public, so that the whole community benefits.

Essentially, the goal has been to start a software project which would ultimately become a community-developed, open source (100% free) software environment for SuperDARN (and space science in general) data access and analysis. In addition, a primary aim is to streamline and simplify data access and make bug-fixes and updates an almost immediate process. This topic is discussed in depth in Appendix A.

[1] http://www.exelisvis.com/ProductsServices/IDL.aspx
[2] http://www.gnu.org/philosophy/free-sw.html

1.4 Dissertation Organization

SuperDARN is a powerful tool for space science research. Since 2004, there have been over 500 publications using SuperDARN data. On its own, it provides a continuous global picture of ionospheric plasma convection. The measurements can be used to derive convection patterns and solve for cross polar cap potential, as seen in Figure 1.10. It is also a valuable tool in collaboration with other measurements. SuperDARN data is readily used with satellite data, such as DMSP data as seen in Figure 1.10. In this figure, the black traces show DMSP drift meter measurements, and the colored dots show electron energy flux. Additionally, SuperDARN data can be combined with measurements from other radar systems. For example, *Greenwald et al.* [2006] used midlatitude SuperDARN measurements in conjunction with incoherent scatter radar data to examine instability processes.

At its most fundamental level, the SuperDARN data product begins with fitting the ACFs which are calculated from receiver voltages in order to solve for Doppler velocity and spectral width. This is a crucial step which makes all of the space science research which is done with SuperDARN possible. This fitting has traditionally been done with a routine called FITACF, which was developed over 20 years ago, at a time when computer speed and storage presented a serious issue. This algorithm has remained in use since its inception, despite having known shortcomings (discussed in Chapter 3). One of the reasons for this was the lack of a reliable, realistic test dataset for comparing different processing algorithms. We have developed a realistic SuperDARN data simulator, based on physical principles, which is able to generate a realistic, reliable test data set with known Doppler velocity and spectral width parameters. The data simulator is discussed in a paper which was published in Radio Science in 2013, and is presented here in manuscript form as Chapter 2.

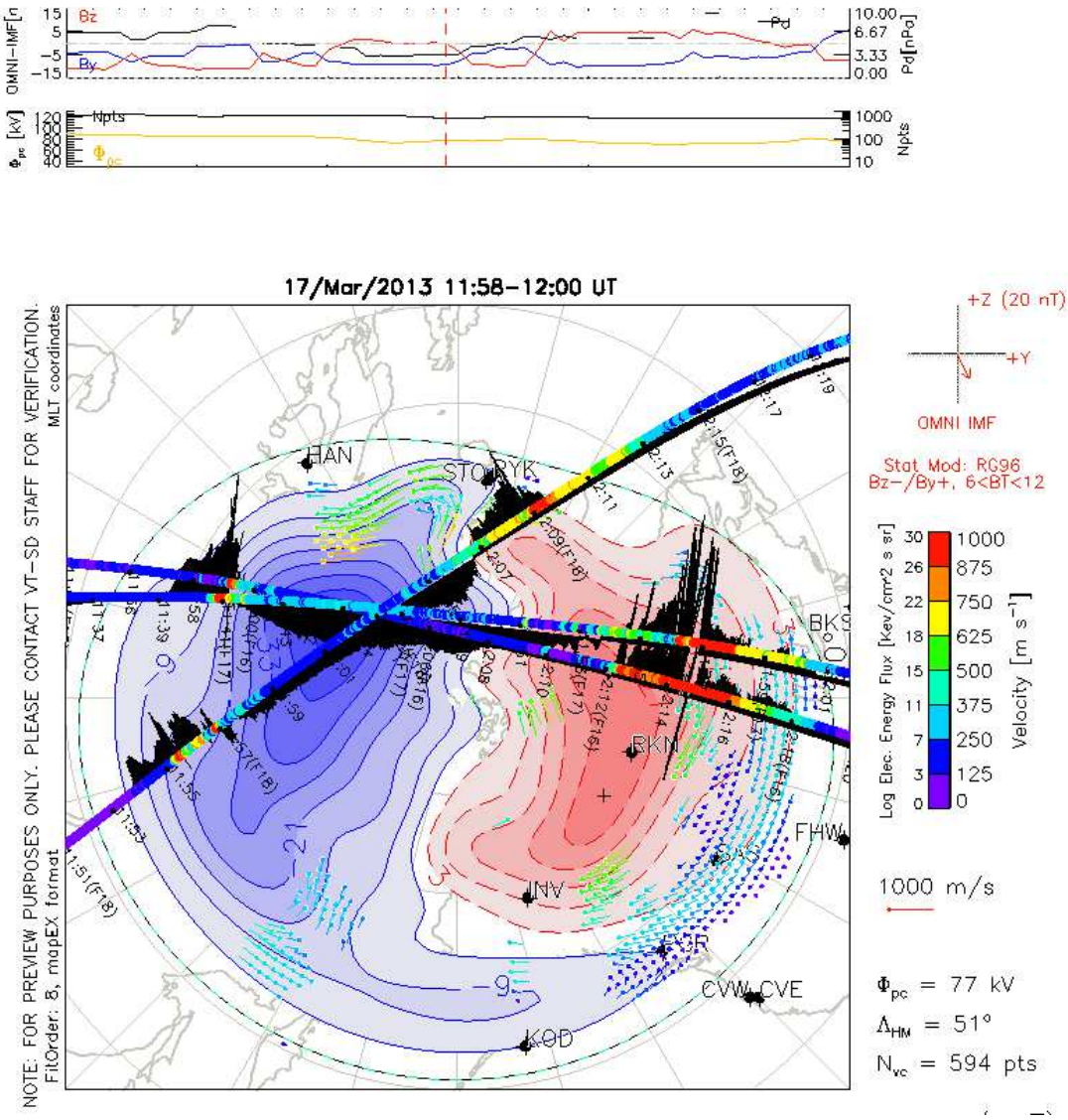

Figure 1.10: A SuperDARN convection map showing fitted convection contours. The vectors shows fitted two-dimensional plasma flows. The blacks traces shows DMSP drift meter data. the colored dots show DMSP electron energy flux measurements.

The development and implementation of new data processing algorithms coupled with the generation of a test data set allowed for the comprehensive testing of new ACF fitting algorithms. We found that the shortcomings of FITACF could indeed be overcome using new processing routines, and the results were presented in a paper which was published in Radio Science in 2013. This paper is presented in this dissertation as Chapter 3.

The SuperDARN midlatitude radar chain was originally constructed in order to provide coverage of the expanded auroral oval during storm times. However, soon after construction, it was noted that low velocity quiet time plasma irregularities were quite frequent. Some early studies of these irregularities include *Greenwald et al.* [2006] and *Baker et al.* [2007]. A problem with these irregularities was that their low Doppler velocity and spectral width made them difficult to distinguish from ground backscatter in an automated way. *Ribeiro et al.* [2011] developed an automated algorithm which could reliably identify these ionospheric events in a reliable way. Following this, *Ribeiro et al.* [2012] performed a study in which they discussed the occurrence characteristics of these F region plasma irregularities. *de Larquier et al.* [2013] followed with a study of the spatial distribution of the irregularities. Building on this previous work, we present a study of convection patterns derived from the drift characteristics of these plasma irregularities. This work is described in a manuscript which is currently under preparation to be submitted to the Journal or Geophysical Research in late 2013, and is presented in this dissertation as Chapter 4.

As the technological world has progressed in the information age, the space science community has been slow to adapt and adopt new technologies. Instead of accelerating and facilitating scientific research and collaboration, the current data sharing paradigm can hinder and stifle it. Too often, data is difficult to get. Sometimes, a researcher must contact an individual PI to get data. Other times data is housed on a remote server, with little documentation of what the files contain. Yet other times, data may be accessible through a web interface, but gathering large quantities of data can be a hassle. The graduate students an the VT SuperDARN Lab envisioned a software package which would allow for painless access to diverse scientific datasets. From this idea grew a software package known as the DaViTpy. In addition to data access tools, several models have been integrated into the package, and visualization software has been implemented. The software package has gotten

contributions from several different people, but the vast majority of the coding work to this point has been done by Sebastien de Larquier and myself. We are currently preparing a manuscript describing DaViTpy, and it is presented here as Appendix A.

Chapter 2

A realistic radar data simulator for the Super Dual Auroral Radar Network

A. J. Ribeiro,[1] P. V. Ponomarenko,[2] J. M. Ruohoniemi,[1] J. B. H. Baker,[1] L. B. N. Clausen,[3] R. A. Greenwald,[1] and S. de Larquier[1]

1: The Bradley Department of Electrical and Computer Engineering, Virginia Tech, Blacksburg, Virginia, USA.

2: Institute of Space and Atmospheric Studies, University of Saskatchewan, Saskatoon, Saskatchewan, Canada.

3: Institute for Geophysics and Extraterrestrial Physics, TU Braunschweig, Germany.

Abstract

The Super Dual Auroral Radar Network (SuperDARN) is a chain of HF radars for monitoring plasma flows in the high and mid latitude E and F regions of the ionosphere. The targets of SuperDARN radars are plasma irregularities which can flow up to several kilometers per second and can be detected out to ranges of several thousand kilometers. We have developed a simulator which is able to model SuperDARN data realistically. The simulation system is composed of four separate parts: model scatterers, model collective properties, a model radar, and post-processing. Importantly, the simulator is designed using the collective scatter approach which accurately captures the expected statistical fluctuations of the radar echoes. The output of the program can represent either receiver voltages or autocorrelation functions (ACFs) in standard SuperDARN file formats. The simulator is useful for testing and implementation of SuperDARN data processing software and for investigation of how radar data and performance change when the nature of the irregularities or radar operation varies. The companion paper demonstrates the application of simulated data to evaluate the performance of different ACF fitting algorithms. The data simulator is applicable to other ionospheric radar systems.

2.1 Introduction

The Super Dual Auroral Radar Network (SuperDARN) is an international network of HF (8-20 MHz) radars monitoring plasma dynamics at middle to high latitudes in both the northern and southern hemispheres [*Greenwald et al.*, 1985; *Chisham et al.*, 2007]. The radars coherently detect via Bragg scattering decameter-scale irregularities in the plasma density distribution in the E and F regions of the ionosphere. A conventional SuperDARN radar has 16 look directions, or beams, separated by 3.24° in azimuth. Each beam sounding counts 75-100 range gates. The spatial extent of the range gates is determined by the radar sample separation, and is typically 45 km, although other values such as 15 or 30 km are common. The radars use a multipulse sequence in order to simultaneously satisfy requirements of the maximum range of values for target Doppler velocity and range. [*Greenwald et al.*, 1985; *Hanuise et al.*, 1993; *Baker et al.*, 1995; *Barthes et al.*, 1998; *Ponomarenko and Waters*, 2006]. Plasma irregularities are routinely detected at ranges of hundreds to several thousand kilometers and have speeds of hundreds of meters per second. An autocorrelation function (ACF), from which parameters such as Doppler velocity are determined, is calculated for each range gate using the instant receiver samples (voltages). The dwell (integration) time on a particular beam, t_{int}, is typically 3-7 seconds. An overall transmit/receive time for a single pulse sequence is typically 100 ms so that in a single integration period 30-70 pulse sequences are integrated. For each range gate, the arrival time of returns from each pulse in the sequence is calculated and receiver samples from pulse pairs are multiplied in order to generate the complex ACF values at the time lag set by the delay between the pulses. These products are averaged over the integration time to produce an average ACF. Besides increasing the signal-to-noise ratio (SNR) by suppressing noise fluctuations, the averaging also lowers the interference from undesired ranges (cross-range interference, CRI,

for more detail see *Ponomarenko and Waters* [2006]). Analytical functions are fitted to the variation in ACF power and phase with lag time to estimate Doppler velocity, spectral width, and backscatter power. The performance of different methods for performing this fitting is considered in the companion paper, [*Ribeiro et al.*, 2013a].

In order to assess fitting algorithms quantitatively, it is desirable to be able to perform the fitting on modeled radar data with tunable input parameters and realistic statistical characteristics. There have been several attempts to design such a simulator for SuperDARN applications [*André et al.*, 1999; *Ponomarenko et al.*, 2008]. The latest effort by *Ponomarenko et al.* [2008] was based on the collective scatter approach and considered a single range gate with a combination of ionospheric scatter, ground scatter, and external noise components. This work represents a further development of the collective scatter approach. The improved model includes multiple range gates, accounts for CRI and pulse-overlap interference (which results from blanking the receiver during transmission) and generates output either as averaged ACFs or instant receiver voltages. It also contains physical justification and detailed description of the basic radar simulator which were only briefly mentioned in *Ponomarenko et al.* [2008]. The simulator is coded in the C programming language and has been thoroughly tested. While it is designed to analyze SuperDARN-specific fitting algorithms, as described in the companion paper *Ribeiro et al.* [2013a], the software can also be adapted to simulate operation of other types of backscatter radars.

2.2 Physical Justification for the Backscatter Model

In testing radar data processing software, it is crucial to be able to simulate the test dataset realistically. With respect to SuperDARN applications, this amounts to simulating iono-

spheric backscatter signals (ACFs). It is easy to generate an ideal ACF with pre-determined magnitude (SNR, or "power"), phase variation (Doppler shift), and decorrelation time (spectral width). However, this sort of modeling does not provide objective information on the measurement errors which are mostly determined by (i) external noise and (ii) statistical fluctuations of the signal itself. While modeling of the external noise/interference is relatively straightforward, a realistic description of the signal's statistics requires special attention. A simple way to "randomize" an ideal ACF is to add a "noise" ACF component that can be generated from "white" or "colored" noise, but that approach lacks clear physical justification. For a more adequate description of the statistical variability of the radar echoes, one has to adopt a realistic model of the scatterers, i.e., electron density irregularities. On average, the ionospheric irregularities are relatively weak $\langle \delta N_e^2 / N_e^2 \rangle << 1$ where N_e is the electron density and δ represents a perturbation, so that most of the wave power penetrates through the plasma with only a small portion scattered back to the receiver. The average backscatter field at the reception point can then be adequately described by the single-scatter approximation (e.g., *Rytov et al.* [1988]), where each point of the scattering volume represents a discrete source of an elementary field

$$A(r,t) = |A(r,t)| e^{j\phi(r,t)} \tag{2.1}$$

where $j = \sqrt{-1}$, amplitude is proportional to the magnitude of the local electron density fluctuations, $|A(r,t)| \propto \delta N_e(r,t)$, and phase is defined by $\phi(r,t) = -(\omega t + \mathbf{k} \cdot \mathbf{r})$, where ω and $\mathbf{k}$ are the angular frequency and wave vector associated with the radar signal and $\mathbf{r}$ is the total path followed by the ray. The resulting field at the radar location then results from summation of the individual fields generated by the sources confined to the effective scattering volume (range gate). Statistical properties of the scattered field arise from the

spatio-temporal variability of the individual fields, $A(r,t)$, which are discussed in the following sections.

2.3 Implementation of the simulator

Operation of the simulator can be divided into four basic components (i) individual scatterer, (ii) collective properties, (iii) radar operation, (iv) post-processing.

2.3.1 Individual Scatterer Model

The fundamental elements of the simulator are the model scatterers. For this application, a scatterer is a point in space which reflects the radar signal. The behavior of scatterers is based on the model proposed by *Moorcroft* [2004]. Each scatterer, i, has a random time of appearance within a designated integration period that begins at time t_{app_i}. For testing purposes, we also introduce an option to designate a finite scatterer lifetime, t_{life_i}. This parameter is consistent with experimental observations from *Ponomarenko et al.* [2007]. This results in "boxcar" scatterers with constant amplitude, i.e.,

$$|A_{max}(t)| = \begin{cases} 1 \quad if \quad (t_{app_i} \leq t < t_{app_i} + t_{life_i}) \\ 0 \quad if \quad (t < t_{app_i}, t > t_{app_i} + t_{life_i}) \end{cases} \tag{2.2}$$

The lifetime distribution of the scatterers can be set to either constant or exponential, i.e., $t_{life_i} = t_c$ in the former case and $t_{life_i} = |t_c * ln(x)|$ (where x is a uniformly distributed random variable between 0 and 1) in the latter case. In the future, it would be easy to introduce

other models for the lifetime distribution of scatterers. The user inputs the constant t_c and chooses the distribution. Table 2.1 lists all of the user inputs to the simulator. Note that if t_c is set to a large value compared to the duration of an integration period, the scatterers will effectively have infinite lifetimes. The last step in initializing the model scatterers is to give each one a noise-like random velocity in the line-of-sight direction drawn from a Gaussian distribution, designated as v_{g_i}. Note that this velocity is distinct from the bulk drift velocity, which will be discussed in the following section. In reality, there is little evidence for these velocity fluctuations, but we have included them in the model for completeness [*Villain et al.*, 1996]. The standard deviation of the distribution of the random velocity fluctuations, σ_{v_g} is set by the user and can be assigned separately to each range gate. If the user sets this value to 0, random velocity fluctuations will not exist in the model.

2.3.2 Collective Behavior Model

The next step in the simulation is to integrate individual scatterers into a collective behavior model which determines statistical characteristics of the radar returns produced by the scatterers confined to a range gate. For this application, we consider a collection of a large number (n = 2000) of elementary scatterers within a single range gate with linear dimension Δr. The number of scatterers was chosen as a trade-off between model validity and computing time. Each scatterer is assigned an initial position in two-dimensional space at a range r_i from the radar, which is selected randomly within the parent range gate such that $r_g \leq r_i \leq r_g + \Delta r$ where r_g is the distance to the front edge range gate. We also assume that backscatter comes from the far zone, $\Delta r/r << 1$, so that we can neglect the difference in the geometrical decay factor for scatterers within a single range gate.

We also use the collective behavior model to deal with characteristics which are common to

Table 2.1: List of user inputs to the simulator

Name	**Scalars** Description	
$freq$	radar frequency	
$noise\_flg$	flag to indicate if noise is included	
$noise\_lev$	white noise level	
N_{avg}	number of ACFs to integrate	
N_{rang}	number of range gates	
$lagfr$	distance to first range gate in samples	
$life\_dist$	flag indicating lifetime distribution of scatterers	
$smsep$	sample separation	
N_{pul}	number of pulses in pulse sequence	
$mpinc$	smallest interpulse separation	
cri_flg	flag indicating whether to include CRI	
Name	**Arrays** Description	Number of Elements
	Scatterer Properties	
t_c	disappearance time constant	N_{rang}
σ_{v_g}	std. dev. of Gaussian velocity fluctuations	N_{rang}
	Collective Properties	
t_d	irregularity decay time	N_{rang}
t_g	irregularity growth time	N_{rang}
v_d	line-of-sight velocity	N_{rang}
	General	
amp_0	amplitude factor of ACFs	N_{rang}
$qflg$	flag indicating if a range gate contains backscatter	N_{rang}
$pulse\_t$	pulse table	N_{pul}

all scatterers within a range gate. In general, the electron density fluctuations associated with ionospheric plasma irregularities are characterized by amplitude decay due to some kind of dissipation process, e.g., plasma diffusion. In our simulator, this is modeled through a combination of exponential growth and decay times, t_g and t_d, respectively. It is worth noting that these two parameters are unrelated to the "boxcar" lifetime property discussed previously. This results in a reflected signal amplitude from the ith scatterer in a range gate at time t of

$$A_i(t) = |A_{max}(t)|(1 - e^{-(t-t_{app_i})/t_g}) * e^{-(t-t_{app_i})/t_d} \tag{2.3}$$

where the $|A_{max}(t)|$ forces the amplitude to 0 outside of the scatterer lifetime, consistent with (2.2).

Another characteristic which is shared by all scatterers within a common range gate is a collective Doppler velocity, v_d. The total line-of-sight (LOS) velocity of a scatterer can then be expressed as $v_i = v_d + v_{g_i}$. Assuming that the Doppler shift ω_{d_i} of the echo from a single scatterer is fully determined by the LOS velocity, this can be expressed as $\omega_{d_i} = 2kv_i$ where $k = 2\pi/\lambda$ and λ is the radar transmit wavelength. In this case, the frequency of the elementary field reflected by the ith scatterer is $\omega = \omega_0 + \omega_{d_i}$ where ω_0 is the radar transmission frequency. The phase of the returned signal depends both on time and range to the target as well as the velocity of the target and can be expressed as

$$\phi_i(t, r_i) = -2k((v_d + v_{g_i})t + r_{i0}) \tag{2.4}$$

where the factor of two represents the fact that the radar signal propagates from the radar

to the target and back.

As a result of (2.3) and (2.4), we can calculate the backscattered field at the radar location produced by a single scatterer at time t as

$$S_i(t) = |A_i(t)|e^{j\phi_i(t,r_i)} \tag{2.5}$$

where $|A_i(t)|$ is described by a combination of (2.2) and (2.3), and $\phi_i(t, r_i)$ is described by (2.4). Thus, assuming 2000 scatterers within a range gate, we can calculate the backscattered field from a single range gate r at the radar location at time t as

$$V_r(t) = \sum_{i=1}^{2000} S_i(t). \tag{2.6}$$

Note that S_i and V_r are complex.

2.4 Model Radar Operation

2.4.1 Setup

Once the model ionosphere has been created, it is sampled by the model radar. As described previously, SuperDARN radars employ a multipulse sequence, and therefore the simulator does as well. The pulse sequence is defined by the user and passed to the simulator. An example of a SuperDARN pulse sequence, *katscan*, is shown in Figure 2 of the companion

paper. In theory any sequence can be used; in the current implementation, three standard SuperDARN pulse sequences are automatically available, *normalscan*, *katscan*, and *tauscan*. The sampling is done by calculating the returns at discrete sample times using (2.6). This process begins at $t_0 \approx 1$ s, which allows for scatterer appearance and decay to reach a steady-state condition. Sampling of returns from a particular pulse begins at $t = t_0 + t_{pul} + t_{frang}$, where t is the time of the current sample, t_{pul} is the time of the pulse, and t_{frang} is the time it takes for the signal to travel to the location of the first range gate (distance to first range gate, in samples, is set by the user). Subsequent samples from this pulse are calculated by incrementing by a single range gate (equivalent to incrementing t by the sample separation, *smsep*) N_{rang} times. The user is responsible for passing an array, $qflg$ in Table 2.1, of size N_{rang} (number of range gates) to the simulator which contains flags to indicate which range gates contain backscatter. In reality, all of the simulated range gates contain scatterers, but only those with a $qflg$ of 1 will be sampled, rendering the scatterers in range gates with a $qflg$ of 0 invisible. The radar returns are sampled as voltages in the receiver. The radars operate with I (in-phase) and Q (quadrature) channels, meaning that the returns (as well as the voltage levels in (2.6)) consist of real and imaginary parts in quadrature.

2.4.2 Sampling

For each pulse, a single sample is collected from each range gate, resulting in a series of measurements $V_r(k)$ where the index r is associated with the rth range gate and the index k indicates a sample associated with the kth pulse. The data sampling is performed continuously at the rate determined by the spatial resolution (typically 45 km). Therefore, from the kth pulse, the received voltage due to backscattered signal from a range gate r is sampled

at a time of $r * smsep + t_{frang}$ after the pulse is emitted. In order to simplify sampling in the simulator, for a pulse sequence with N_{pul} pulses, N_{pul} separate voltage sequences of length N_{rang} are calculated, one for the returns from each pulse. The voltage sequences from different pulses are then superposed with the proper time offset in order to generate the final set of voltage samples, with only a single voltage for each sample time within the pulse sequence.

Note that with this manner of sampling, cross-range interference (CRI) is present in the radar samples. That is, if a pulse p_2 occurs before the last sample associated with a previous pulse p_1, there is an ambiguity about whether subsequent returns are from p_1 or p_2. In actual radar operation, this effect is dealt with by averaging the returns from a number of pulse sequences so that the incoherent contribution from interfering range gates decreases at a rate of $\propto 1/\sqrt{N_{avg}}$ where N_{avg} is the user-specified number of pulse sequences in the integration period. The user does however have the option to eliminate CRI from the simulated data, which is done by integrating range gates individually, which is equivalent to turning off the scatterers in all but one of the range gates.

2.4.3 ACF Calculation

The next step is to calculate ACFs for each range gate from the samples recorded for the pulse sequence. An ACF consists of a series of complex samples at discrete integer lag times, each with a real part Re and an imaginary part Im. The lag times are multiples of the smallest spacing between two consecutive pulses in the multipulse sequence, *mpinc*, which is an integer multiple of *smsep*. The lag times are due to all possible differences, $t_j - t_i$ where $i, j = 1, 2, ...N_{pul}$. The value of the ACF R from the pth pulse sequence at a particular integer lag l is calculated as

$$R_p(l) = V_p(t)V_p^*(t+\tau) \tag{2.7}$$

where the asterisk indicates a complex conjugate, $\tau = l * mpinc$, and l is the integer lag number of the ACF sample. The process of calculating voltage returns and ACFs is performed N_{avg} times. Once this process is complete, the ACFs from the individual pulse sequences are averaged (integrated) in order to produce a single ACF for each range gate. Specifically, the final ACF sample at lag l can be calculated as

$$R(l) = \sum_{p=1}^{N_{avg}} R_p(l)/N_{avg}. \tag{2.8}$$

2.5 Post-Processing

In order to make the simulated data more useable, some post-processing is performed.

2.5.1 Amplitude Normalization

Lag zero power, $P(0)$, is the power level of an ACF at lag zero. It is calculated according to

$$P(0) = \sqrt{Re\{R(0)\}^2 + Im\{R(0)\}^2}. \tag{2.9}$$

Because of the manner in which the simulator operates, the $P(0)$ of all of the range gates will fluctuate around some arbitrary value, which has no particular meaning. Therefore, all

of the ACFs are normalized to an average $P(0)$ of 1 (arbitrary units) to allow for scaling to a user-defined value (amp_0) and introduction of scaled noise into the signal. In order to do this, the average $P(0)$ of all of the range gates which contain backscatter, excluding any range gates which could contain CRI in lag zero, are calculated. The ACFs of all of the range gates which contain backscatter are then normalized by this value, resulting in all range gates containing scatter having an average $P(0)$ of 1. The ACFs can then be scaled in order to produce ACFs with average amplitudes of any value desired. Currently, the simulator also includes an option to force the signal to decay as a function of $1/r^2$, where r is range from the radar. The reason for this is that in real-life situations, signal amplitude decays with range, and $1/r^2$ is a plausible dependence. This is the only step in the simulation where real propagation conditions can be considered. This decay is implemented after normalization and scaling.

2.5.2 Introduction of Noise

The user of the simulator is able to set an option to model external noise by adding white noise ACFs to the simulated signal. If this option is set, then a second set of ACFs are calculated in the same fashion as before, where the scatterers have zero velocity, zero growth time, infinite lifetime, and a decorrelation time much less than *mpinc*. This causes the returned signal to correlate only with itself, resulting in ACFs of δ-correlated white noise. These ACFs are scaled by a value provided by the user to produce the desired SNR. The noise level is set relative to the magnitude of the signal ACFs. These noise ACFs are then added to the post-processed signal ACFs, which is the final product returned to the user. Note that the noise level is relative to the signal level at range gate 0, so if the user selects to have power decay with range, SNR will subsequently also decay with range.

Alternatively, the user can choose to have the raw voltage samples returned instead of the calculated ACFs. This mimics actual radar operation in that data can be stored as (i) averaged ACFs in RAWACF files or (ii) as voltages at the sampling times in IQDAT files, both of which are standard SuperDARN file formats. With option (ii), the averaged ACFs can be obtained in post-processing but there is a considerable storage requirement (one day of radar IQDAT data requires ≈1.5 GB of storage).

2.6 Results

The simulator has been designed to produce realistic data including statistical fluctuations. A real SuperDARN ACF from the Fort Hays East, Kansas radar recorded on 2 April 2012 at 05:30 UT using the *katscan* pulse sequence and $N_{avg} = 21$ is shown in Figure 2.1a. In this case, the sample separation is 300 μs, corresponding to a range separation of 45 km, and a basic lag time of 1500 μs The fitted parameters for this data are as follows: $t_d = 55$ ms, $v_{LOS} = 365$ m/s, and $SNR = 9$ dB. An example of an ACF that has been generated with the simulator is shown in Figure 2.1b. This ACF was generated with the *katscan* pulse sequence, $N_{avg} = 21$, $t_d = 50$ ms, $v_{LOS} = 350$ m/s, $R(0) = 10000$ and $SNR = 9$ dB. It is apparent from this figure that realistic statistical fluctuations are present in the simulated ACFs as the two ACFs display similar properties in terms of both phase progression and amplitude decay. Note that lags are missing in the ACF derived from the data (indicated by diamonds) owing to bad samples from pulse-overlap interference and CRI.

In order to test whether the statistical fluctuations present in simulated ACFs are at correct levels, ACF power and phase fluctuations were examined. A total of 1000 ACFs were simulated with $t_d = 5$ ms, $v_{LOS} = 350$ m/s, $N_{avg} = 50$. The effects of Gaussian velocity spread,

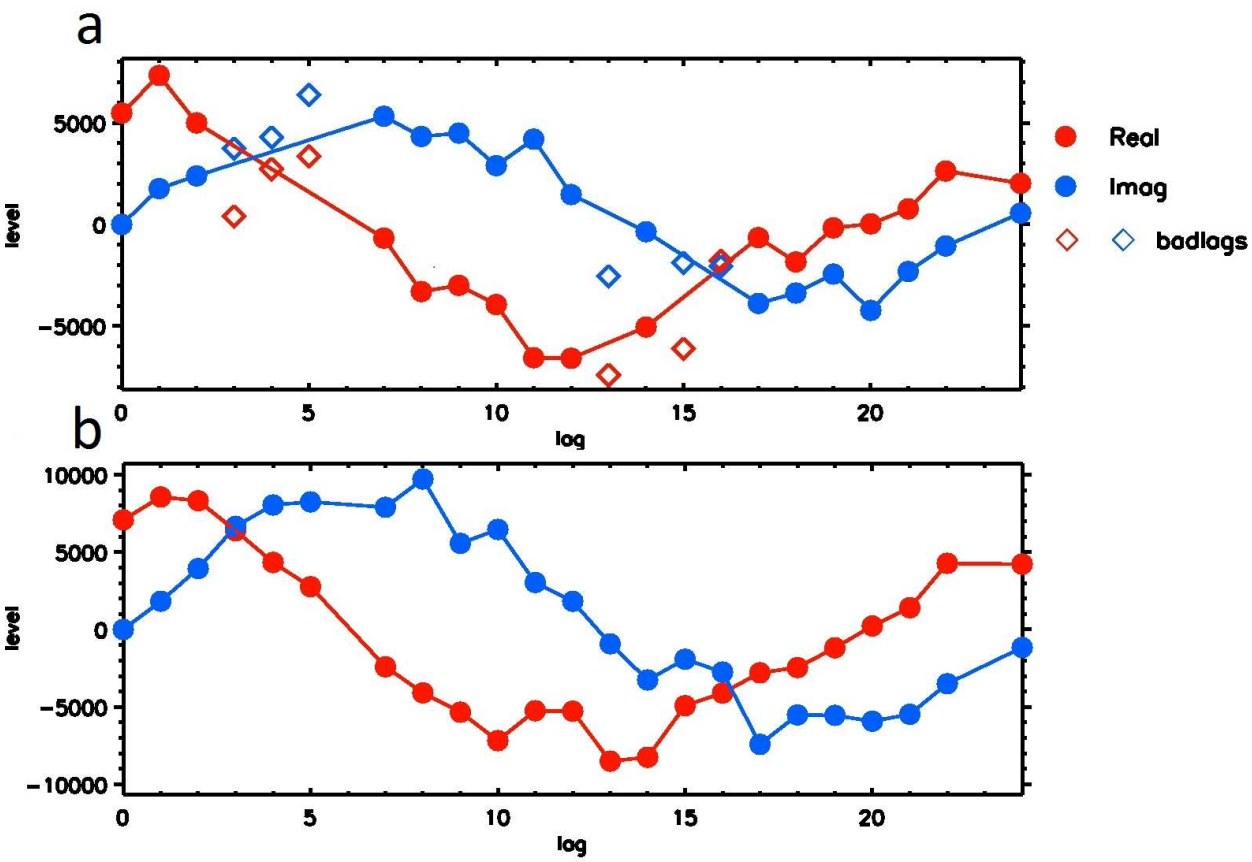

Figure 2.1: (a) A measured SuperDARN ACF from the Fort Hays East, Kansas radar recorded on 2 April 2012 at 05:30 UT using the *katscan* pulse sequence and $N_{avg} = 21$. The fitted parameters for this data are as follows: $t_d = 55$ ms, $v_{LOS} = 365$ m/s, and $SNR = 9$ dB. The x-axis represents lag time in increments of *mpinc*, and the y-axis represents ACF signal level. Note that lags which have been flagged as bad by the processing are plotted as open symbols. (b) An example of a simulated ACF. This ACF was generated with the *katscan* pulse sequence, $N_{avg} = 21$, $t_d = 50$ ms, $v_{LOS} = 350$ m/s, $R(0) = 10000$ and $SNR = 9$ dB. Note the similarity between the two panels.

scatterer disappearance, irregularity growth, CRI, and white noise were set to be negligible in this simulation. These parameters can be ignored because they do not affect the statistical fluctuation level. Figure 2.2 shows a histogram of ACF lag power which shows that the simulator accurately reproduces the statistical power fluctuations. The x-axis shows ACF lag time and the y-axis shows normalized ACF power, calculated using (2.9). The color coding indicates the number of simulated ACFs with lags in a power bin, and the diamonds rep-

resent the mean values. The solid curve represents the ideal ACF power curve, the vertical dash-dot line represents the decorrelation time t_d, and the horizontal dash-dot line represents the e-folding power. The fact that the diamonds follow the ideal curve very closely for $t < t_d$ indicates that the simulator is behaving as expected. The horizontal dashed line represents the statistical fluctuation level, $\sigma = P(0)/\sqrt{N_{avg}}$. This fluctuation level is the magnitude of the expected value of the fluctuation of the ACF power level [*Ponomarenko and Waters*, 2006]. Thus, as ACF power approaches zero in later lags, the expectation is that statistical fluctuations become the dominant source of power. The fact that the diamonds are very close to σ for the later lags indicates that statistical fluctuations are being reproduced properly.

Figure 2.3 shows a similar plot to Figure 2.2 for the phase variation. The data are taken from 1000 ACFs simulated with $N_{avg} = 50$, $t_d = 30$ ms, and $v_d = 350$ m/s. The color coding is for number of ACF lags in a particular lag-phase bin. The solid line shows an idealized lag phase progression for $v_{LOS} = 350$ m/s. It is evident that the simulated ACFs show a phase progression that is consistent with what one would expect for the simulated Doppler velocity. It is also apparent that as lag time increases, the variability in the phase also increases. This is expected, and occurs because ACF amplitude decays with time while the statistical fluctuation level remains constant, meaning that statistical fluctuations become more prominent in the ACF.

2.7 Conclusions

We have developed a robust, physically-based SuperDARN data simulator which is able to model radar returns from ionospheric irregularities. Statistical fluctuations are well-modeled by the simulator. This simulator can be used to generate realistic data for the purpose of

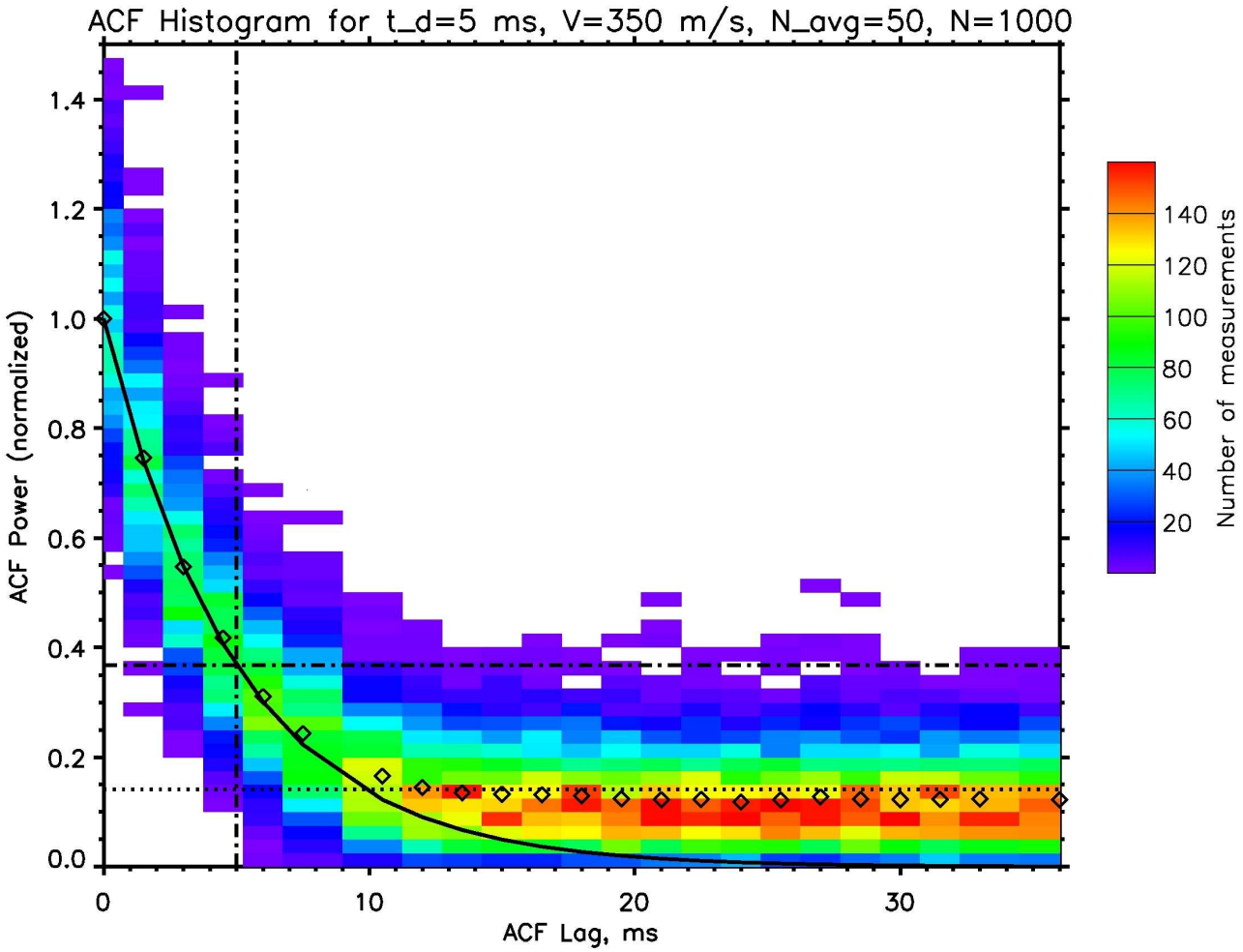

Figure 2.2: Histogram of ACF lag powers for 1000 simulated ACFs. The simulator was run with $N_{avg} = 50$, $t_d = 5$ ms (spectral width of ≈800 m/s), $v_d = 350$ m/s. An unphysical spectral width is used here in order to show the performance of the simulator when ACF power goes to the statistical fluctuation level. The color coding represents the number of ACFs with a lag power in a particular bin. The diamonds show the mean ACF lag powers at each individual lag. The solid curve represents an ideal power decay for an ACF with a decorrelation time of 5 ms. The vertical dash-dot line shows the decorrelation time of the simulated ACF, and the horizontal dash-dot line shows the e-folding power of an ideal ACF. The horizontal dashed line shows the statistical fluctuation level for an ACF with a lag zero power of unity and a N_{avg} of 50.

testing the processing of radar returns into higher-order products under controlled conditions. In the companion paper, the simulator is used to compare several methods of processing radar returns for Doppler velocity and spectral width. The simulator can be adapted to test

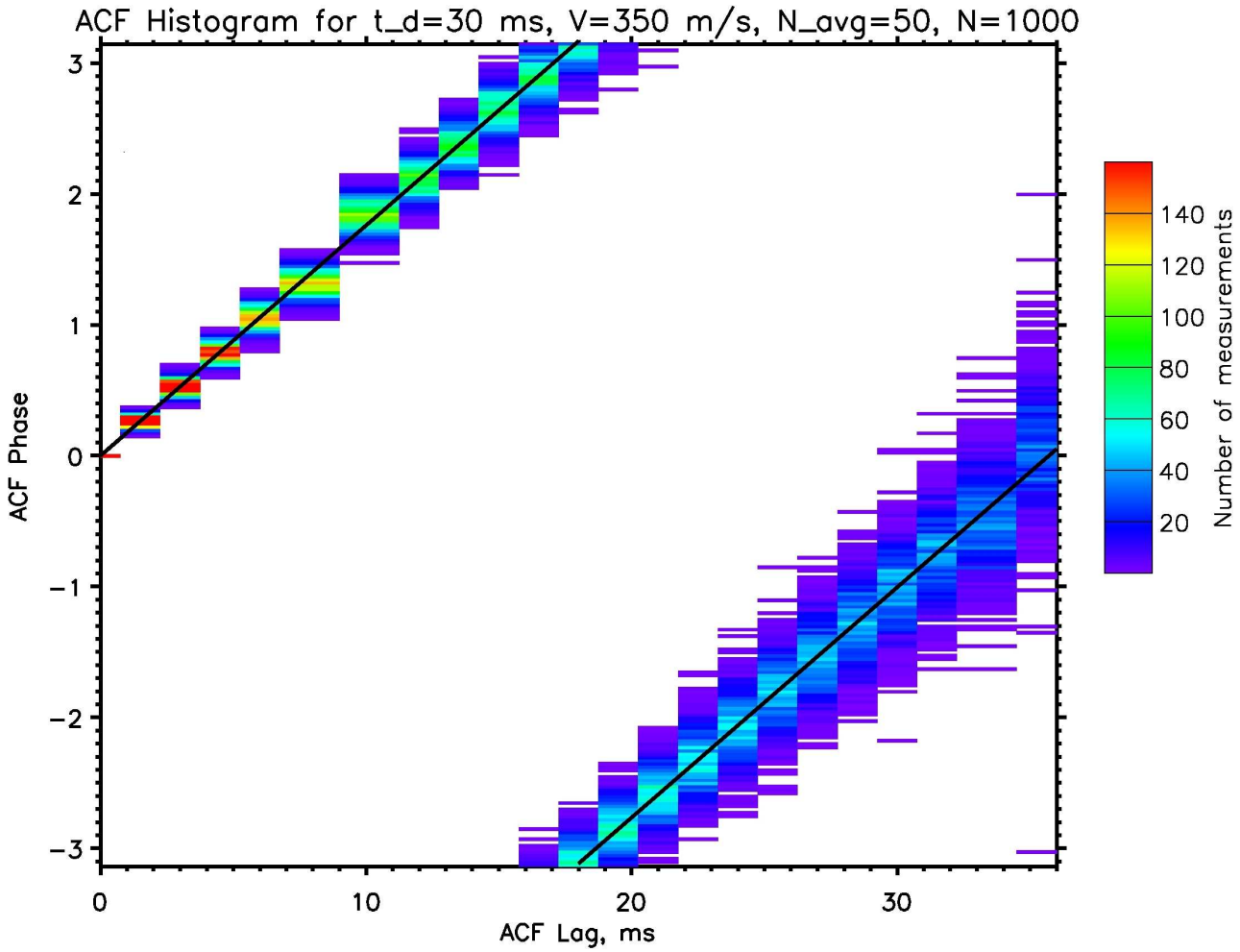

Figure 2.3: Histogram of ACF lag phases for 1000 simulated ACFs. The simulator was run with $N_{avg} = 50$, $t_d = .03$ s (spectral width of 132 m/s), $v_d = 350$ m/s. The color coding represents the number of ACFs with a lag phase in a particular bin. The solid line represents the ideal phase progression for a Doppler velocity of 350 m/s

processing algorithms for other types of pulsed ionospheric radars.

2.8 Acknowledgments

The authors thank the National Science Foundation for support under grants AGS-0849031 and AGS-0946900.

Chapter 3

A comparison of SuperDARN ACF fitting methods

A. J. Ribeiro,[1] J. M. Ruohoniemi,[1] P. V. Ponomarenko,[2] L. B. N. Clausen,[3] J. B. H. Baker,[1] R. A. Greenwald,[1] K. Oksavik[4,5] and S. de Larquier[1]

1: The Bradley Department of Electrical and Computer Engineering, Virginia Tech, Blacksburg, Virginia, USA.

2: Institute of Space and Atmospheric Studies, University of Saskatchewan, Saskatoon, Saskatchewan, Canada.

3: Institute for Geophysics and Extraterrestrial Physics, TU Braunschweig, Germany.

4: Department of Physics and Technology, University of Bergen, Norway.

5: Birkeland Centre for Space Science, Bergen, Norway.

Abstract

The Super Dual Auroral Radar Network (SuperDARN) is a worldwide chain of HF radars which monitor plasma dynamics in the ionosphere. Autocorrelation functions are routinely calculated from the radar returns and applied to estimate Doppler velocity, spectral width, and backscatter power. This fitting has traditionally been performed by a routine called FITACF. This routine initiates a fitting by selecting a subset of valid phase measurements and then empirically adjusting for 2π phase ambiguities. The slope of the phase variation with lag time then provides Doppler velocity. Doppler spectral width is found by an independent fitting of the decay of power to an assumed exponential or Gaussian function. In this paper, we use simulated data to assess the performance of FITACF, as well as two other newer fitting techniques, named FITEX2 and LMFIT. The key new feature of FITEX2 is that phase models are compared in a least-squares fitting sense with the actual data phases to determine the best fit, eliminating some ambiguities which are present in FITACF. The key new feature of LMFIT is that the complex ACF itself is fit, and Doppler velocity, spectral width, and backscatter power are solved simultaneously. We discuss some of the issues that negatively impact FITACF, and find that of the algorithms tested, LMFIT provides the best overall performance in fitting the SuperDARN ACFs. The techniques and the data simulator are applicable to other radar systems that utilize multipulse sequences to make simultaneous range and velocity determinations under aliasing conditions.

3.1 Introduction

The Super Dual Auroral Radar Network (SuperDARN) is a chain of HF radars which monitor ionospheric plasma convection in the northern and southern hemispheres by detecting backscatter from ionospheric plasma irregularities [*Greenwald et al.*, 1985; *Chisham et al.*, 2007]. A typical SuperDARN radar has 16 look directions ("beams") separated by 3.24° in azimuth, with 75-100 range gates along each beam separated by 45 km. The dwell time on any particular beam is typically 3-7 seconds (integration period) which results in a 1-2 minute azimuthal scan. Examples of field of view plots of a single scan are shown in Figure 3.1. Panel (a) shows SNR ("backscattered power"), panel (b) shows Doppler velocity, and panel (c) shows Doppler spectral width. These data are fairly representative in displaying a range of echo types including (i) an extended region of low velocity ground scatter at greater ranges on the more westward beams, (ii) meteor wind scatter at the very near ranges, (iii) a high-velocity ionospheric scatter feature on the middle beams, and (iv) spotty noise/interference elsewhere but especially on the more northward beams.

The nature of the primary targets detected by SuperDARN radars introduces certain complications. The principal dilemma arises because the radar was designed to detect targets with Doppler velocities of up to 2 km/s out to a range of 4500 km. These conditions impose mutually exclusive requirements on the nominal pulse repetition frequency (PRF). To avoid ambiguities in range we require a long inter-pulse period (PRF $\leq$ 33.3 Hz) while to avoid ambiguities in Doppler velocity we must have a shirt inter-pulse period (PRF $\geq$ 320 Hz). Some techniques which have been used to solve this problem are complementary codes, alternating codes [*Lehtinen*, 1986], and aperiodic sequences [*Uppala and Sahr*, 1994]. In order to resolve this dilemma, the radars employ multipulse sequences to simultaneously determine

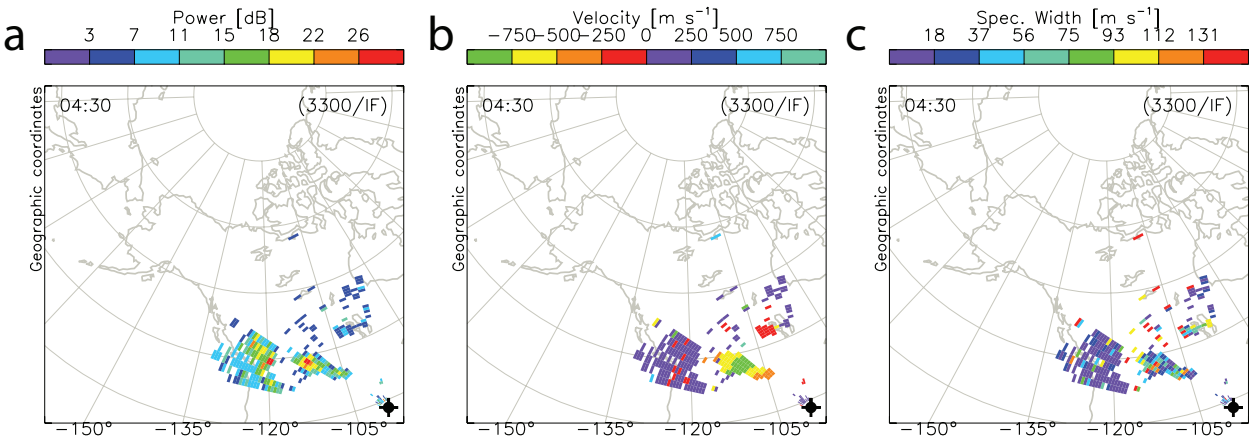

Figure 3.1: Examples of SuperDARN radar field of view plots. The data were collected with the Fort Hays West radar on 10 September 2011 over the interval 04:30-04:31 UT. The radar, located at 38.86° north, -99.39° west, was scanning across 22 beam directions, with range gates beginning at 180 km. The data were solved using FITEX2 as described in the text. The panels show (a) backscatter power, (b) Doppler velocity, (c) Doppler spectral width.

the range and Doppler velocity of targets [*Farley*, 1972; *Greenwald et al.*, 1985; *Hanuise et al.*, 1993; *Baker et al.*, 1995; *Barthes et al.*, 1998; *Ponomarenko and Waters*, 2006]. This means that instead of transmitting solitary pulses that are separated by a fixed time determined by the PRF, the radars periodically emit sequences of pulses that are separated unevenly in time by integer multipliers of an "elementary lag time" $\tau_0 = 1.5 - 2.4$ ms. By sampling the returns from a fixed range for each pulse of the sequence using a coherent receiver, all products of the complex autocorrelation function (ACF), $R_k = V(t)V^*(t+k\tau_0)$, where V is the receiver voltage sample and k is the lag number, can be calculated from 0 to $n\tau_0$, where n is the number of lags, with occasional misses at certain lags. An ACF is calculated for each range gate from the returns from each multipulse sequence. Averaging the returns over multiple sequence transmissions partially suppresses the contributions from pulses that encounter other scattering regions at the same sampling times (cross-range interference, CRI, a type of clutter) [*Baker et al.*, 1995]. This averaging occurs within what is called an integration period. An example of a standard SuperDARN multipulse sequence

is shown in Figure 3.2. One observes that with this eight pulse sequence, all but two of the lags can be computed up to a lag of 24.

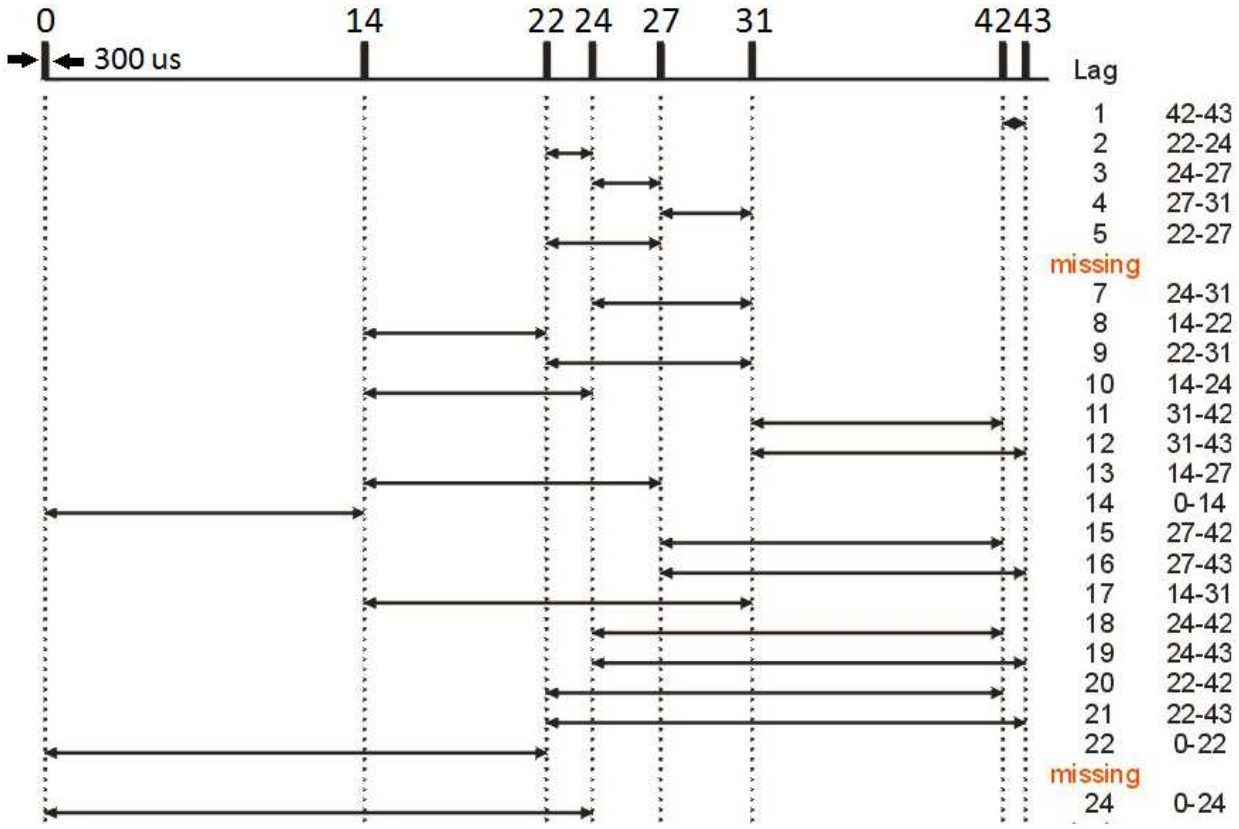

Figure 3.2: An illustration of a standard SuperDARN pulse sequence, called *katscan*. The raised bars represent transmit pulses, and the numbers represent lag time from the first pulse until transmission. The pulse duration is 300 μs, and the basic lag time is typically either 1500 or 2400 μs. Samples are recorded in between transmit pulses and after the last pulse. (Figure courtesy of K. A. McWilliams)

An integration period is typically 3-7 seconds in length. The total number of multipulse sequences transmitted during an integration varies between about 15 and 60. The ACFs calculated from all the sequences are then integrated in order to minimize interference and increase gain. The integrated ACFs are fit to model functions in order to resolve Doppler velocity (v), spectral width (w), and backscatter power (signal-to-noise ratio, SNR) as functions of range. Figure 3.3a shows an ACF from the Fort Hays West radar taken from the period of

Figure 3.1. The ACF consists of a real part (red curve), $Re\{R\}$, and an imaginary part (blue curve), $Im\{R\}$, in quadrature. Note that the real part has a maximum at lag zero, and the imaginary part has a value of zero at lag zero. The Doppler shift imposed on the frequency of the returned signal is manifested as a systematic variation of phase with lag. The phase ϕ at lag τ is calculated as $\phi(\tau) = \arctan(Im\{R(\tau)\}/Re\{R(\tau)\})$. Figure 3.3b illustrates the variation of phase with lag for the ACF of Figure 3.3a. The maximum Doppler frequency shift, f_{dmax}, that can be resolved is related to the basic lag time, τ_0, by $f_{dmax} = 1/(2\tau_0)$. Typically, this value is $\approx$ 300 Hz, corresponding to a maximum Doppler velocity of $\approx$ 4000 m/s. The lag power P at lag τ is calculated as $P(\tau) = |R(\tau)|$. The SNR is found using the fitted signal level at lag zero, R_0, of the ACF. The spectral width is obtained as a decay of the amplitude of the ACF with lag, i.e., a decrease in $P(\tau)$ with τ. Figure 3.3c shows the lag powers for the ACF of Figure 3.3a. A detailed discussion of the physical significance of spectral width in terms of signal composition is given by *Ponomarenko and Waters* [2006]. In order to actually calculate v, w, and SNR from the radar data, fits must be performed to the lag phases and powers of the ACFs.

FITACF is the name of the traditional routine used to process SuperDARN ACFs. While it has performed reasonably well since the inception of SuperDARN, its performance has rarely been tested, mainly because of the absence of a realistic data simulator accounting for both regular and random components of the backscatter echoes. Some other algorithms have been developed over the last few years that attempt to improve data quality, but to compare their performance to that of FITACF objectively, again one needs to have a controlled set of inputs such as can be provided by a comprehensive data simulator. An appropriate simulator has recently been developed by *Ribeiro et al.* [2013b] based on the collective scatter model initially conceived by *Ponomarenko et al.* [2008].

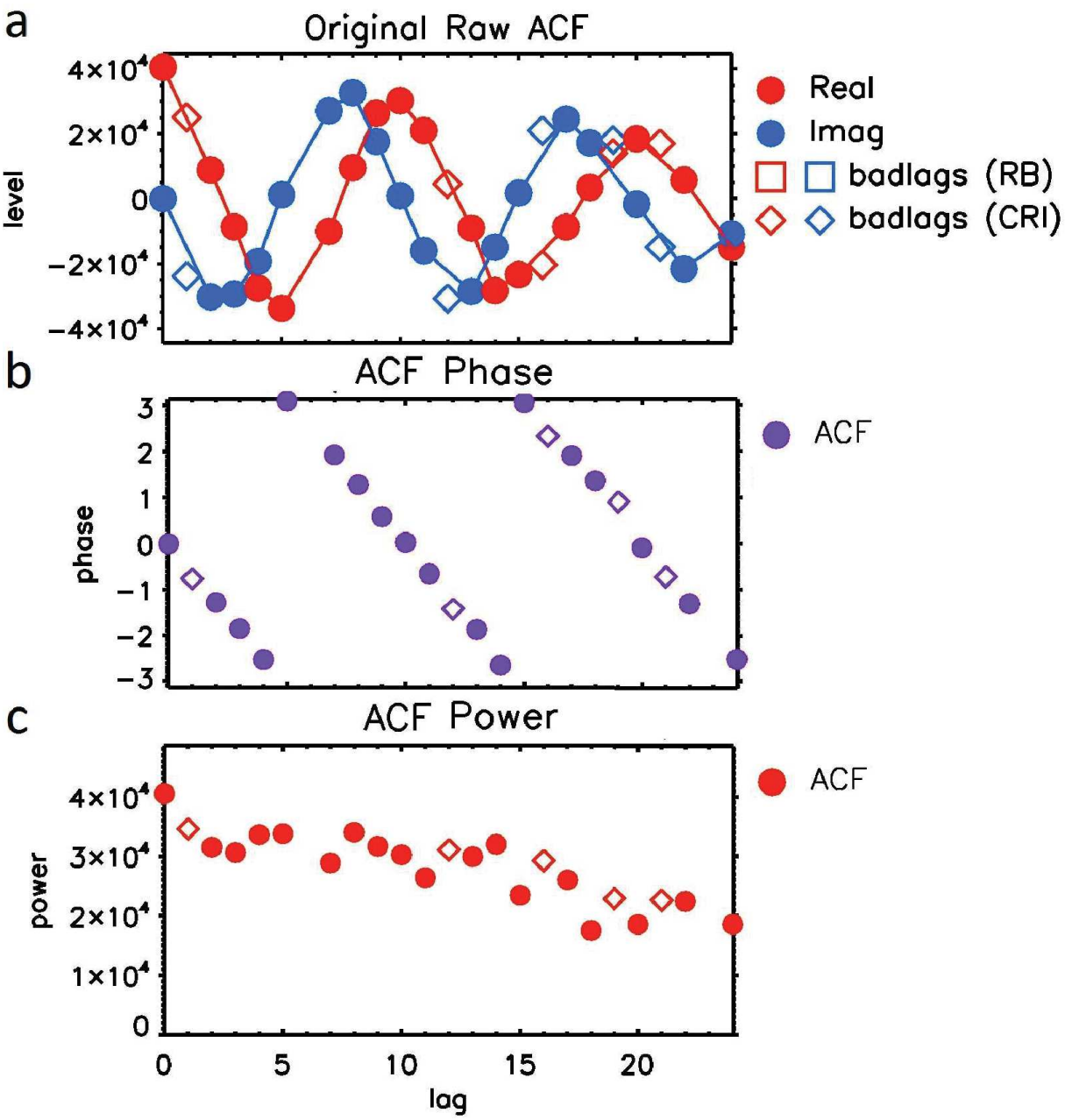

Figure 3.3: (a) A SuperDARN ACF from the Fort Hays West radar in Kansas. The data were collected on 10 September 2011 at 04:30 UT from beam 7 and range gate 27. The real part of the ACF is plotted in red and the imaginary part is plotted in blue. The ACF values at individual lags are plotted as discrete points. Any lags that have been identified as bad are plotted as open shapes. (b) The lag phases in radians for the ACF in (a). (c) The lag powers for the ACF in (a).

In this paper, we examine three different ways of extracting Doppler velocity, spectral width, and SNR from SuperDARN ACFs. We first analyze the conventional FITACF package, in use for almost thirty years. The second method is FITEX2, which is an iteration on a routine called FITEX, which was developed in order to fit a specific multipulse sequence. Finally, we test so-called LMFIT, which uses the Levenberg-Marquardt algorithm [*Levenberg*, 1944; *Marquardt*, 1963] to fit the complex ACF in a single procedure. The aim of this analysis is to compare the performances of the three routines and determine which is the most reliable at extracting Doppler velocity and spectral width from SuperDARN ACFs.

3.2 Description of Fitting Methods

3.2.1 Common Routines

Some procedures are common to all three ACF fitting routines. This includes subroutines which determine so-called "bad" lags, which are not suitable for use in the fitting process. A lag is flagged as bad in initial processing if it is (i) contaminated by CRI, or, (ii) affected by transmitter pulse overlap (a pulse was being transmitted when a sample should have been recorded). All three fitting methods use the same such subroutines in initial processing and therefore have the same lags flagged as bad. A "good" lag is one which is not bad, and a minimum of four good lags must be present for fitting to occur. In Figure 3.3a, lags that have been identified as bad in initial processing are plotted as open circles and diamonds. Additionally, all three routines use the same algorithms to find a noise power level, N, for each integration period, which is done by calculating the average $P(0)$ of the 10 lowest power ACFs on a given beam sounding. The three routines will not have the same

exact noise figure, however, because FITACF does some calculations with integers, whereas FITEX2 and LMFIT use double precision numbers for all calculations.

3.2.2 FITACF

FITACF is the traditional method used for fitting SuperDARN ACFs. The version used in this paper is distributed with the SuperDARN Radar Software Toolkit 3 [1] (RST3). In addition to the three common routines discussed previously, another bad lag routine is also invoked by FITACF at the stage of fitting the ACF. This routine identifies additional lags as bad depending on some empirical criteria for a single Doppler component (e.g. monotonous power decay with increasing lags) [*Ponomarenko and Waters*, 2006]. This routine is not used in the other two fitting routines because of recommendations made by P. Ponomarenko and C. Waters at the 2006 SuperDARN meeting held at Chincoteague, Virginia. However, in FITEX2 and LMFIT, any lags with power values less than the statistical fluctuation level ($\sigma_P = P(0)/\sqrt{N_{avg}}$, where N_{avg} is the number of integrated pulse sequences) are assigned a very low weight, so as to be effectively excluded from the fitting, in accordance with the same recommendations. Lags flagged as bad by this checking are indicated by open triangles in plots of the type shown in Figure 3.3.

To resolve all three major information parameters, v, w, and SNR, FITACF applies two separate fitting procedures. The Doppler velocity is determined from the variation of phase with lag, i.e.,

$$v = \frac{\lambda}{4\pi}\frac{\partial\phi}{\partial\tau}, \tag{3.1}$$

[1] http://superdarn.jhuapl.edu/software/index.html

where λ is the radar wavelength. A linear least-squares fit is performed to determine $\delta\phi/\delta\tau$. In determining the phase slope it is important to account for the 2π uncertainty in the phase shift variation with τ. With FITACF, an initial estimate of the number of 2π phase cycles across the full extent of lag time is made using the phases of the first four lags. Subsequent lags are fit by advancing one lag at a time and considering whether to unfold a 2π phase variation and then fitting the phase slope over the augmented set of lags. The fact that FITACF must make an initial guess will be an important issue later in this discussion.

A completed FITACF phase-fit for the data shown in Figure 3.3 is shown in Figure 3.4a. The phases corresponding to the data are plotted in purple, while the fitted solution is plotted as a green dash-dot line. The solid circles and open diamonds represent the "good" and "bad" lags, respectively. The Doppler velocity is calculated from the slope of the best-fit line. Note that even though the data and fit are shown as a sawtooth pattern, the fitting is actually performed as a straight line that extends over multiple 2π ranges. In this case, the line-of-sight Doppler velocity calculated from the slope of the best-fit line is v = -916 m/s, where the minus signifies motion away from the radar.

In order to resolve Doppler spectral width and power, a model is fitted to $|R(\tau)|$. For the entirety of this paper, we will assume that the ACF amplitude decays exponentially, i.e., $|R(\tau)| = R_0 e^{-\tau/t_d}$ where t_d is a decay time constant [*Ponomarenko et al.*, 2007]. For the actual calculation of parameters, a second linear least-squares fit is performed to the natural logarithm of the $|R(\tau)|$ of the ACF.

The resulting y-intercept of the fitted model represents the fitted lag zero power, R_0, which is then used to calculate SNR in dB,

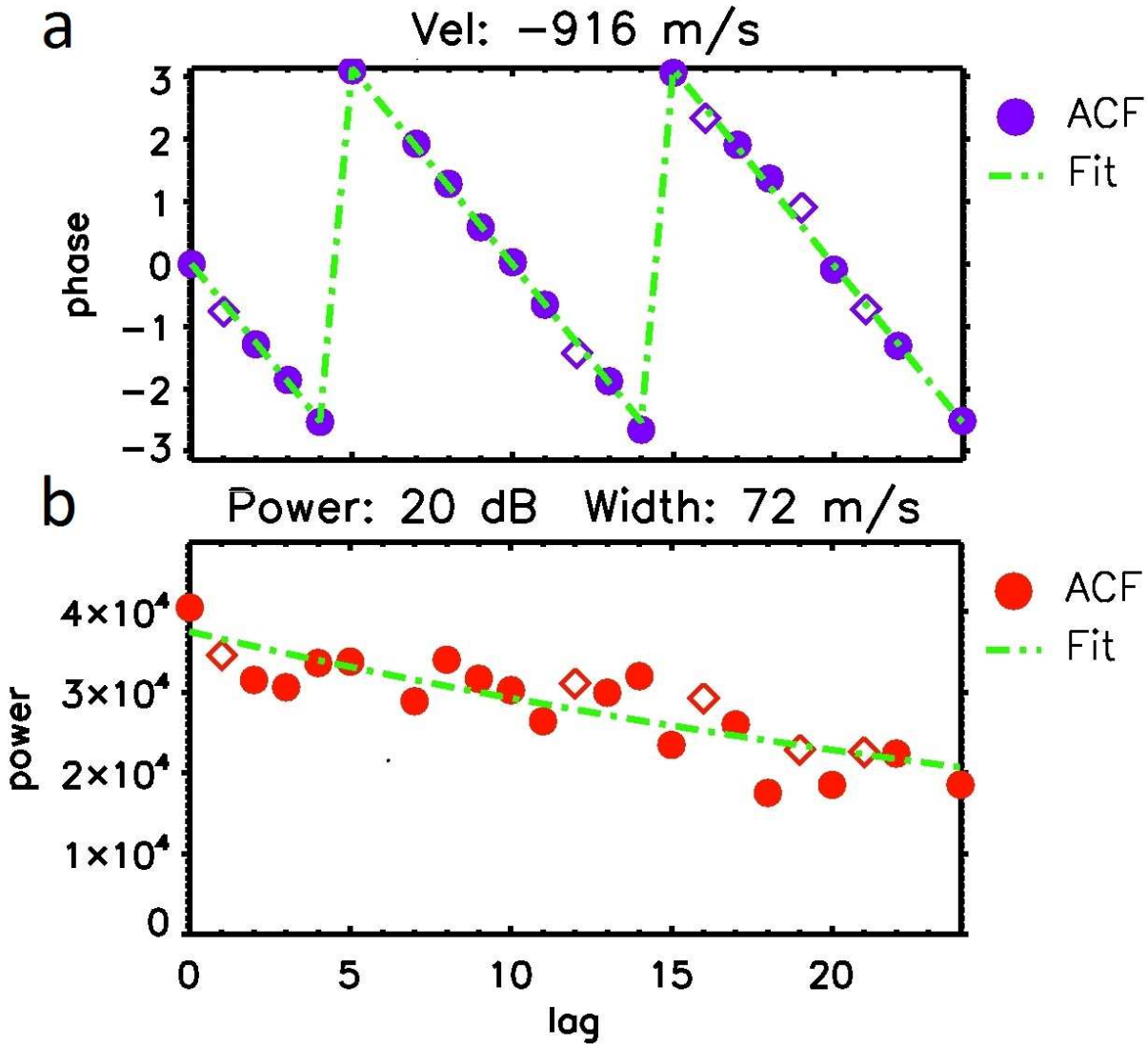

Figure 3.4: FITACF results for the data in Figure 3.3. (a) The phase fit used to resolve Doppler velocity. The actual lag phases are plotted in purple and the fit is plotted in green. (b) Log power fit used to resolve power (SNR) and spectral width. The actual lag powers are plotted in red, and the fit is plotted in green.

$$SNR = 10 \log_{10}(R_0/N). \tag{3.2}$$

The slope of the linear log-power fit is used to calculate the exponential decay time of the signal, which in turn is used to find the spectral width of the ACF, which is determined as

the width of a model spectrum at a half-power level and for the exponential model can be expressed as

$$w = \frac{\lambda}{2\pi t_d}. \tag{3.3}$$

A completed log-power fit is shown in Figure 3.4b. The lag powers are presented as red symbols, while the best fit line is plotted in green. For this particular ACF, the FITACF analysis gives $w = 72$ m/s and an SNR = 20 dB.

3.2.3 FITEX2

FITEX2 represents an iteration on an earlier routine called FITEX. FITEX was originally developed as a new method to fit velocity data from a particular pulse sequence, known as *tauscan*, which is described in *Greenwald et al.* [2008]. Similar to FITACF, a weighted linear least-squares fit to the log of the ACF lag powers is used to resolve SNR and spectral width. However, the phase fitting differs significantly. Instead of the linear phase fit, 120 phase variation models spanning the 180° range at 1.5° intervals are calculated and compared to the phases of the actual data. The number of models used is a trade-off between the computational burden of doing the comparison, which increases with the number of models, and the resolution of the velocity determination. These pre-determined models are then fitted to the actual sawtooth pattern (e.g. Figure 3.3a) without the need for an initial guess on the number of 2π cycles across the ACF lag range. Once this comparison is complete, the model that produces the lowest root-mean-squared (RMS) error is chosen to be the best fit. If this best fit produces an RMS error more than three standard deviations below the mean error across all models, it is determined that the fit is valid ("good"), and v is calculated

from the model. The major disadvantage of FITEX is that it only provides ≈ 25 m/s velocity resolution because of the discrete steps in the phase slopes of the 120 models. The result of the model comparison with the data in Figure 3.3 is shown in Figure 3.5.

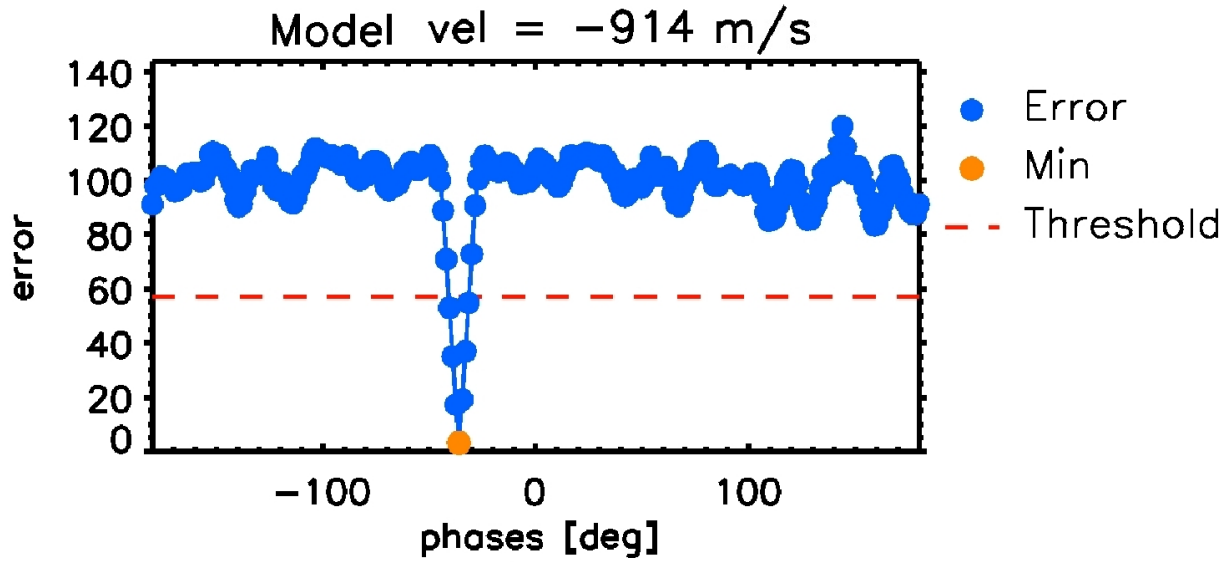

Figure 3.5: FITEX2 model comparison results for the ACF in Figure 3.3. The orange circle represents the lowest error model. The horizontal dashed line represents the error threshold for a good model fit (3 standard deviations below the mean model error). The model velocity which produces the lowest error is -914 m/s.

The subsequent version, FITEX2 was developed to solve Doppler velocity to arbitrary resolution. For improvement of Doppler velocity resolution, the best model phase fit from FITEX is used as an initial guess for the bisection method algorithm described in *Press et al.* [1992]. This provides arbitrary velocity resolution, while only increasing processing time by the equivalent of 5-10 model comparisons. For the data in Figure 3.3, FITEX2 returns v = -916 m/s, W = 73 m/s, and SNR = 20 dB, which are essentially the same as determined by FITACF. The FITEX criteria for a good fit are also used in FITEX2.

3.2.4 LMFIT

In contrast to FITACF and FITEX2, which apply two separate fitting procedures for the ACF phase and power, this routine performs a single model fit to a complex ACF consisting of real and imaginary parts, so that v, w and SNR are resolved simultaneously. Specifically, R_0, Doppler frequency, and decay time constant are adjusted to fit a model to the empirical data. Previously, *Ponomarenko et al.* [2008] used this method to fit ACFs in the special case of "mixed scatter," which occurs when a single range gate contains backscatter from two distinct targets, which are usually ionospheric plasma irregularities and the terrestrial surface (ground scatter). It should be noted that in this paper we are only testing the ability of LMFIT to fit single-component scatter. The name LMFIT is given to this approach because it utilizes the Levenberg-Marquardt non-linear fitting method [*Levenberg*, 1944; *Marquardt*, 1963; *Press et al.*, 1992]

In order to apply LMFIT, the ACF must be expressed as a single function. We choose to use a modified version of an exponentially decaying harmonic function described by *Ponomarenko et al.* [2008], i.e.,

$$R(\tau) = R_0 e^{-\tau/t_d} e^{j2\pi\tau f_d} \tag{3.4}$$

where $j = \sqrt{-1}$, and $f_d = \frac{1}{2\pi}\frac{\partial\phi}{\partial\tau}$ is Doppler frequency. In this equation, the first exponential describes the decay of the signal amplitude, while the second (complex) exponential describes the phase variation of the signal. Doppler velocity, spectral width, and SNR (in dB) can then be calculated using Equations (3.5), (3.3), and (3.2), respectively.

$$v_d = \lambda f_d / 2 \tag{3.5}$$

For implementation of the Levenberg-Marquardt algorithm, the free C library MPFIT is used [*Markwardt*, 2009]. This requires that initial guesses be provided on the three parameters before the fitting starts. For this purpose, we used the Doppler velocity and spectral width results from FITEX in order to provide initial guesses of f_d and t_d. The decay time parameter is limited to between .001 and 1000 s, which correspond to spectral widths of about 4000 and .004 m/s, respectively. Values measured by SuperDARN radars typically range from zero to hundreds of meters per second. The initial guess for R_0 is set to the value of the real part of the ACF at lag zero. A good fit status is returned from LMFIT if (i) the model comparison yields a result with an error that is three standard deviations below the mean model error (as in FITEX2); (ii) MPFIT returns a non-error status; and, (iii) R_0 is greater than 150% of the ACF error on the fit. ACF error is a measure of how far an ideal ACF generated from the fitted parameters deviates from the ACF being fitted. The result of using LMFIT on the ACF from Figure 3.3 is shown in Figure 3.6. LMFIT returns a Doppler velocity of -917 m/s, a spectral width of 77 m/s, and an SNR of 20 dB.

3.3 Test Data

For thorough testing of all three fitting routines, we used artificial ACFs generated by a simulator described in detail by *Ribeiro et al.* [2013b]. The simulator allows us to set desired values for v, t_d (w) and SNR. Importantly, the simulator utilizes the collective scatter approach allowing for realistic simulation of the statistical variability of the backscatter echoes by setting the appropriate number of averaged pulse sequences.

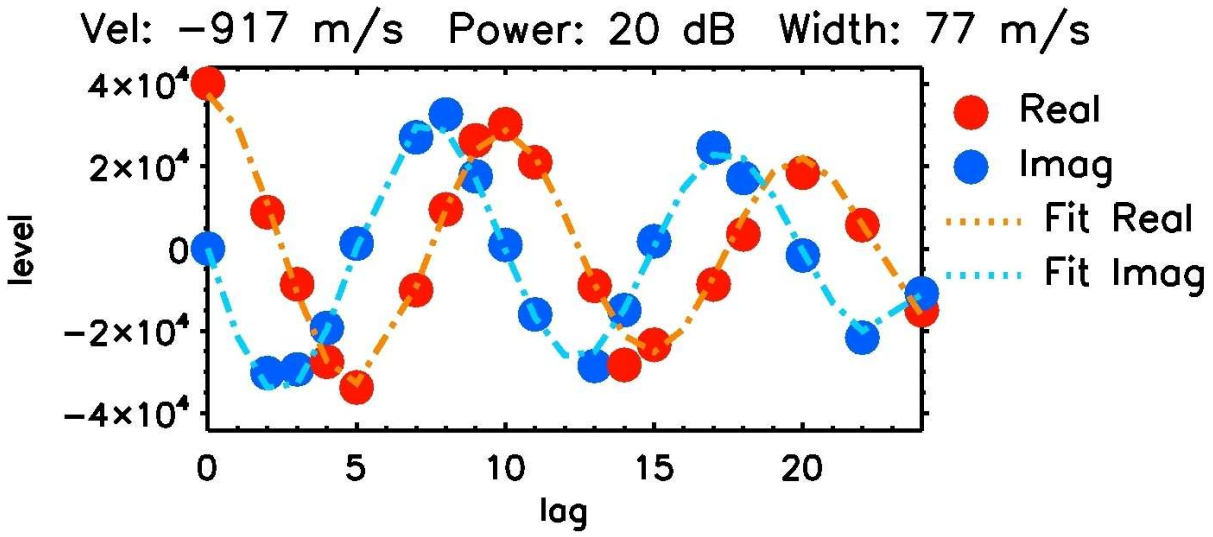

Figure 3.6: LMFIT results for the ACF in Figure 3.3. The red and blue circles represent the actual ACF, whereas the orange and blue lines represent the fitted ACF calculated from the outputs of the LMFIT algorithm.

In order to cover a range of v and w, we simulate data over a two-dimensional grid of values with fixed decay time and Doppler velocity at the nodes. We used the 8-pulse sequence *katscan* (Figure 3.2) with basic lag of $\tau_0 = 1.5$ ms, radar frequency $f_0 = 12$ MHz and $N_{avg} = 35$. The simulated data contains Doppler velocity values from 50 to 1950 m/s in 100 m/s steps, and decay time values from .01 to .1 s in .01 s steps. SNR is fixed at a maximum of 25 dB. The effects of irregularity growth, particle precipitation, and velocity spread are set to be negligible in the simulation parameters. There are 500 samples for each combination of decay time and Doppler velocity, resulting in a total of 100000 ACFs. Note that decay time is referred to here instead of spectral width because it is the more fundamental value and does not have a linear relation with spectral width. Conversely, Doppler velocity is used even though Doppler frequency is the more fundamental value, because it does have a linear relationship with frequency. In the remainder of this paper, decay time and Doppler velocity will be the values used to address error. Lag zero power error will not be examined because although much information is potentially available from the

backscattered power measurement, these data are little used and we simplify our presentation here by not examining the error on the lag zero power estimate.

In order to simulate a realistic range profile of the backscatter echoes, each integration period contains a band of 10 range gates containing scatter separated by 45 km. The SNR decreases with range R as $1/R^2$ to account plausibly for the geometrical decay of the radar transmission. This coefficient of $1/R^2$ is appropriate for ionospheric beam filling, as opposed to hard target backscatter which would decay as $1/R^4$. Here $R = (n+1) \times 45$ km, where $n = 0-9$ is the range gate number.

3.4 Results

For the comparison, all 100000 simulated ACFs are fed into the three fitting routines, and the results are stored. Three specific types of error are examined specifically for this exercise, and these will be explained later on in the paper. For all three types, error will be calculated in terms of the deviations from the inputs to the simulator. Regardless of type, error values are only retained for the specific routines which return a good fit.

First, Doppler velocity estimate error is analyzed in a root-mean-squared (RMS) error fashion to review the typical error magnitude, i.e.

$$\sigma_v = \sqrt{\langle (v - v_0)^2 \rangle} \tag{3.6}$$

where v is the fitted velocity, v_0 is the velocity input to the simulator, and the brackets indicate averaging over all of the valid fitted values. Second, presence of a regular bias/offset

is analyzed in terms of mean (signed) deviation,

$$\Delta_v = \langle v - v_0 \rangle \tag{3.7}$$

Finally, normalized RMS errors are examined for fitted decay times. The errors are calculated in a similar fashion to the velocity errors, except that they are normalized by the original input (to the simulator) decay time quantity, i.e.

$$\sigma_t = \sqrt{\langle [(t_d - t_{d0})]^2 \rangle} / t_{d0} \tag{3.8}$$

where σ_t is the error on the decay time estimate, t_d is the fitted decay time and t_{d0} is the decay time input to the simulator. True decay time errors are not discussed in this paper because none of the fitting routines exhibit a bias in the calculation of decay time.

3.4.1 Velocity Errors

The velocity errors are most important because they a have direct influence on the main SuperDARN product, high-latitude plasma circulation and electric field maps which are based on the Doppler velocity estimates [*Ruohoniemi and Baker*, 1998]. Because of this, velocity error should be the primary consideration in determining which fitting method provides the best performance.

RMS

Figure 3.7 presents σ_v (Equation (3.6)) for three values of input $t_{d0} = 0.01$, 0.03, and 0.10 s which correspond to $W \approx 398$, 133, and 39 m/s, respectively. The first feature that stands out is that FITACF performs extremely poorly for higher (> 1 km/s) Doppler velocities. Another feature that is apparent is that FITEX2 and LMFIT have some pronounced errors with bad fits at $t_{d0} = .01$ s, i.e., for very wide spectra. These bad fits occur in the same velocity bins because FITEX processing is used to obtain an initial velocity for LMFIT. In general, LMFIT outperforms the other methods for $t_{d0} < .03$ ($W > 133$ m/s) and all three fitting routines stabilize above this level. Figure 3.7 also illustrates that with longer decay time (decreasing spectral width), the error in velocity estimates generally decreases for all three methods.

Bias

Another aspect of the velocity estimation that must be examined is whether any of the three fitting routines have a statistical high or low bias, i.e., a chronic under- or over-estimation of velocity. To illustrate this, in Figure 3.8 we show mean velocity deviation, Δ_v (Equation (3.7)). Again, three different simulated decay times are pictured, 0.01, 0.03, and 0.1 s. It is immediately apparent that FITEX2 and LMFIT have no apparent bias, while FITACF consistently produces velocities with the wrong sign for $|v| \geq 1000$ m/s. This bias begins when the simulated velocity is high enough to cause problems with the initial guess of the number of 2π phase cycles. This effect will be discussed later in this paper.

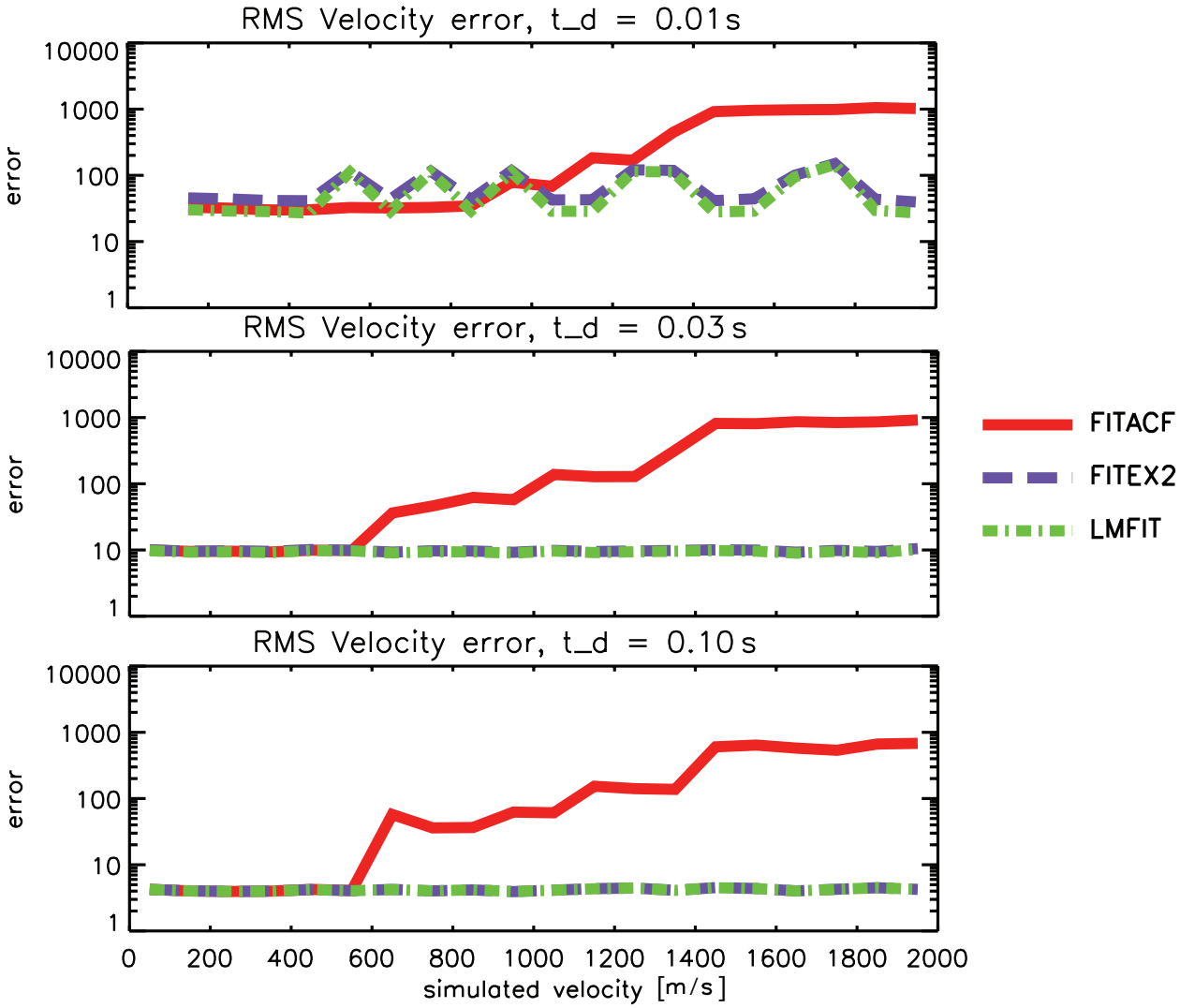

Figure 3.7: RMS velocity estimate errors for the three fitting routines for three different decay times, .01, .03, and .10 s, which correspond to spectral widths of 398, 133, and 39 m/s, respectively. The x-axis shows simulated velocity. The y-axis represents RMS errors. The red, purple, and green lines represent FITACF, FITEX2, and LMFIT, respectively.

3.4.2 Decay Time (Spectral Width) Errors

Spectral width is the second most scientifically important parameter that is returned from these fitting routines, as it is typically used in conjunction with Doppler velocity to classify backscatter as ionospheric or ground [*Blanchard et al.*, 2009]. It has also been used as a

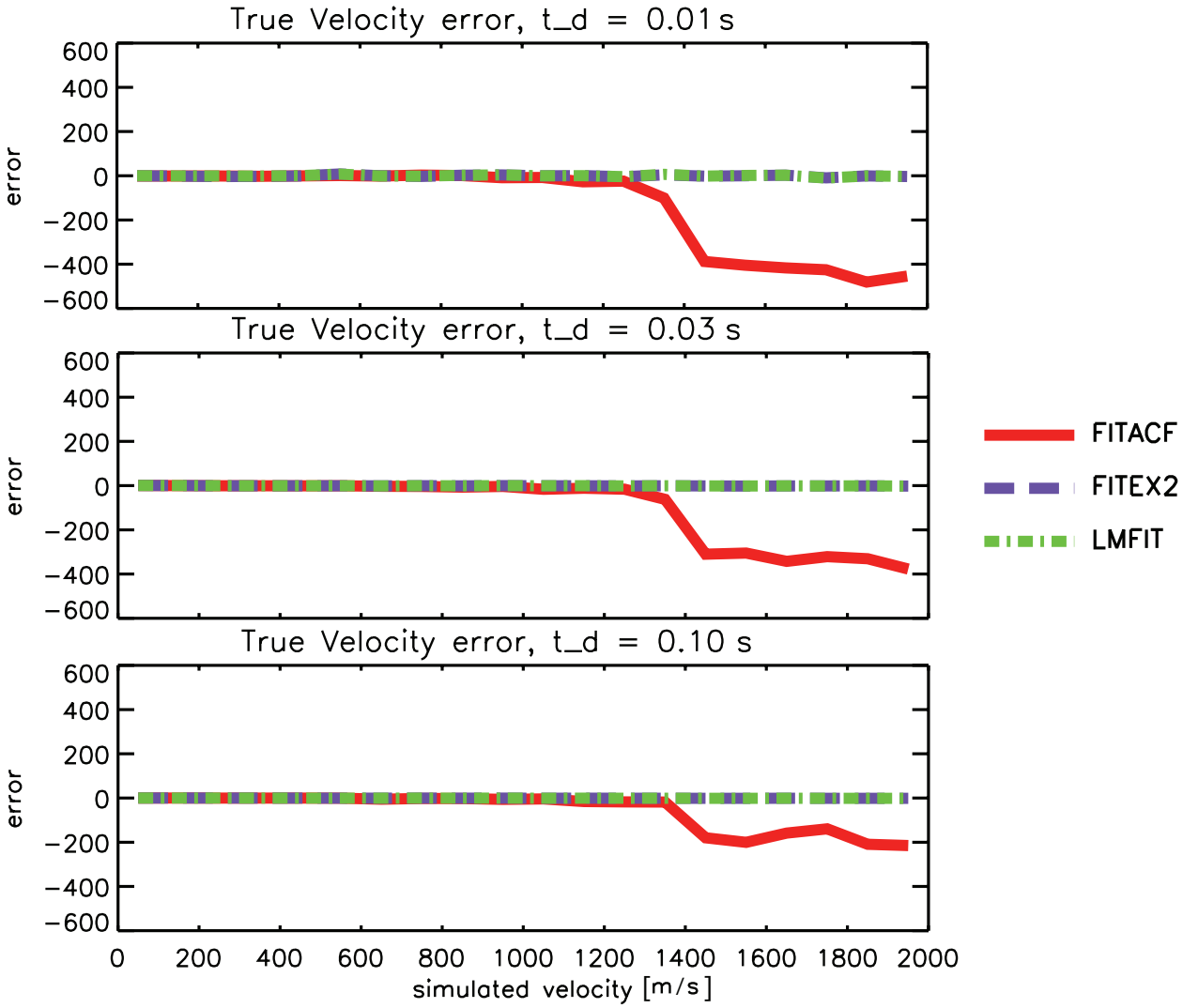

Figure 3.8: True velocity estimate errors for the three fitting routines for three different decay times organized by simulated velocity. The true error is calculated as fitted velocity minus simulated velocity. The display format is the same as in Figure 3.7.

proxy to estimate the location of the open-closed magnetic field line boundary at auroral latitudes [*Chisham et al.*, 2007].

As was mentioned previously, spectral width error is examined in terms of decay time, because this is the more fundamental parameter in (3.4). Also, only the RMS error is considered, because none of the three routines exhibit a bias in terms of average true error.

RMS

The results of this comparison can be seen in Figure 3.9, which shows σ_t (Equation (3.8)) for all three fitting routines. We found that, in contrast to σ_v, the absolute values of RMS decay time errors are approximately proportional to the input t_{d0} value, so we show errors normalized by the respective simulated decay time, t_{d0}. Panels are shown for $v_0 = 50$, 1050, and 1950 m/s. It is apparent that simulated velocity does not have a strong effect on the quality of the decay time estimates. In general, LMFIT provides better decay time estimates than FITACF, and is also noticeably better than FITEX2 for $t_d < 0.3$ s. None of the three routines, however, exhibit very poor performance.

3.4.3 Calculation Efficiency

Another factor which must be considered is which fitting routine is more stable and produces a larger percentage of valid fits. After all, a routine might be able to estimate all parameters perfectly, but if it can only fit one out of every ten ACFs which contain backscatter, it is essentially useless. In order to test this, again all three routines were run on the file with the 100000 simulated ACFs. FITACF produced 99714 good fits, while FITEX2 and LMFIT both produced 99703 good fits. The fact that LMFIT and FITEX2 have the same number of fits is a direct result of LMFIT using a FITEX style process for obtaining an initial velocity guess. Regardless of this, all three routines produce a similar number of good fits.

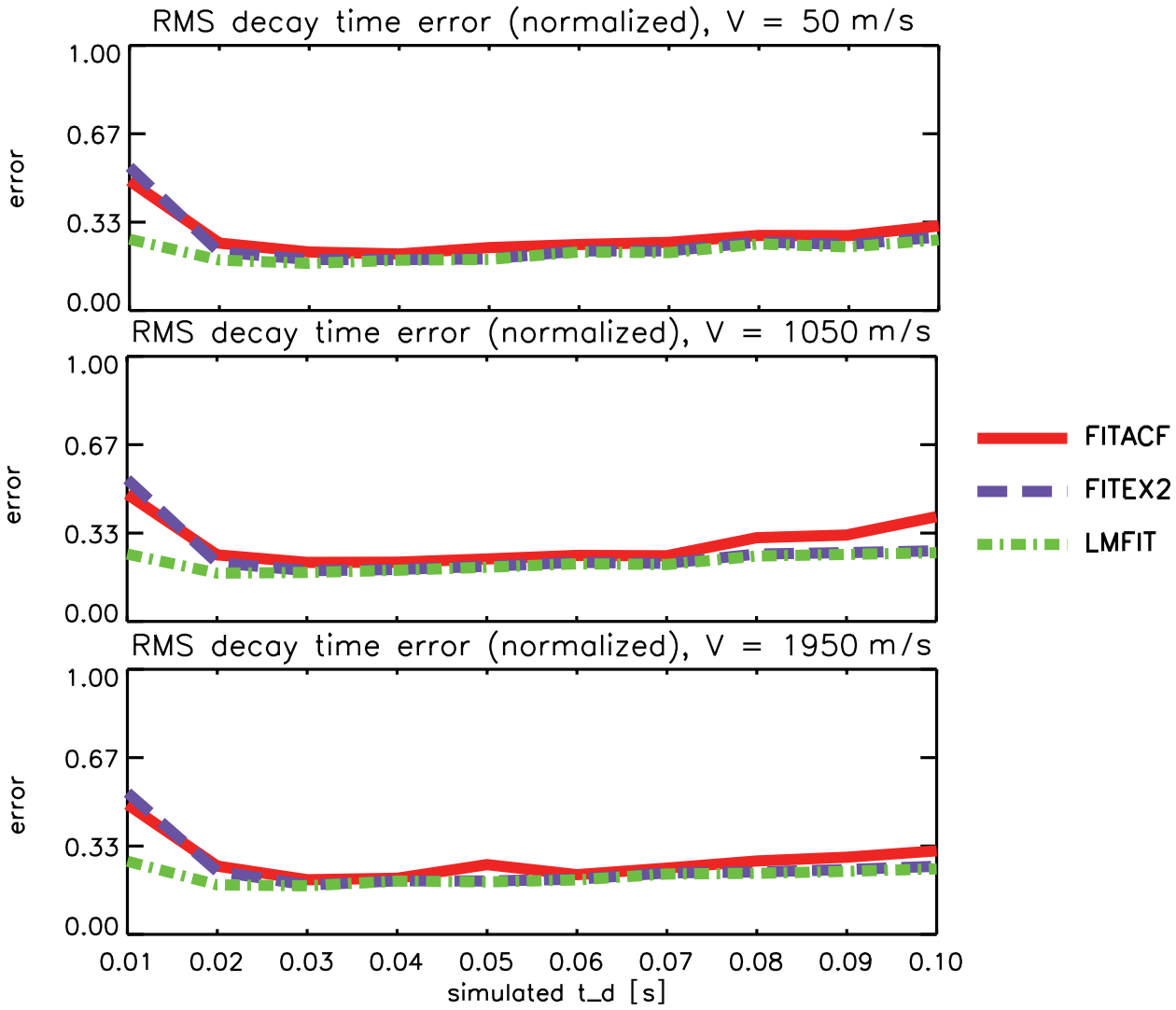

Figure 3.9: RMS decay time estimate errors for the three fitting routines for three different simulated Doppler velocities. The display format is the same as in Figure 3.7.

3.5 Discussion

The major finding of this work is that FITACF velocity fitting is inferior to the other two routines at velocities in excess of 1 km/s. The root of this problem lies in the fact that an initial guess for 2π phase cycles is made. FITACF uses lags 1-4 to make an initial guess on the number of 2π phase jumps to be expected across the entire lag time extent of the

ACF. When the velocity magnitude exceeds 1 km/s, the first 2π "flip" occurs within these four lags so that missing one or two lags can lead to a wrong initial guess. This effect is illustrated in Figure 3.10, which represents phases of two ACFs simulated with the input velocity $v = 1750$ m/s. In the top panel only lag one is bad so that FITACF performs an accurate fit and perfectly reproduces the simulated velocity value. In the bottom panel both lags one and two are bad so that the use of the remaining lags three and four produce wrong guesses on both the magnitude (generally lower in magnitude) and the sign of the phase slope. Ultimately, this leads to a bad velocity estimate of -383 m/s. As we mentioned before, FITEX2 and LMFIT do not use the four-lag guess procedure so they are not affected by this artifact.

Another noticeable effect is that the magnitude of the σ_v generally decreases with increasing t_{d0}. This is true of all three fitting routines, and occurs because the velocity fitting is sensitive to decay time. As lag power decreases, the statistical fluctuation level σ_P remains constant, and makes up a larger portion of the signal level in the ACF, which causes increased uncertainty in the phase fit. This calculation is illustrated in Equation (3.9). Thus, as t_d decreases, the number of lags with lower power increases, resulting in higher uncertainty in the phase fit.

$$\phi(\tau) = \tan^{-1} \frac{Im\{R(\tau)\} \pm \sigma_{Re}}{Re\{R(\tau)\} \pm \sigma_{Im}} \tag{3.9}$$

The third significant finding is that, except in the case of FITACF at high velocities, σ_v is independent of the velocity itself. The reason for this is that, while the statistical errors for ACF power depend on power itself, i.e. $\sigma_P = R_0/\sqrt{N_{avg}}$, ACF phase is an arbitrary parameter so its fluctuations cannot depend on the phase magnitude. In fact, they are

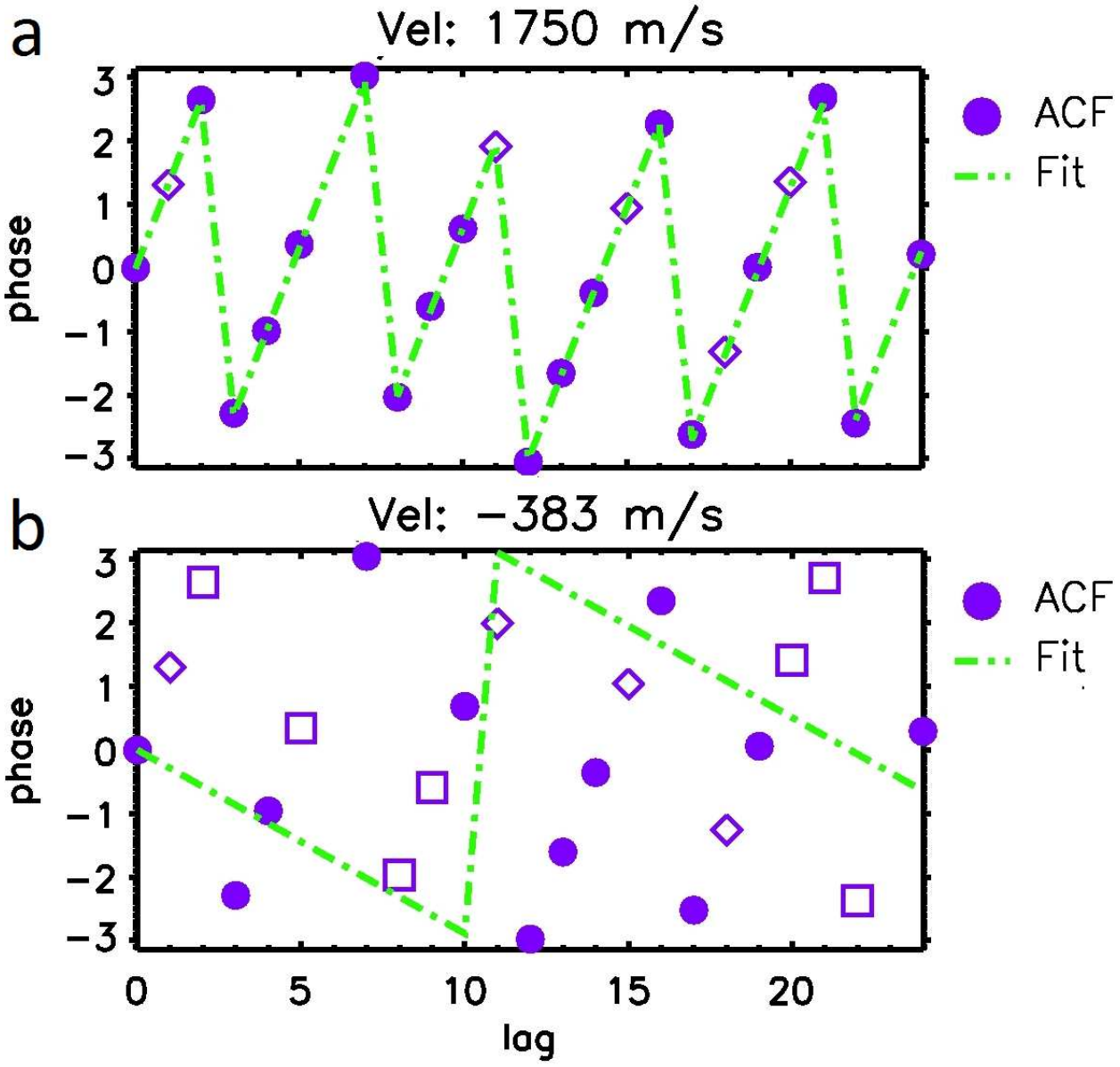

Figure 3.10: An example of a Bad FITACF velocity fit. (a) shows a good phase fit of a simulated ACF with a velocity of 1750 m/s. (b) shows a bad phase fit of a simulated ACF with a velocity of 1750 m/s.

also determined by the ACF power (more specifically, correlation coefficient) at a given lag [*Bendat and Piersol*, 1986]. Therefore, theoretically one would not expect to observe velocity magnitude effects on statistical fluctuations of any estimated parameters, including t_d.

Conversely, σ_t is fairly constant across all tested values of t_{d0}. The proportionality of non-normalized decay time errors, σ_d, to t_{d0} can be illustrated using the propagation of ACF power errors onto decay time. In estimating t_d, we are looking for a point on the time lag axis which corresponds to the e-fold decay of ACF power. The propagation of errors method gives us a respective decay time uncertainty, $\sigma_d = \sigma_P \left|\frac{\partial t_d}{\partial R}\right|$. We are interested in the decay time error at $\tau = t_d$. With changing t_d the power uncertainty, σ_P, remains essentially constant but the derivative term (inverted slope of $P(\tau)$ at $\tau = t_d$) increases or decreases proportionally so that $\sigma_d \propto t_d$. Detailed theoretical analysis of statistical fluctuations lies beyond the scope of this manuscript, but we plan to address it in a future paper.

Table 1 presents a summary of the performance characteristics of all three fitting routines. Note that some of the errors presented here have been normalized by the simulated parameters. For example, a normalized decay time error is calculated as $|t_0 - t|/t_0$. Mean and median errors are shown for velocity and decay time. In both median and mean comparisons, LMFIT has the lowest errors for all fitted parameters. Although several of the results are very close the results are unanimous. The sole weakness of LMFIT is a longer run time. Future work could focus on developing a new method of providing LMFIT with an initial velocity guess in order to sever the tie to FITEX, possibly eliminating the bad fits seen in the top panel of Figure 3.7.

3.6 Summary and Conclusions

After examination of the error characteristics and effectiveness at extracting estimates from ACFs, we conclude that LMFIT is the fitting routine which generally performs best in estimating ionospheric parameters on the basis of SuperDARN radar measurements. The

conventional routine FITACF performs very well at $|v| \leq 1000$ m/s, but at higher velocities eventual data contamination at the shortest lags causes it to produce systematically poor estimates. In sum, LMFIT significantly outperforms FITACF and slightly outperforms FITEX2. Finally, we note that the findings and routines reported here are applicable to other multipulse radar systems that have been designed to overcome the range ambiguity/velocity aliasing dilemma.

3.7 Acknowledgments

The authors thank the National Science Foundation for support under grants AGS-0849031 and AGS-0946900.

Chapter 4

Nightside quiet time midlatitude ionospheric plasma convection measured by the North American midlatitude SuperDARN radars.

A.J. Ribeiro,[1] J. M. Ruohoniemi,[1] J. B. H. Baker,[1] S. de Larquier,[1] S. Shepherd,[2] R. A. Greenwald[1]

1: The Bradley Department of Electrical and Computer Engineering, Virginia Tech, Blacksburg, Virginia, USA.

2:Thayer School of Engineering, Dartmouth College, Hanover, New Hampshire, USA

Abstract

Expansion of the Super Dual Auroral Radar network to midlatitudes has provided new opportunities to study the large-scale dynamics of midlatitude ionospheric electric fields. The radars run continuously and cover a large field of view, meaning that ionospheric dynamics can be analyzed over a larger area than previously possible. We have taken two years of quiet-time, nightside radar data from the six North American midlatitude SuperDARN radars and generated average convection patterns. The electric fields responsible for the plasma drifts are likely generated by the F region dynamo. We find that in general, the zonal flows are much larger than the meridional flows and plasma drifts are primarily westward throughout the night. The measurements presented here are in good agreement with previous studies and empirical models which used data from ISRs. A new result is the identification of a large latitudinal gradient in the winter zonal flows. Large electron densities in the southern hemisphere suggest that this gradient is likely due to conjugate effects, and we discuss a possible mechanism for generation of this feature involving the F region dynamo.

4.1 Introduction

4.1.1 Background Theory

To first order, midlatitude plasma must corotate with the earth [*Mozer*, 1973; *Kelley*, 2009]. This can be shown as follows. Consider a rotating earth with a rotating neutral atmosphere, and a nonrotating ionosphere. In the nonrotating frame, the neutral wind due to rotation, $\mathbf{U}_R$, drives a current $\mathbf{J} = \boldsymbol{\sigma} \cdot (\mathbf{U}_R \times \mathbf{B})$ where $\boldsymbol{\sigma}$ is ionospheric conductivity, which varies with altitude and $\mathbf{B}$ is the magnetic field. Due to variation in conductivity, the current $\mathbf{J}$ is not divergence-free and a polarization electric field builds up in the nonrotating frame in the conducting region of the ionosphere. This electric field continues to build up until the induced electric field is canceled, such that $\mathbf{J} = \boldsymbol{\sigma} \cdot (\mathbf{E}_R + \mathbf{U}_R \times \mathbf{B}) = 0$. Note that the current disappears when the plasma $\mathbf{E} \times \mathbf{B}$ drift velocity is equal to the rotation velocity of the earth. When we transform back into the rotating frame, we find that $\mathbf{E} = 0$. This means that the electric field in the nonrotating frame causes the ionosphere to corotate with the earth. The neutral atmosphere does not perfectly corotate with the earth, however, as there are variations in neutral winds. This causes midlatitude plasma to deviate from perfect corotation. The existence of midlatitude plasma drifts in the rotating frame thus indicates that electric fields must also be present.

Quiet-time midlatitude F region electric fields have long been thought to be caused by the dynamo action of the neutral winds [*Rishbeth*, 1971; *Richmond et al.*, 1976; *Fejer*, 1991; *Buonsanto et al.*, 1993]. The mechanism behind the generation of dynamo electric fields is not dramatically different from the mechanism which drives corotation. The basic idea behind dynamo theory is described in *Rishbeth and Garriott* [1969]. When a wind, $\mathbf{U}$, blows

across the geomagnetic field, it drives a current equal to

$$\mathbf{J} = \boldsymbol{\sigma} \cdot (\mathbf{U} \times \mathbf{B}) \tag{4.1}$$

where $\boldsymbol{\sigma}$ is the tensor conductivity. This current does not necessarily satisfy the condition $\nabla \cdot \mathbf{J} = 0$, which causes charge to accumulate in regions where this condition is not satisfied. This causes an electrostatic polarization field which makes the current nondivergent. Additionally, charge will accumulate at the top and bottom of the conducting layer because the current cannot flow into a region of low conductivity. This induces an electric field which forces the current flow to be horizontal.

Because the current is horizontal we can now use the layer conductivity, σ', and the total electric field, $\mathbf{E}_t$, to describe the current:

$$\mathbf{j} = \boldsymbol{\sigma}' \cdot \mathbf{E}_t = \boldsymbol{\sigma}' \cdot (\mathbf{U} \times \mathbf{B} - \nabla\Phi) \tag{4.2}$$

where $-\nabla\Phi$ is the electrostatic polarization field, $\mathbf{E}_p$. This polarization electric field is typically on the order of a few millivolts per meter. An additional simplification can be made if one assumes that $\mathbf{U}$ and $\mathbf{B}$ are independent of height through the conducting region. This allows for the use of height integrated conductivity, $\boldsymbol{\Sigma}'$, such that

$$\mathbf{J} = \boldsymbol{\Sigma}' \cdot (\mathbf{U} \times \mathbf{B} - \mathbf{E}_p). \tag{4.3}$$

In steady state, with a fully formed polarization electric field, the polarization field cancels the field due to the wind, such that $\mathbf{E}_p = -\mathbf{U} \times \mathbf{B}$ and $\mathbf{J} = 0$. In this case, the plasma and the neutrals drift together in the directions perpendicular to the magnetic field [*Burnside*

et al., 1983]

The dynamo effect which has been described can occur in either the E or F regions of the ionosphere. During the day, any $\mathbf{E}_p$ which is set up in the F region is thought to be neutralized by current flow between the F and the more highly conducting E region. The midlatitude plasma drifts which will be discussed in this paper occur mainly at night. At night time, the upper thermospheric winds are relatively large and the E region conductivities are small. Because of this, the dominant night time driver of convection is generally thought to be the F region dynamo.

Large values of parallel conductivity allow large-scale electrostatic fields to map between the hemispheres [*Burnside et al.*, 1983; *Fejer*, 1993; *Buonsanto et al.*, 1993]. Since dynamo processes can be occurring simultaneously in conjugate hemispheres, the polarization fields can be mapped between hemispheres. The hemisphere with the larger conductivity determines the dominant electric field and hence the local electric field in the conjugate hemisphere. *Burnside et al.* [1983] found that drift velocities observed by the Arecibo ISR were well explained by dynamo theory, provided that electrostatic fields from the conjugate hemisphere were considered.

4.1.2 Previous Work

Historically, studies of midlatitude convection have been done using data from incoherent scatter radars (ISRs), and specifically, the Millstone Hill ISR. Two such studies are *Richmond et al.* [1980] and *Buonsanto et al.* [1993]. *Richmond et al.* [1980] presented quiet time drift observations from four ISRs and derived a global empirical model, but we will focus on their results from Millstone Hill, and specifically the nighttime zonal drifts.

Richmond et al. [1980] used Millstone Hill measurements centered on 57° magnetic latitude. In all seasons (winter, summer, equinox), they found westward plasma drifts throughout the night. In the winter, the eastward velocities peaked at about -50 m/s around midnight MLT and approached 0 m/s towards dusk and dawn. In summer, they also found westward plasma drifts throughout the night but varying between about -20 and -50 m/s eastward with MLT. At equinox, they again found westward plasma drifts throughout the night, with the velocities peaking at about -35 m/s at midnight and approaching 0 m/s towards dusk and dawn.

Buonsanto et al. [1993] performed a similar study to *Richmond et al.* [1980], again using Millstone Hill ISR measurements and found similar results for the zonal plasma drifts. *Buonsanto et al.* [1993] showed a diurnal variation in the meridional plasma drifts. In general, they found northward drifts from about 0-12 LT, maximizing at about 20 m/s, southward drifts of about 10 m/s from 12-20 LT, and small positive drifts from 20-24 LT, regardless of season. *Buonsanto et al.* [1993] also found some solar cycle dependencies in the drift patterns for all three seasons. They explained the differences in zonal drifts between summer and winter as a result of variations in the dynamo electric fields in the local and conjugate hemispheres. In winter, the conjugate points to the Millstone Hill nighttime measurements are sunlit for a large portion of the night, meaning that the southern hemisphere has the dominant conductivity.

In this study, we aim to derive and analyze statistical midlatitude convection patterns covering a larger latitudinal swath than was possible previously. ISRs only provide spatial coverage within a few hundred kilometers range from the radar. As a result, previous studies using ISRs average their measurements and show plasma velocities for only a single point at the center of the field of view. Conversely, SuperDARN radars can make measurements

over thousands of kilometers from the radar, allowing the measurements to be analyzed over a span of latitudes. In addition, ISRs are typically only run for short, intermittent periods, meaning that the statistical patterns in these previous studies were derived using a relatively small number of measurements. The power requirements of SuperDARN radars are such that they run continuously and large quantities of data are generated in relatively short times.

Baker et al. [2007] presented a study of midlatitude convection patterns using midlatitude SuperDARN data. These results disagreed with previous studies performed using Millstone Hill ISR data because of ground scatter contamination of SuperDARN data. *Ribeiro et al.* [2011] developed a classification algorithm which solved the ground scatter problem. In this paper, we present new convection patterns derived from two years (2011-2012) of midlatitude radar data from six different radars processed using the algorithm of *Ribeiro et al.* [2011]. We compare our derived patterns with those previously reported in *Richmond et al.* [1980] and *Buonsanto et al.* [1993]. Additionally, we compare the patterns to and empirical convection model presented by *Richmond et al.* [1980]. We will see that the convection patterns derived using SuperDARN are in good agreement with previous studies and empirical models.

4.1.3 Dataset

The Super Dual Auroral Radar Network (SuperDARN) is an international chain of phased-array HF radars which monitor plasma dynamics in the E and F regions of the ionosphere [*Greenwald et al.*, 1985; *Chisham et al.*, 2007]. During normal operation, the radars scan across 16-24 azimuthal look directions (beams) separated by 3.24°, and have 75-100 range gates, separated by 45 km. The targets for SuperDARN radars are decameter scale plasma irregularities, which are density structures caused by plasma instability processes [*Fejer and*

Kelley, 1980; *Keskinen and Ossakow*, 1983; *Tsunoda*, 1988]. In the F region, the plasma irregularities drift at the $\mathbf{E} \times \mathbf{B}$ velocity [*Ruohoniemi and Baker*, 1998].

SuperDARN radars have historically been built at ≈60° latitude in order to maximize coverage of the auroral oval. With the construction of the radar at Wallops Island, Virginia, USA, SuperDARN F region coverage expanded to latitudes as low as 50° magnetic latitude. This was prompted by the need to improve coverage of the expanded auroral oval during storm periods [*Baker et al.*, 2007]. Soon after its construction, an unexpected type of nightside F region irregularity was observed frequently, and was first reported by *Greenwald et al.* [2006]. These radar echoes were observed on most geomagnetically quiet nights, exhibited Doppler velocities and spectral widths typically in the tens of meters per second, and were thought to be backscatter from F region irregularities.

Because of the low Doppler velocity and spectral width of the backscatter from these irregularities, they proved difficult to distinguish from ground echoes in an automated manner. Ground echoes occur when the radar signal experiences enough refraction in the ionosphere to bend it back down to the ground, where the signal reflects back to the radar. *Ribeiro et al.* [2011] demonstrated a new classification algorithm for identifying this type of low velocity ionospheric backscatter. Subsequently, a statistical study was performed by *Ribeiro et al.* [2012] which confirmed that this type of backscatter was observed only on the nightside and demonstrated that the irregularities were both subauroral and equatorward of the ionospheric projection of the plasmapause. Using ray-tracing analysis, *de Larquier et al.* [2013] was then able to show that the irregularities responsible for this subauroral ionospheric scatter do in fact reside in the F region.

We have processed data collected from the North American midlatitude SuperDARN radars in 2011-2012 with the classification algorithm of *Ribeiro et al.* [2011], and selected for only

low-velocity events as was done in *Ribeiro et al.* [2012]. The fields of views of the radars are shown in Figure 4.1. Selecting for only low velocity events serves to filter out data which could be auroral in nature. Furthermore, we have selected for periods with $Kp < 3$, and only used data from magnetic latitudes between 52° and 58°. The lower boundary was chosen because it is approximately the lowest latitude at which the radars generate F region measurements, and the upper boundary was chosen to be below the usual equatorward boundary of the auroral zone during quiet-time [*Ribeiro et al.*, 2012].

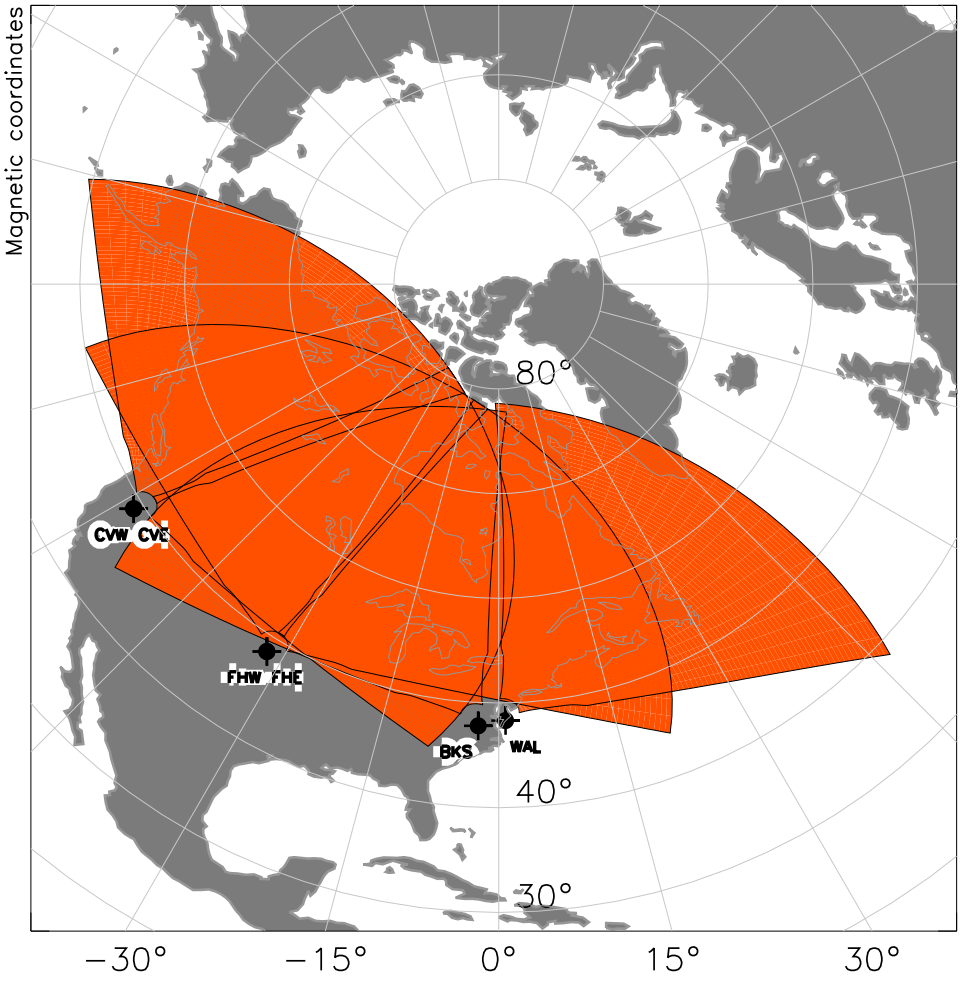

Figure 4.1: Fields of views of the six North American midlatitude radars used in this study. From west to east, the radars are: Christmas Valley West, Christmas Valley East (Oregon), Fort Hays West, Fort Hays East (Kansas), Blackstone, and Wallops Island (Virginia).

4.2 Convection Mapping

In order to generate average convection patterns from SuperDARN data, some processing is done on the Doppler velocity data. Data are binned into magnetic latitude-magnetic local time (MLT) grid, similar to what was done by *Ruohoniemi and Baker* [1998]. This grid can be seen in Figure 4.2. The grid cells are 1° latitude by whatever MLT span makes the cell closest to a square while allowing for an integer number of cells to span 24 hours in MLT at that latitude. Over the course of the night, the plasma drift within a cell is viewed over a range of radar look directions. Because of this, within each grid cell, Doppler measurements are binned by azimuth in 10° increments. The azimuth bins are shown as an inset in Figure 4.2.

The convection mapping starts by binning data from a single radar in magnetic latitude, MLT, and azimuth. The velocity data is averaged over ten minute (UT) intervals, that is, ten minutes of data from a single radar is binned, and the median vector in each azimuth bin within each grid cell is chosen to be the velocity for that ten minute time interval. This is done for each individual radar for each day during the 2011-2012 time period.

Once this processing step is done, the data from all radars is combined into a single master grid. This grid contains all of the ten minute averaged vectors from all six North American radars from the two year time interval. Next, the median velocity within each azimuth bin within each master grid cell is chosen to be the typical line-of-sight velocity at that magnetic latitude, MLT, and azimuth. Because the radar line-of-sight (LOS) velocity is the projection of a two-dimensional flow vector onto the radar beam azimuth, there is a cosine variation of velocity with azimuth. Therefore, to solve for the average two-dimensional flow vector in each grid cell, a cosine function is fit to the variation of line-of-sight velocity with azimuth

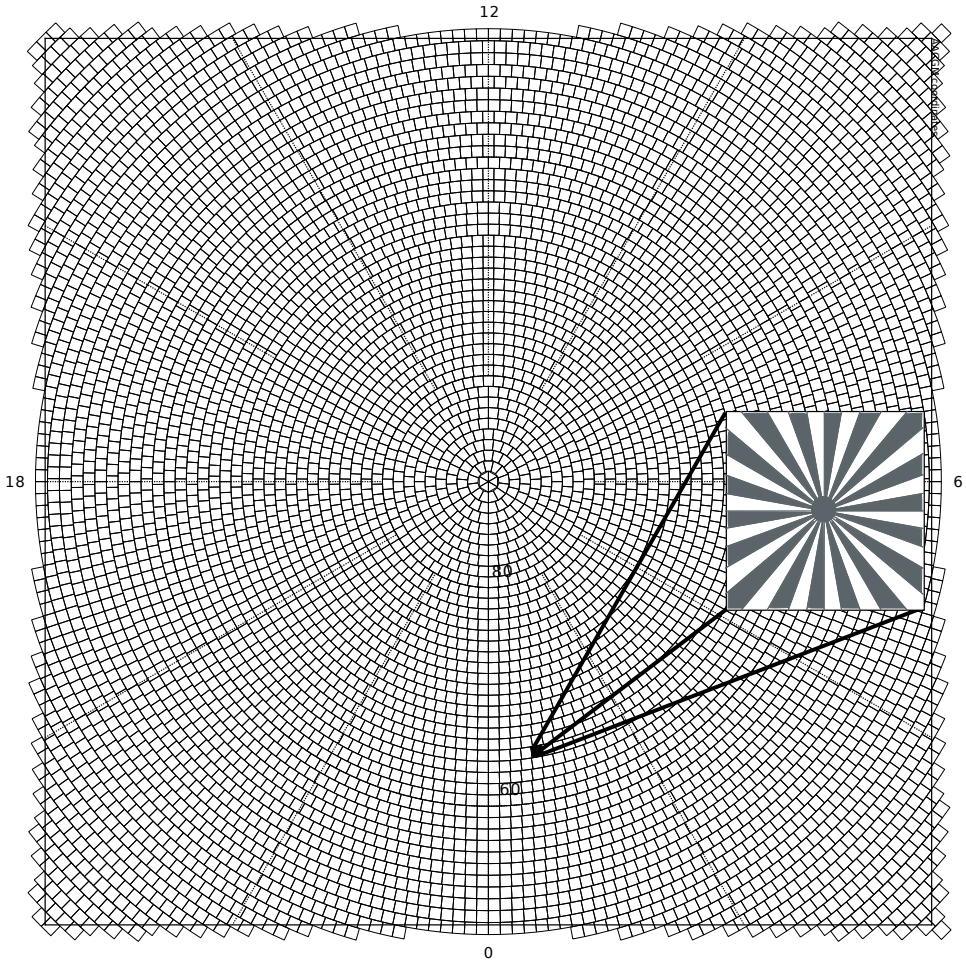

Figure 4.2: A view of the grid used for convection mapping. The size of the grid cells is 1° in magnetic latitude by the magnetic local time span which makes the cell closest to a square. Inset is an expanded view of the 10° azimuth bins within each grid cell.

in each cell using the non-linear least squares fitting routine in the Numpy Python library [*Dubois et al.*, 1996; *Ascher et al.*, 1999]. An example of such a fit is shown in Figure 4.3 with Doppler velocity on the y-axis and azimuth in degrees shown on the x-axis. The typical velocity value within each azimuth bin is plotted as a circle, with the size of the circle proportional to $1/\sqrt{n}$ where n is the number of measurements within each azimuth bin. The fit is weighted by a factor of $1/\sqrt{n}$ so that the most reliable medians are given preference. The best fit line is plotted as a gold curve, and the resulting two-dimensional velocity is plotted as a red star.

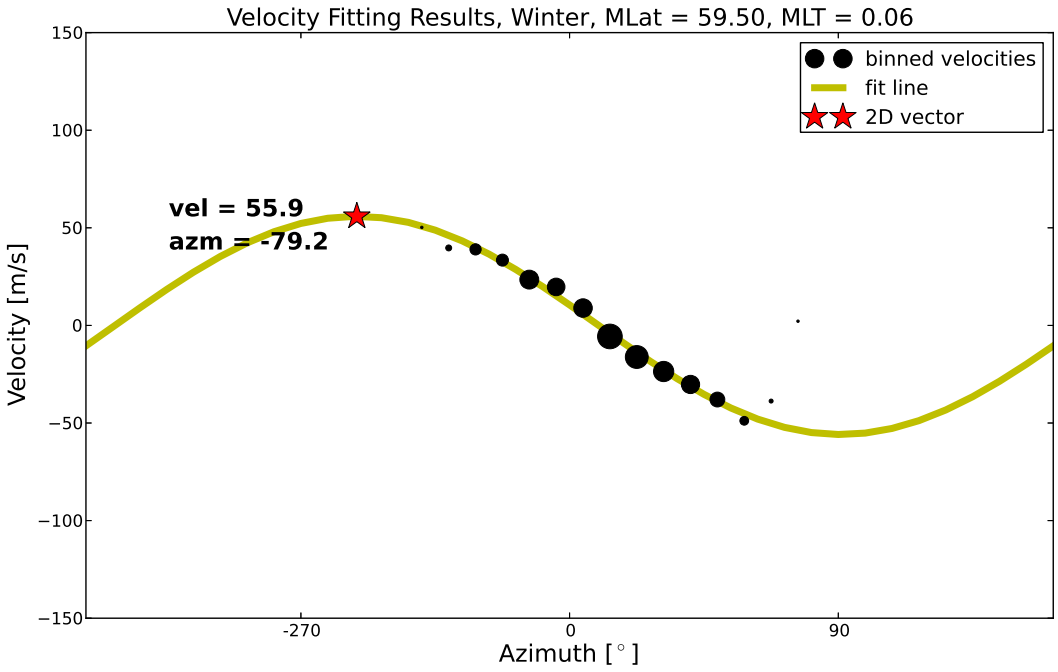

Figure 4.3: An example of fitting a cosine to the typical line-of-sight velocities in each azimuth bin within a single grid cell. The median Doppler velocities at each azimuth are plotted as black circles, and the size of the circle is proportional to the square root of the number of measurements within each bin. The fit is weighted by this factor, so the larger circles are fit more closely than the small ones. The best-fit cosine is shown in gold, and the resulting flow vector is plotted as a red star. Here, the result of the fit is a two-dimensional vector with a velocity magnitude of 55.8 m/s and an azimuth of 281.9.

4.3 Results

The resulting convection patterns, separated by season (winter: November-February; summer: May-August; equinox: March-April, September-October), are shown in Figures 4.4a, b, c. These maps are centered on 0 MLT. Figures 4.5a, b, c show the number of measurements in each grid cell. It is worth noting that there is significant variation between seasons. In general, the highest velocities occur in winter and the lowest in summer. For all seasons, the flow is predominantly westward throughout the night, which indicates a predominantly

northward electric field. The zonal flows are typically on the order of 20-40 m/s, while the meridional flows are on the order of 10 m/s. Near the dawn and dusk boundaries, the patterns begin to exhibit erratic behavior. As shown in Figure 4.5 this is probably due to decreasing statistical significance of measurements, rather than to actual physical phenomena.

In Figures 4.6 and 4.7, the velocities are plotted again but as lines with a single color-coded line for each 1° latitude interval. This format provides an easy way of comparing the magnitudes of the flows as a function of latitude. Zonal velocities (positive eastward) are shown in Figure 4.6, and meridional velocities (positive northward) are shown in Figure 4.7. It can be seen that in all three seasons, meridional velocities are generally small when compared to the zonal velocities.

It is apparent from Figures 4.6 and 4.7 that the dominant flow throughout the night is westward, which implies a northward electric field. We can then use the solved zonal components of the convection velocities and the relationships $\mathbf{E} = -\mathbf{v} \times \mathbf{B}$ and $\Phi = -\int E \cdot dl$ in order to calculate the potential drop and average electric field across the 52°-58° latitudinal interval at different MLT sectors. The results are shown in Figure 4.8. In this figure, we have used a magnetic field z-component value of 40 μT. We have calculated a single average value of the meridional electric field assuming that the distance between lines of magnetic longitude is 111 km. Although these calculations are somewhat crude, they can give us an idea of the magnitude of the electric fields seen across this interval of magnetic latitude. We can see that, as would be expected from the drift velocities, the largest fields are seen in winter, the next highest in equinox, and the smallest in summer. In winter, the maximum is seen at midnight at 2 mV/m. In equinox, again the maximum is seen at midnight, and the average electric field value is about 1.2 mV/m. In summer, the largest electric fields are seen pre-midnight, and has a maximum value of about 1 mV/m.

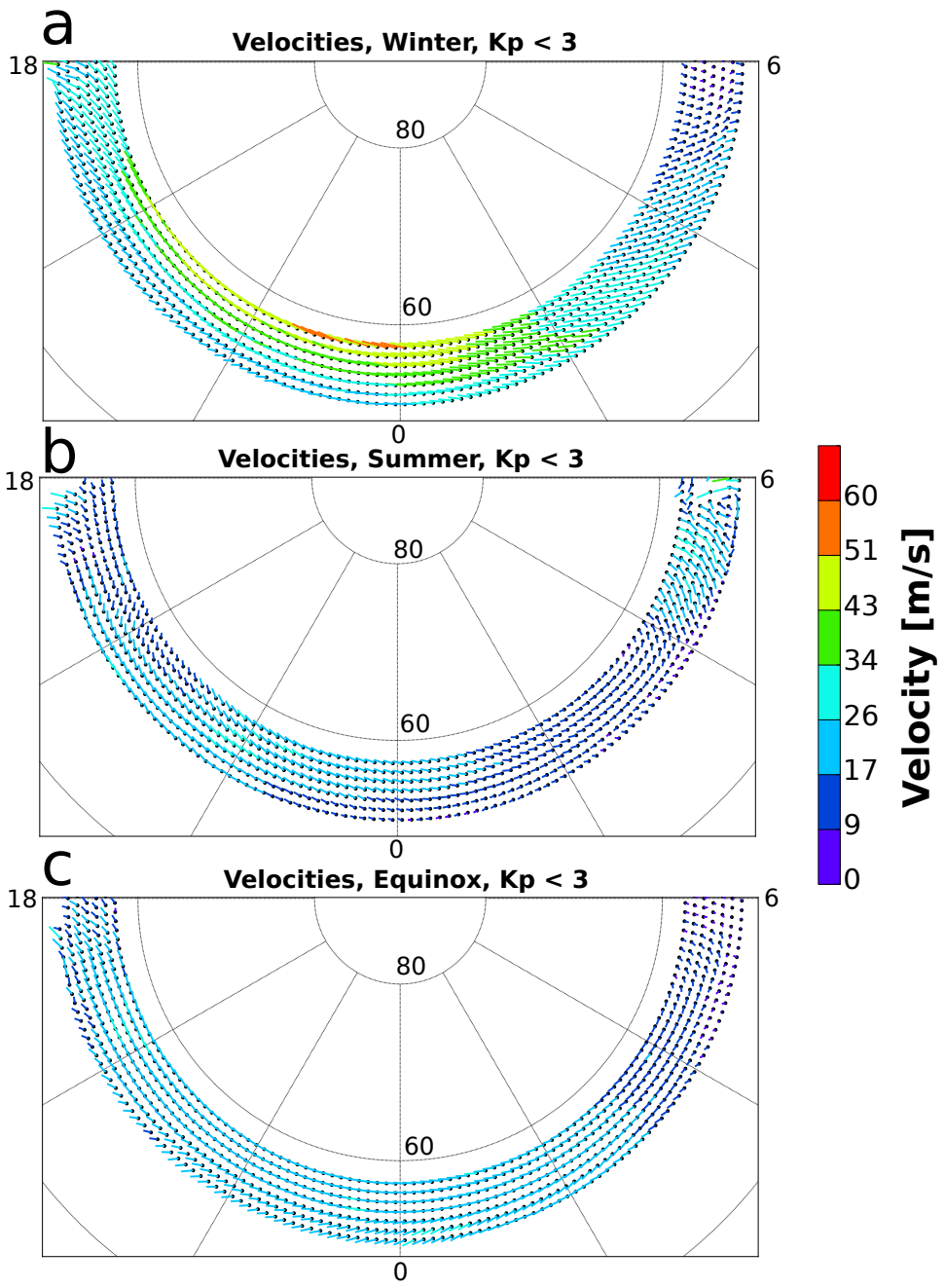

Figure 4.4: Panels a, b, and c show the convection patterns which were calculated for winter, summer, and equinox, respectively. Note that the patterns get a bit erratic for all seasons on the dawn and dusk fringes, which is probably due to a lack of measurements, and not due to actual physical processes.

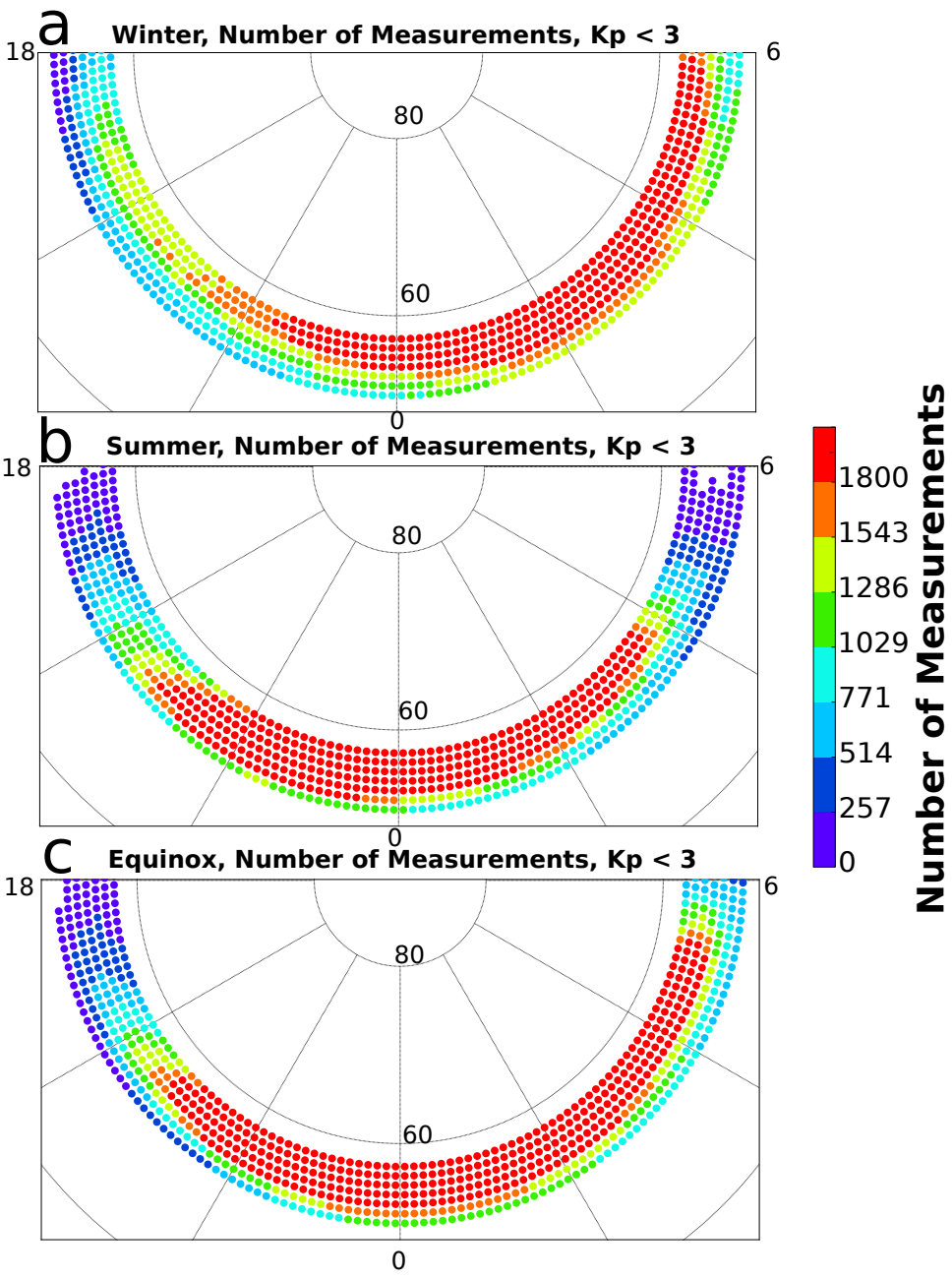

Figure 4.5: Panels a, b, and c show the number of measurements in each grid cell which went into the calculation of the patterns shown in Figure 4.4

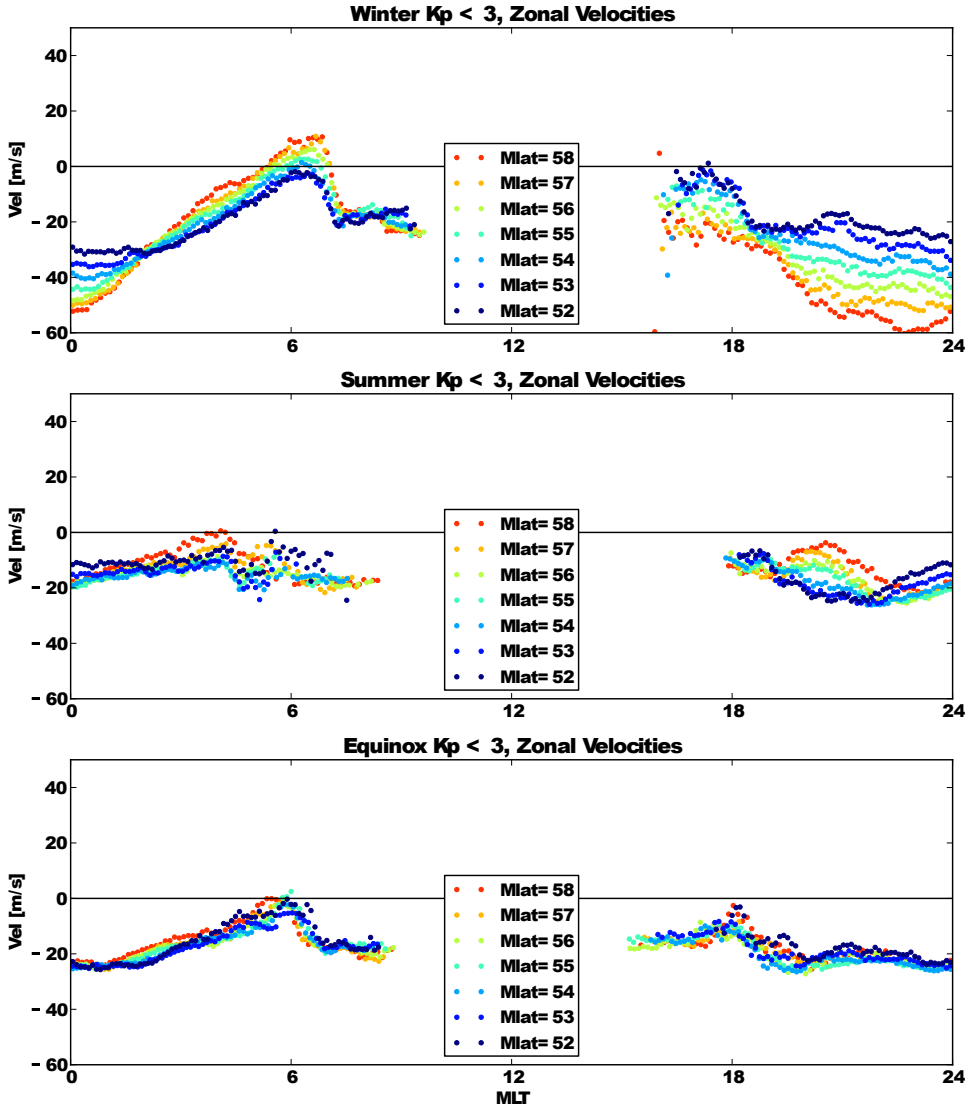

Figure 4.6: Fitted zonal velocities by latitude (positive eastward). The top row shows the results for winter, the middle row shows the results for summer, and the bottom row shows the results for equinox. Note that the plots are centered on midnight MLT.

4.4 Discussion

4.4.1 Data Comparison

It is worthwhile to compare the results presented here with the previous studies. The zonal velocities shown in Figures 4.6 and 4.7 are in very good agreement with those calculated using

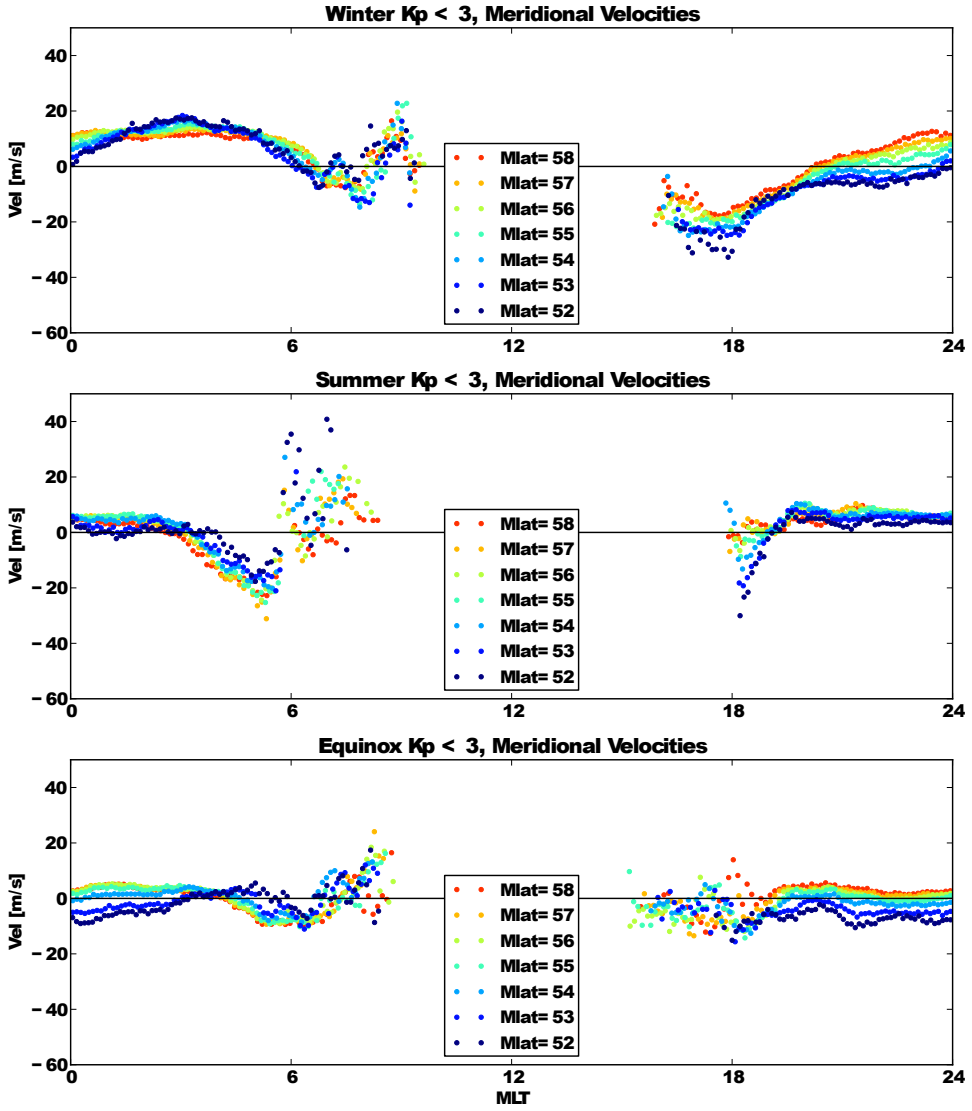

Figure 4.7: Fitted meridional velocities by latitude (positive northward). The top row shows the results for winter, the middle row shows the results for summer, and the bottom row shows the results for equinox. Note that the plots are centered on midnight MLT.

the Millstone Hill ISR reported in *Richmond et al.* [1980] and *Buonsanto et al.* [1993]. The zonal flows reported by *Richmond et al.* [1980] are plotted as individual points in Figure 4.9. The top panel shows winter, the middle panel shows summer, and the bottom panel shows equinox. The zonal flows reported by *Buonsanto et al.* [1993] are shown in Figure 4.10. The meridional velocities are also in good agreement with those calculated using data from

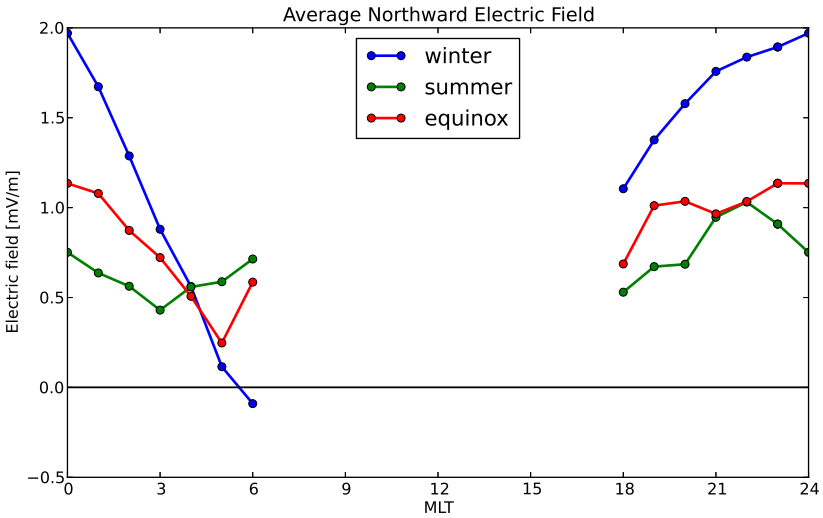

Figure 4.8: Average northward electric fields observed by the SuperDARN radars throughout the night. Assuming a magnetic field z-component of 40 μT and 111 km separation between lines of magnetic longitude, the total potential drop is calculated for one-hour MLT steps, and then the average electric field is found by dividing my the distance. Winter is plotted in blue, summer in green, and equinox in red.

Millstone Hill in *Buonsanto et al.* [1993], which are shown in Figure 4.11. Note, that the meridional velocities cannot be compared with the results presented in *Richmond et al.* [1980] because in that paper, upward/poleward drifts were shown instead of just poleward.

4.4.2 Empirical Model Comparison

Previous studies have derived empirical midlatitude convection patterns from Millstone Hill data (e.g. *Richmond et al.* [1980]; *Wand* [1981]). We will make comparisons between the northward electric field in this paper, as shown in Figure 4.8, and the empirical model reported by *Richmond et al.* [1980], as shown by the solid lines in Figure 4.9. The right side axis shows approximate electric field values, as seen in *Wand* [1981]. In winter, *Richmond et al.* [1980] found a maximum electric field of about 1.5 mV/m around midnight, with a

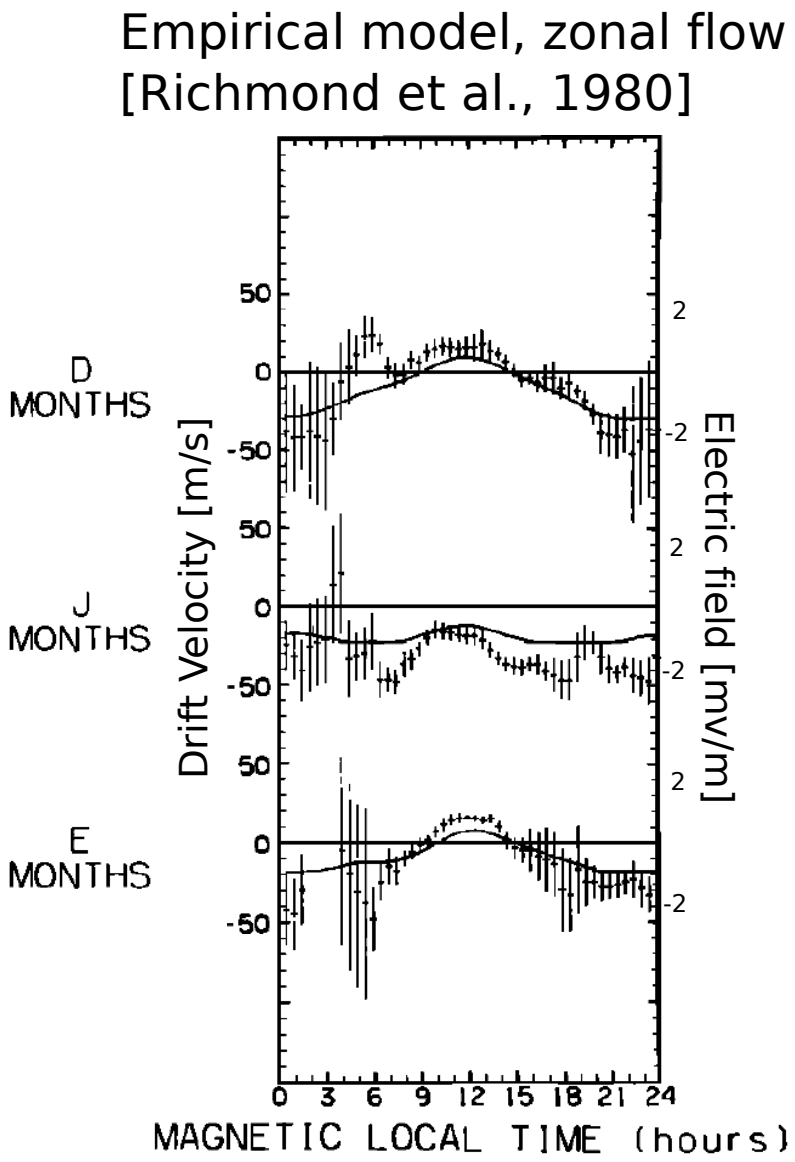

Figure 4.9: Zonal plasma drifts and calculated empirical model drifts reported in *Richmond et al.* [1980]. The individual scatter points represent measured drift velocities, while the smooth curve indicates the velocity predicted by the empirical model. The data used were from the Millstone Hill ISR, centered on 57° magnetic latitude. The right axis shows approximate electric field values, from *Wand* [1981]. Figure from *Richmond et al.* [1980].

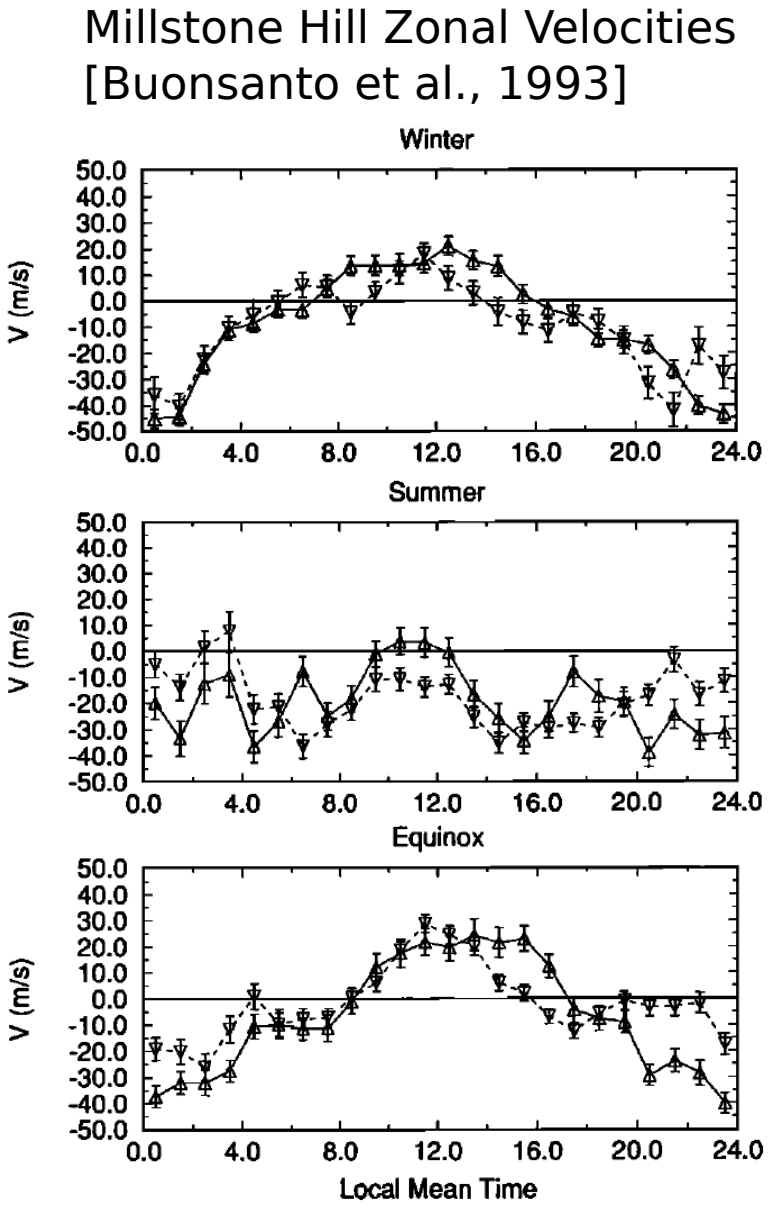

Figure 4.10: Zonal plasma drifts reported in *Buonsanto et al.* [1993]. The upward triangles represent data from solar maximum, and the downward triangles represent data from solar minimum. The data used were from the Millstone Hill ISR, centered on 57° magnetic latitude. Figure from *Buonsanto et al.* [1993].

value of about 1 mV/m at 1800 LT, and crossing 0 mV/m at about 0600 LT. Although the maximum found here is larger than that found by *Richmond et al.* [1980] by about 0.5 mV, the rest of the results are consistent.

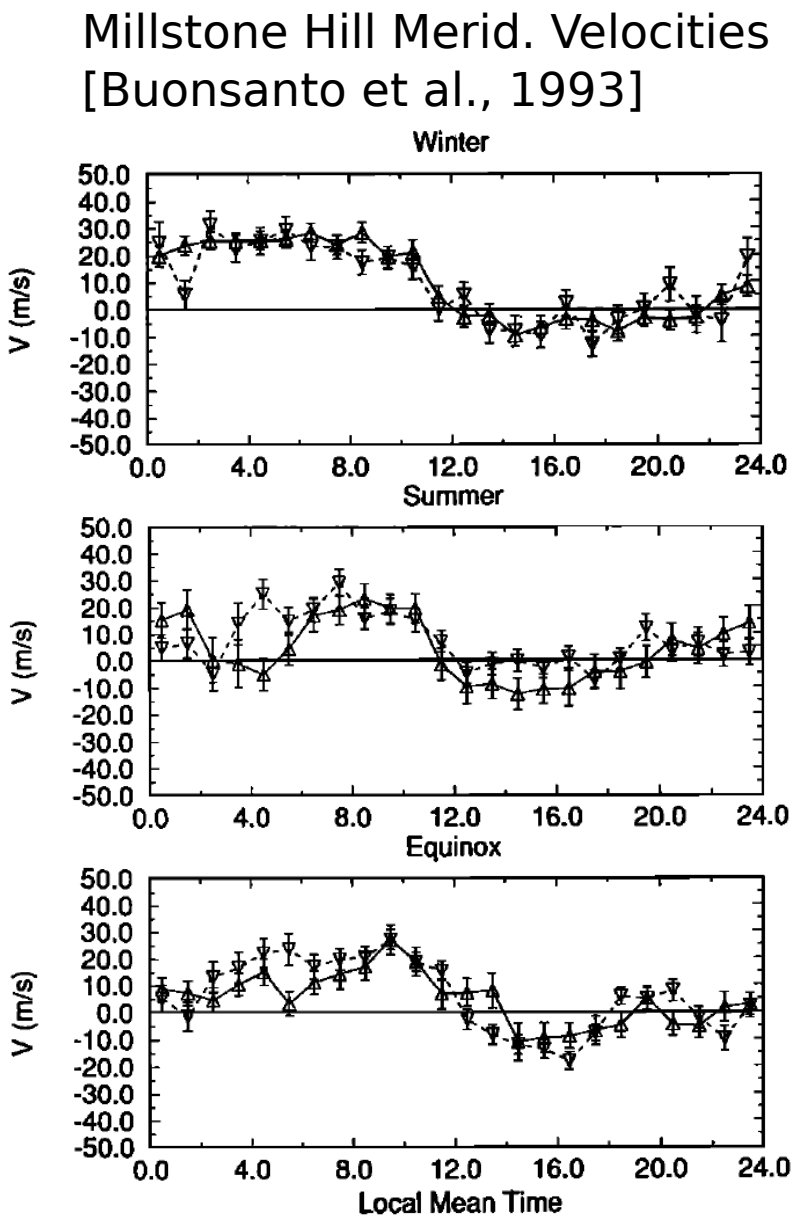

Figure 4.11: Meridional plasma drifts reported in *Buonsanto et al.* [1993]. The upward triangles represent data from solar maximum, and the downward triangles represent data from solar minimum. The data used were from the Millstone Hill ISR, centered on 57° magnetic latitude. Figure from *Buonsanto et al.* [1993].

In summer, *Richmond et al.* [1980] predicts a fairly steady electric field throughout the night at around 1 mV/m. This is in good agreement with our observations. During equinox, *Richmond et al.* [1980] predicts an electric field of about .75 mV/m at 1800 LT, 1 mV/m at

midnight, and slightly less than 1 mV/m at 0600 LT. Again, this is fairly consistent with our observations.

In general, the empirical model of *Richmond et al.* [1980] agrees very well with our observations. Possible causes for any discrepancies are (1) Millstone Hill observes a much smaller latitudinal range than the SuperDARN midlatitude radars, and (2) does not run continuously. Additionally, it is possible that some of the SuperDARN data here has some ground-scatter contamination. In the future, the results presented in this paper can be used to improve empirical models of midlatitude F region dynamics. The results presented here could also be used to improve wind models and thus improve theoretical models, (e.g. *Roble et al.* [1988]; *Richmond et al.* [1992]).

4.4.3 Conjugacy Effects

In Figure 4.6 during winter, there is a large latitudinal gradient in the zonal velocity from about 1800 MLT until just after midnight MLT. We argue that the situation across the terminator in the southern hemisphere is controlling the latitudinal variation in the zonal electric fields seen in the northern hemisphere. As was mentioned earlier, because of the large conductivity of magnetic field lines, conditions in the conjugate hemisphere are important for midlatitude dynamics [*Burnside et al.*, 1983; *Fejer*, 1993; *Buonsanto et al.*, 1993]. In Figure 4.12, we show the conjugate footpoints of the range-beam cells from the North American SuperDARN radars between 52 and 58 degrees magnetic latitude plotted as black dots. These conjugate footpoints have been determined using the Tsyganenko T96 model [*Tsyganenko*, 1995]. We also show the terminator for four different times, 0100, 0400, 0700, and 1000 UT, which correspond approximately to 1800, 2100, 0000, and 0300 LT over the middle of North America. We can see that the conjugate points to much of the collective

field of view of the North American radars is sunlit throughout much of the night, which we would expect would lead to higher conductivities in the southern hemisphere.

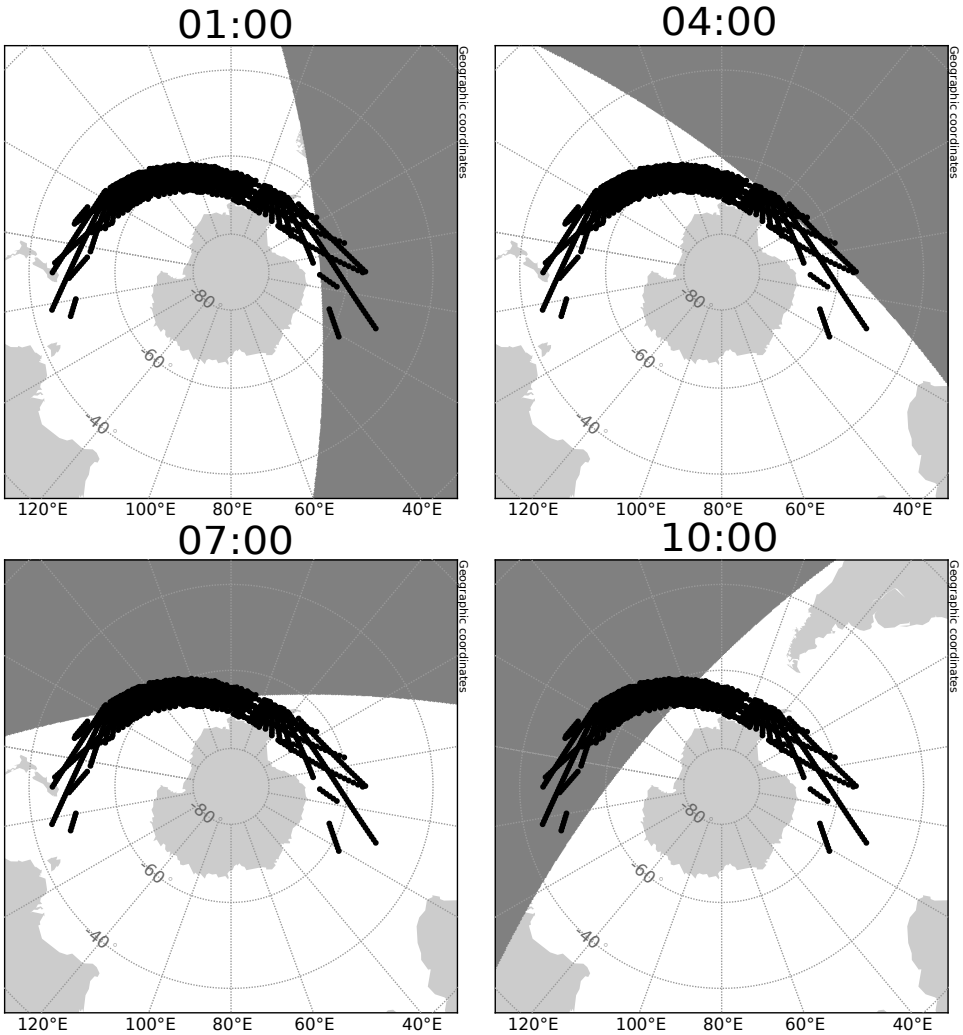

Figure 4.12: A plot of the conjugate of coverage region in winter. The range beam cells of the North American midlatitude SuperDARN radars are plotted as black dots. The four plots are for 0100, 0400, 0700, and 1000 UT, which correspond to approximately 1800, 2100, 0000, and 0300 LT over North America. Note that for much of this period, the coverage region straddles the terminator.

We can see that the region of observations straddles the terminator throughout the night with the peak alignment occurring at 7 UT which corresponds to approximately midnight over central North America. Naively, one might expect a nonlinear increase in plasma density in

the vicinity of the terminator, which could lead to the latitudinal gradient which is observed in the winter panel of Figure 4.6. This is illustrated in Figure 4.13. The red line in the line plot on the right shows the nonlinear Pedersen conductivity profile which we would expect to arise from the nonlinear increase in assumed plasma density. The steps in the dynamo process are as follows:

1. A uniform zonal neutral wind (U_z) blows westward in the vicinity of the terminator.
2. The wind drives a current, $\mathbf{J} = \boldsymbol{\sigma} \cdot (\mathbf{U} \times \mathbf{B})$. Because of the gradient in Pedersen conductivity, this current is not uniform, leading to the three different current values, $\mathbf{J}_1, \mathbf{J}_2, \mathbf{J}_3$.
3. This current is not divergence free, and charge builds up in places where the divergence does not equal zero. If we assume that the wind velocity and magnetic field do not vary with height throughout the conducting region, we can say that $\nabla \cdot \mathbf{J} \propto d\sigma_p/d\Lambda$.
4. The charge accumulation causes polarization electric fields to develop, and because the divergence of the current varies with latitude (blue line in the line plot on the right), so too do the polarization electric fields, $\mathbf{E}_1, \mathbf{E}_2, \mathbf{E}_3$.
5. The polarization electric fields drive zonal plasma drifts V_{z1}, V_{z2}, V_{z3} whose magnitudes vary with latitude due to the latitudinal variation in the polarization electric fields. Note, that the larger velocities are observed at higher latitudes, which is precisely what we observe in the winter panel of Figure 4.6.

In order to test the viability of our hypothesis, we have examined electron density as predicted by IRI [*Bilitza*, 2001]. Figure 4.14 shows IRI electron densities along the 100° west meridian at approximately midnight over North America for the northern and southern hemisphere

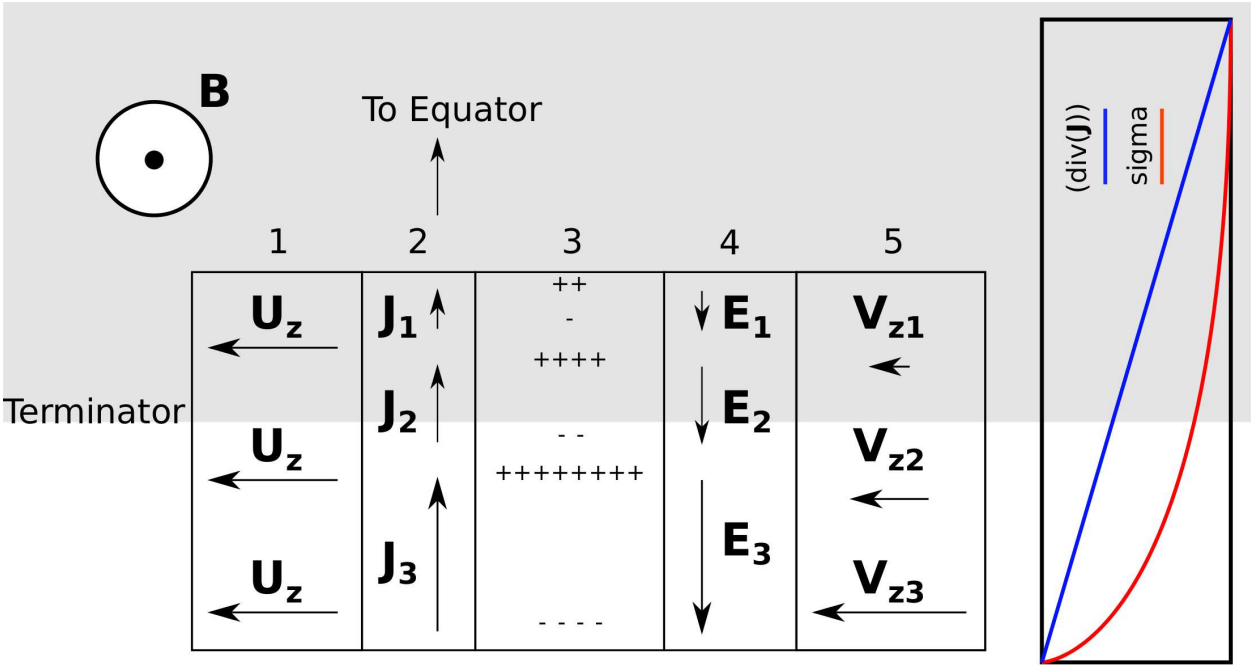

Figure 4.13: A cartoon illustrating a possible mechanism responsible for the latitudinal gradient observed in the winter zonal flows. In (1), a uniform wind blows in the vicinity of the terminator. This wind generates currents, $\mathbf{J}_i$, in the $\mathbf{U} \times \mathbf{B}$ direction. Variability in conductivity (sigma in the line plot) causes the current to not be divergence free, which causes charge accumulation. This charge accumulation generated polarization electric fields, which in turn drive $\mathbf{E} \times \mathbf{B}$ plasma drifts. These plasma drifts vary with latitude because the divergence of $\mathbf{J}$ varies with latitude, due to the nonlinearity of the conductivity profile.

F regions. Additionally, the terminator at 300 km altitude in the southern hemisphere is plotted as a vertical black line. It can be seen that F region densities are much higher in the southern hemisphere than in the north. *Burnside et al.* [1983] states that when the polarization electric field due to the dynamo effect has reached steady state, the zonal plasma drift is determined by the equation

$$V_z = \frac{\Sigma_N U_{zN} + \Sigma_S U_{zS}}{\Sigma_N + \Sigma_S} \tag{4.4}$$

where Σ is height-integrated Pedersen conductivity and the z subscript indicates zonal velocity. Following this, we argue that any polarization electric fields generated by the southern

hemisphere F region dynamo should dominate those generated by the northern hemisphere F region dynamo.

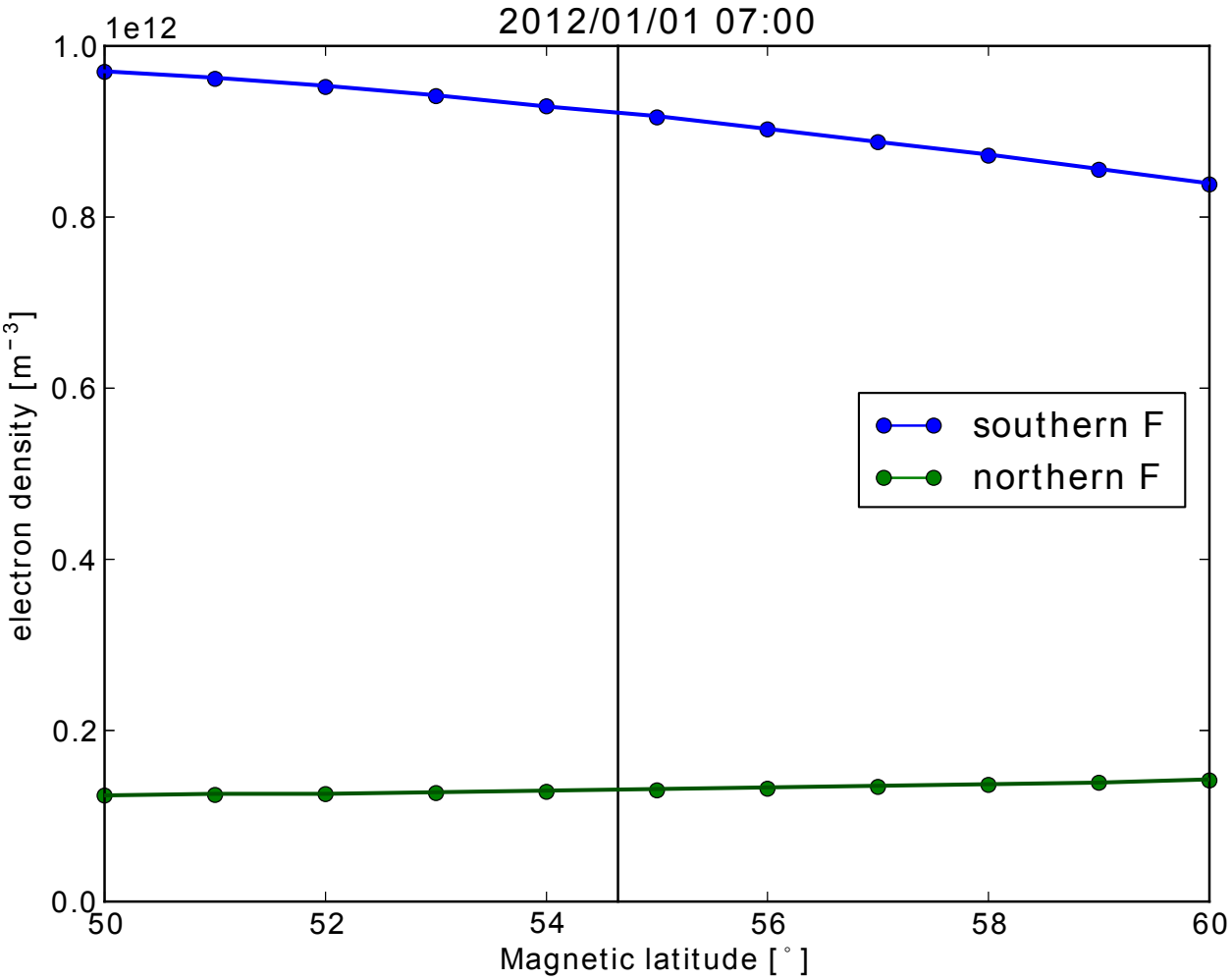

Figure 4.14: Electron densities according the the IRI model [*Bilitza*, 2001] along the 100° west meridian. The blue line shows the F region peak density in the southern hemisphere, and the green line shows the F region peak density in the northern hemisphere. The latitude of the terminator in the southern hemisphere is plotted as a vertical black line.

This IRI profile of southern hemisphere F region density opposes the mechanism which we propose could cause the latitudinal gradient in winter zonal velocities. First, electron densities are actually larger in the dark region than in the sunlit region. Additionally, the trend in electron density is linear rather than nonlinear. This could be the reality of

the situation, as the points conjugate to the North American radar fields of view lie over the Weddell Sea Anomaly, which is a region of enhanced electron density at night during southern hemisphere summer (northern winter) [*de Larquier et al.*, 2011; *Milan et al.*, 2013]. This profile could also be inaccurate due to a deficiency in IRI over the southern pole due to a lack of electron density measurements. The reality of the situation is that the physics are much more complex than what is shown in Figure 4.13, and should be studied further in future work.

4.5 Conclusions

We have presented, two-dimensional nightside quiet-time midlatitude subauroral convection patterns generated using SuperDARN data across the 52°-58° latitudinal interval. We have found that the flows are predominantly westward throughout the night. The fields associated with these flows show a significant seasonal variation, and they are largest in winter, smallest in summer, and in between during equinox. The results presented here are generally in good agreement with observations from the Millstone Hill ISR, and with empirical models generated using those results.

The broad consensus with previous empirical data that the flows should be westward throughout the night, with a maximum around midnight suggests that the electric fields responsible for the flows observed by the North American midlatitude SuperDARN radars are in fact driven by the F region dynamo. Furthermore, we argue that due to the much larger F region conductivity in the southern hemisphere than in the northern hemisphere, conjugacy effects are likely responsible for the large latitudinal gradient seen in the zonal flows in winter.

4.6 Acknowledgments

The authors thank the National Science Foundation for support under grants ATM-0849031 and ATM-0946900.

Chapter 5

Discussions/Conclusions/Future Work

Here we discuss the significance of my findings and discuss directions for future research. We review here each of the research themes in the order in which they were presented.

5.1 A realistic radar data simulator for the Super Dual Auroral Radar Network

The data simulator presented in Chapter 2 represents a powerful tool which can be used to perform several functions and the results revealed several interesting facts. First, the simulator is able to generate ACFs with the expected shape and is able to capture the inherent statistical fluctuations which are present in real data. This lends credence to the backscatter model which was used as the basis for the simulator [*Moorcroft*, 2004].

I applied the data simulator to test SuperDARN data processing algorithms, but there are

a number of other topics which could be addressed in the future using the simulator. One such study, now in process at the University of Saskatchewan, is concerned with the inherent variability in Doppler velocity within SuperDARN measurements due to the random nature of the targets. Another study which is underway is looking at the effect of cross range interference (CRI) on SuperDARN data. CRI occurs when there is range ambiguity in the pulse returns. Other work which could be performed would be to test the implementation of new pulse sequences and examining the effect of different geophysical processes on ACF shape, e.g. irregularity decay versus Doppler spectrum spread.

In addition, several further advances could be made to increase the realism of the simulator. One such advance would be to implement a more realistic model of the irregularities. The goal of the work presented here was to generate a simulator which was able to generate realistic radar data using a simple physical model. We were not, however, concerned with the detailed physics of plasma irregularities in the ionosphere. As theoretical research into instability processes progresses, particularly at midlatitudes (e.g., *Greenwald et al.* [2006]), parameters pertaining to specific types of irregularities and instabilities could be used in the simulator. This would allow for the modeling of radar returns from different types of plasma irregularities, providing insight into the viability of different instability mechanisms for generating the plasma irregularities and explaining the observations.

A more realistic ionosphere could be used in the model. In its current implementation, the simulator assumes ideal backscatter from identical scatterers in all range gates equally. This is unrealistic because, in reality, magnetic aspect conditions play an important role in determining whether the radar receives backscatter from a particular range gate. Specifically, the radar rays need to be nearly perpendicular to the background magnetic field to generate backscatter from magnetic field aligned plasma irregularities. This could be incorporated

using HF ray-tracing analysis. For example *de Larquier et al.* [2013] presented ray tracing results using SuperDARN radars and the IRI model [*Bilitza*, 2001]. By combining this type of ray-tracing model with the simulator, aspect conditions could be accurately accounted for.

Finally, the simulator has general utility beyond the specific work of SuperDARN. That is, a similar type of simulator could be used to model backscatter for different types of radars. The specific details of the implementation would have to change, but the fundamentals could be essentially the same. Specifically, the concepts of generating scatterers and sampling them in a realistic fashion would stay the same, but the scatterer model and radar implementation would have to be customized to the application. One broad category in which this might be an attractive endeavor would be to advance the ability to distinguish between radar "targets" (desired backscatter) and "clutter" (unwanted backscatter). If one is able to accurately model returns from both targets and clutter, it would then be possible to generate large quantities of data which could be used to both train and test different classification methods (e.g., support vector machines, artificial neural networks, etc.).

5.2 A comparison of SuperDARN ACF fitting methods

The analysis of ACF fitting methods presented in Chapter 3 is important not just for the SuperDARN community, but also for the space science community as a whole. In this manuscript, three different algorithms for extracting ionospheric parameters (Doppler velocity, and spectral width) were tested. It was found that there was a substantial weakness in the traditional fitting method, FITACF, which has been in use for over 20 years. This flaw

had been known about for some time and highlighted for specific extreme cases, but the current work is the first to definitively quantify the statistical significance of the problem. In recent years, two viable alternatives to FITACF have been introduced but there has been vigorous debate within the SuperDARN community regarding the pros and cons of embracing a new approach after so many years using FITACF. Although this flaw only affects data which meet the conditions of large Doppler velocity and several bad lags within the first few ACF lags, it results in extremely large errors in Doppler velocity measurements. FITACF was also shown to, on average, underestimate Doppler velocities because of this issue. Both of these new methods, FITEX2 and LMFIT, were tested, and both provided a significant improvement over FITACF. Specifically, LMFIT was shown to outperform FITEX2 for data with large spectral widths. Thus is is my recommendation that LMFIT be used as the standard SuperDARN data processing algorithm.

The improvement of SuperDARN Doppler velocity estimates is a significant result for the space science community at large. Doppler velocity is the most widely used SuperDARN data product, and since 1994, over 500 scientific papers have been published using SuperDARN data. Improving Doppler velocity estimates has the effect of improving the science done with SuperDARN.

Extraction of Doppler velocity from SuperDARN ACFs represents the first step in producing the convection patterns for which SuperDARN is well known. A byproduct of the convection map solution is a cross polar cap potential estimate. SuperDARN velocity measurements have been found by many studies to be generally smaller in magnitude than those measured by other instruments, e.g. DMSP [*Drayton et al.*, 2005; *Gillies et al.*, 2009; *Xu et al.*, 2008]. Although the effect of refractive index certainly plays a role in this discrepancy, the underestimation of Doppler velocities by FITACF may also be a contributing factor. Moving

to a new algorithm for fitting SuperDARN data with no bias in estimating magnitudes could help to partially resolve this issue.

Finally, the improvement of SuperDARN Doppler velocity estimates has the effect of improving the convection maps as well as the cross polar cap potential estimates. These factors together combine to improve the quality of science which can be done using SuperDARN.

5.3 Nightside quiet time midlatitude ionospheric plasma convection measured by the North American midlatitude SuperDARN radars

The work presented in Chapter 4 built on the work done in my Master's thesis. The analysis of nightside quiet time ionospheric plasma convection represents a significant scientific advance and provides a view of statistical midlatitude convection patterns over an interval of 52°-57° magnetic latitude. Previous work by *Baker et al.* [2007] presented a preliminary analysis of quiet time midlatitude convection but the results were inconsistent with previous studies. The data here cover two years (2011-2012) and were obtained from six North American midlatitude radars. Convection was found to be primarily westward throughout the night, with typical zonal drift velocity magnitudes in the 20-50 m/s range. Traditionally, the F region ionospheric dynamo is cited as being the dominant driver of the subauroral quiet-time electric fields observed by SuperDARN radars. The findings presented here are broadly consistent with previous studies based on data obtained by ISRs (e.g., *Richmond et al.* [1980]; *Buonsanto et al.* [1993]).

The findings we presented do, however, display some new features not present in the ISR studies. First, in the meridional flows, there is a prominent poleward (equatorward) drift post-midnight in the winter (summer) measurements. Conversely, there is an equatorward (poleward) drift pre-midnight in the winter (summer) measurements. We also identify a latitudinal gradient in zonal velocity in the winter months, with stronger flows being observed at higher latitudes. During these months, the region in the southern hemisphere conjugate to the area over which the measurements were made is both sunlit and within the Weddell Sea Anomaly. This results in the southern hemisphere having a larger F region density than the northern hemisphere according to IRI. From this, we infer that the conjugate region in the southern hemisphere has a larger Pedersen conductivity than the Northern hemisphere and any electric fields generated there by dynamo processes map to the northern hemisphere and dominate the local fields. Thus, we conclude that conditions in the southern hemisphere are the likely cause of the large latitudinal gradient observed in zonal velocities during winter in the northern hemisphere.

Next, we speculated about a mechanism which could explain the observed latitudinal gradient. The F region currents generated by the neutral winds do not necessarily satisfy the divergence free condition and a nonzero divergence leads to charge buildup and polarization electric fields. Assuming that the neutral wind and magnetic field are uniform through the conducting region, the divergence of the current should be proportional to the spatial derivative of the Pedersen conductivity. Assuming a uniform zonal neutral wind and a nonlinear increase in conductivity in the vicinity of the terminator, the divergence of the current would be larger at higher latitudes, leading to a latitudinal gradient in the polarization electric field, and thus a latitudinal gradient in the observed velocity in the same sense as that which we presented, i.e. stronger flows at higher latitudes. In the future, examination of simultaneous measurements of southern hemisphere neutral winds, electron densities, and plasma drifts

could confirm or refute the validity of this hypothesis.

Appendix A

DaViTpy: A new paradigm for data and model access and visualization

A.J. Ribeiro,[1] S. de Larquier,[1] N. A. Frissell,[1] B. S. R. Kunduri,[1] E. G. Thomas,[1] J. M. Ruohoniemi,[1] J. B. H. Baker,[1] J. Spaleta[2]

1: The Bradley Department of Electrical and Computer Engineering, Virginia Tech, Blacksburg, Virginia, USA.

2: Geophysical Institute, University of Alaska, USA.

Abstract

We present a community driven space science software package called DaViTpy. It is an open-source, Python-based module providing access to multiple data sources, multiple models and the accompanying visualization and manipulation tools relevant to each. It is still under active development to include more data, improve some aspects of user experience and add more visualization and analysis options. We encourage anyone interested to participate in the development and testing of future versions.

A.1 Introduction

Science marches forward by combining theoretical and experimental insights into reproducible and/or demonstrable concepts. Since the early days of punch-cards, computers have increasingly contributed to the scientific method. Not only have computer programs simplified complex calculations, they have opened the doors to much larger scale endeavors, from multi-scale coupled physical models to multi-instrument space-borne experiments.

As a subset of this adventure, space science is intensely data driven. To understand the ionosphere, magnetosphere and interplanetary environment, data are used to validate complex physics-based models, to build empirical models, and to drive new discoveries. Most published space science results during the past 20 or 30 years have relied on some form of computer program to record, visualize, analyze and synthesize data into meaningful insights. Some of the software developed in this process and used in published results is propagated to the community, but most never spreads further than a handful of computers in a single institution. In addition, many space science researchers lean heavily on proprietary software which requires an expensive license. New developments make it possible to do research and create publication-quality visualizations with free software

Due to the incremental nature of science in general, this process is demonstrably inefficient. However, it can be easily improved, without having to rely on unproven cutting edge technologies, by simply adopting some of the well tested practices of software engineering. Interestingly, one of the fundamental aspects of such practices is also key to all scientific results, reproducibility. By sharing and combining code built by experts in each domain, it is possible to build robust foundations to enable further discoveries.

Scientific software tools, like scientific results, should be free and open to all, easily accessible, with a transparent history. Experts should contribute their knowledge and skills to the codebase, and the community should be responsible for its maintenance and validation. Code should be generously documented and flexible, with revision and enhancement integrated in existing software rather than published as independent packages. All these criteria are fundamental, and easily enabled by existing tools and processes, such as open-source and free-software practices like distributed version control. The astronomy community has understood the value of such an effort, and has released multiple community developed software packages which continue to grow (e.g., *Hanisch and Jacoby* [2001]; *Robitaille et al.* [2013]. In space science, institutions have brought together modeling efforts, and to some extent data warehouses, but community driven software tools are very rare.

In the past year, at Virginia Tech, we have been working with members of the international SuperDARN community to develop a new Data Visualization Toolkit (DaViTpy) for the space sciences. It leverages the power of the Python programming language and robust numerical packages such as Numpy [*Oliphant*, 2006] and SciPy [*Jones et al.*, 2001]. While it started as a SuperDARN toolkit, its mission has been extended to more general space science applications. It includes modules to access data from multiple instruments (e.g., SuperDARN, POES, OMNI) and multiple geomagnetic indices (e.g., Kp, AE, Dst). It also includes several fundamental models (e.g., IRI, MSIS, HWM) kept in their original FORTRAN or C native language, but wrapped in Python to enable their use with data and other models. Finally, access to data and models would not mean as much without the visualization tools included in DaViTpy. The development is version-controlled using git and GitHub, providing a framework for clear history, contribution and feedback tracking.

The goal of this paper is to present an overview of the different aspects of DaViTpy and

demonstrate the potential benefits of such projects for the space sciences. In the following sections, we provide a description of data access (Section A.3), model integration (Section A.4) and visualization tools (Section A.5) included in DaViTpy. For each type of tool, we demonstrate use cases and discuss the potential benefits and caveats of our approach. Finally, we provide an overview of the development approach (Section A.2), a key component of DaViTpy and its potential future.

A.2 Development approach

The most essential aspect of DaViTpy's development is that it is developed by space scientists for the space science community. Every component is the product of conscientious development, peer testing and thorough documentation. It is to remain free and open-source at all times, with clear acknowledgement of all its contributors.

To enable these requirements, we rely on well-tested software engineering practices. Git and GitHub[1] are used to facilitate the distributed version control, contribution tracking and management (*a.k.a.*, pull requests), and bug reporting. The documentation is auto-generated directly from inline code docstrings, then hosted online [2]. Any new contribution to the codebase is evaluated based on its technical details as much as its documentation.

This workflow is in no way innovative, it has worked successfully for many other projects. Bug reports and pull requests are handled by the most qualified and available contributors for each specific request. This removes the need for a single code guru stretching his time and knowledge to their thinnest, thus increasing development pace and quality.

[1] http://github.com
[2] http://davit.ece.vt.edu/davitpy/

A.3 Data Integration

Obtaining data is one of the first steps in doing science. Often, just obtaining the data is a problem. Sometimes one must email a PI, specifically ask for a time period, and then wait for it to be delivered. Other times, the data is hosted on a remote FTP server, often with no documentation. Although in this paradigm access is easy, the scientist must decipher what the file actually contains. Yet another paradigm which exists is requesting data through a web form. This can be easy to use, and well documented, but there are often limits on the amount of data which can be requested at once. This means that the form often has to be submitted several times, which is a nuisance. In all of these cases, even after getting the data, the scientist must then write routines to read the data, which is tedious and time-consuming, especially since there is not a consistent file format across space science.

DaViTpy represents a paradigm shift in the way in which data is obtained. A single function is written for access to each type of data for use by the users. Instead of going and looking for data somewhere, the user simply executes a command, and the data is downloaded and read into coherent, useable objects in the environment. Take, for example, reading a period of Dst data:

```
gme.ind.dst.readDst(datetime(2011,1,1,0,0),eTime=datetime(2011,1,2,0,0))
Out[1]:
[Dst record FROM: 2011-01-01 00:00:00
info = These data were downloaded from WDC For Geomagnetism, Kyoto.  *Please be courteou
 and give credit to data providers when credit is due.*
dst = -11.0
time = 2011-01-01 00:00:00
```

```
dataSet = Dst
,
...
 Dst record FROM: 2011-01-02 00:00:00
info = These data were downloaded from WDC For Geomagnetism, Kyoto.  *Please be courteou
 and give credit to data providers when credit is due.*
dst = -1.0
time = 2011-01-02 00:00:00
dataSet = Dst
]
```

Using a single read command, we have queried the server for a day of data, located the data, and read it into a list of Dst objects. All data access within DaViTpy is handled in this manner.

Additionally, several of the datasets available within DaViTpy are stored in a NoSQL database, allowing for query operations. For example, one can read all Omni data from January of 2011 with IMF Bz values between -100 and 0 and By values between 10 and 20 with a command like so:

```
omniList = gme.ind.readOmni(sTime=datetime(2011,1,1,0,0),
                            eTime=datetime(2011,2,1,0,0),
                            bz=[-100,0],bye=[10,20])
```

Currently, the datasets which are available from the NoSQL database are SYM/ASY, AU/AL/AO/AE, Kp, OMNI, Dst, and POES. Additionally, SuperDARN data is available, but this data is

hosted on an FTP server. Note that even though the data is hosten on an FTP server, the downloading, reading, and parsing of data into objects is still done in the backend, and is no harder than reading data from the NoSQL database.

In the future, we plan to make more datasets available within DaViTpy. The beauty of the design is that data does not have to be moved to a central location, routines simply have to be written to automatically fetch the data from wherever it resides and parse it. Once those routines are incorporated into DaViTpy, any user has access to it without concern for locating and reading the data.

A.4 Model Integration

Most space science data is eventually compared to or assimilated into numerical models, whether to directly simulate the environment (e.g., *Bilitza et al.* [2011]), or as support to study other physical processes such as neutral or plasma waves. However, to the authors knowledge, there is no software package which enables easy interfacing between data and models. For this reason, DaViTpy includes several key models such as the International Reference Ionosphere (IRI), International Geomagnetic Reference Field (IGRF), Horizontal Wind Model (HWM07), Tsyganenko (T96), and more. The common approach for each model is to leave the original code almost untouched, and design a Python wrapper using either F2PY [*Peterson*, 2009] for FORTRAN-based models or the Python/C API for C/C++-based models.

This provides a single and convenient environment for data and model exploration. For example, one could read and plot an electron density profile from the Millstone Hill Incoherent

Scatter Radar, and in the next line, query IRI for the same profile. In the following code, we illustrate another example, running the Tsyganenko model to obtain conjugate locations.

```
lats = range(10, 80, 10) # latitudes: 10, 20, 30, 40, 50, 60, 70, 80
  lons = zeros(len(lats)) # longitude: 0
  rhos = 6672.*ones(len(lats)) # 300 km altitude
  trace = tsyganenko.tsygTrace(lats, lons, rhos) # trace field lines and find conjugate
  print trace # print results
  ax = trace.plot() # plot traced field lines
```

In the case of the Tsyganenko model illustrated in the above code, we are working on integrating more recent versions of the model, but the interface will remain the same, providing a high level of abstraction, while preserving the possibility to dive down to the low-level FORTRAN subroutines, while remaining in the Python environment. It is also worth highlighting that this model integration approach comes at no additional cost to the model developers while bringing great benefits to the model users.

A.5 Visualization

Data visualization is often a critical part of scientific analysis. DaViTpy does this by heavily utilizing the python library Matplotlib [*Hunter*, 2007]. Our goal when developing the visualization routines was to keep it as simple as possible while simultaneously remaining incredibly flexible. We achieve this goal by modularizing all of the routines. Consider, for example, the plot shown in Figure A.1. This figure shows data from two SuperDARN

radars, as well as POES total energy detector data overlaid [*Rodger et al.*, 2010]. This plot is generated with a single command:

```
pydarn.plotting.fan.plotFan(datetime(2012,5,13,8,0),['bks','fhw'],
overlayPoes=True),
```

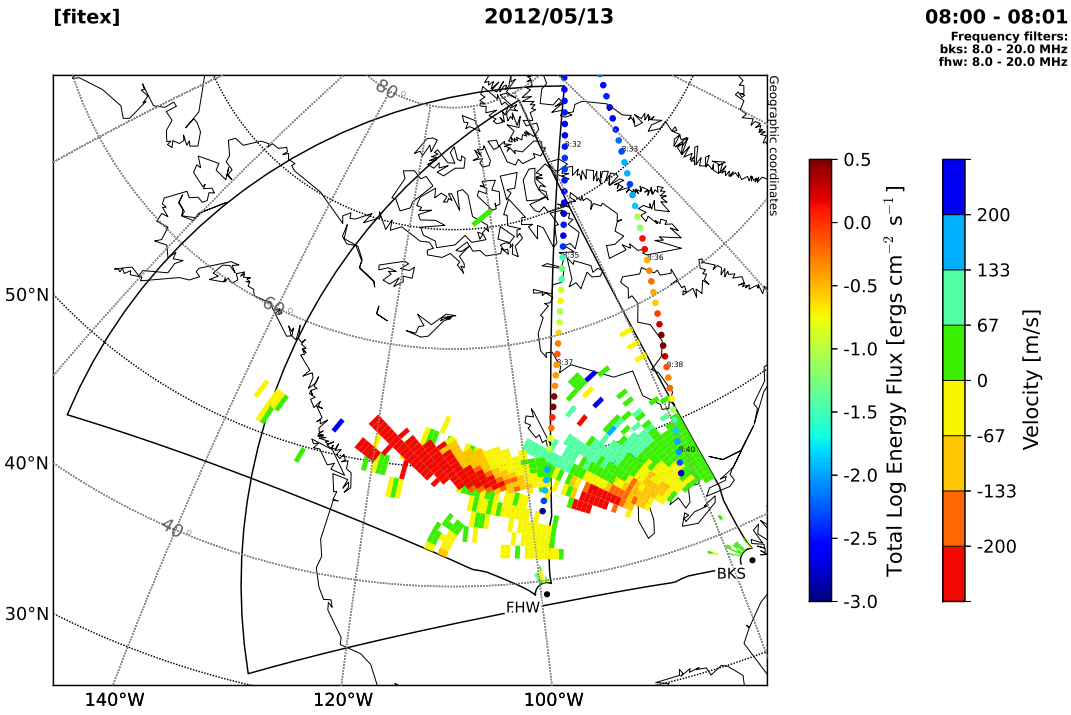

Figure A.1: An example of a plot generated using DaViTpy. The colored rectangles show SuperDARN Doppler velocity, and the colored circles are POES TED measurements.

Several routines are utilized in the creation Figure A.1, hidden behind this simple line of code. First, a single routine is called in order to draw the map. Another routine is then called to overlay the SuperDARN data. A third routine is called to overlay the POES satellite data.

There are several advantages to this type of design. First, a fairly generic, but nevertheless robust, plot can be generated with a single command. Second, it provides a framework for the incorporation of new datasets. For example, if a new satellite dataset were to be incorporated, an overlay routine could be written, and this routine could just be woven into the overarching single plot command. Third, it allows for a lot of flexibility when one is developing figures for publication. When preparing these types of figures, the ability to fully customize plots is often desirable. In the DaViTpy paradigm, the scientist would have this ability because instead of calling a single, overarching routine with options, they could call the background routines one by one in order to pick and choose what gets plotted and how.

Another example of SuperDARN data visualization is shown in Figure A.2. This is a SuperDARN Range-Time Intensity (RTI) plot, which shows Doppler velocity in the top colored panel, backscatter power in the middle panel, and spectral width in the bottom panel. This again was generated using a single command, which makes use of several plotting subroutines. In general, if a type of plot can be done very simply using the routines in matplotlib, we have not implemented separate routines for plotting. In the future, we would like to be able to include and visualize more datasets alongside those which are already present.

A.6 Conclusions

We have presented a community developed space science software package, and described its main functionalities, which include:

- data access: SYM/ASY, AU/AL/AO/AE, Kp, OMNI, Dst, POES and SuperDARN
- model access: IGRF, IRI, MSIS, HWM, T96 and AACGM

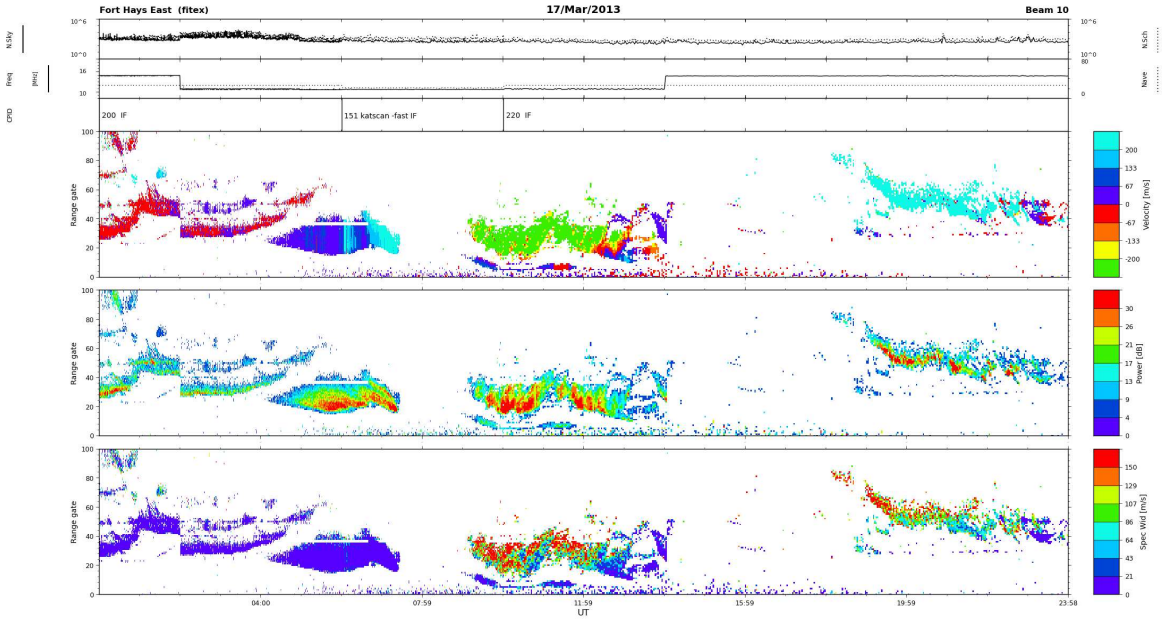

Figure A.2: An example of a SuperDARN RTI plot generated using DaViTpy. The top colored panel shows Doppler velocity, the middle panel shows backscatter power, and the bottom panel shows spectral width.

- visualization: each data source, model and coordinate system includes an associated set of plotting tools

While DaViTpy provides all of these very useful tools, its most important strength relies on its development model. DaViTpy has relied on an international collaboration to develop and test these tools. Future plans are currently being discussed to involve other institutional software packages in this community driven development effort.

We invite members of the community to join the effort by adopting the DaViTpy package for their own projects, reporting any issues, and whenever possible, developing new functionality.

A.7 Acknowledgments

The authors thank the National Science Foundation for support under grants ATM-0849031 and ATM-0946900.

Appendix B

References

André, R., M. Pinnock, and A. S. Rodger (1999), On the SuperDARN autocorrelation function observed in the ionospheric cusp, *Geophysical Research Letters*, *26*(22), 3353–3356, doi:10.1029/1999GL003658.

Angerami, J., and D. L. Carpenter (1966), Whistler studies of the plasmapause in the magnetosphere 2. electron density and total tube electron content near the knee in magnetospheric ionization, *Journal of Geophysical Research*, *71*(3), 711–725.

Ascher, D., P. F. Dubois, K. Hinsen, J. Hugunin, and T. Oliphant (1999), *Numerical Python*, Lawrence Livermore National Laboratory, Livermore, CA, ucrl-ma-128569 ed.

Baker, J., R. Greenwald, J. Ruohoniemi, K. Oksavik, J. Gjerloev, L. Paxton, and M. Hairston (2007), Observations of ionospheric convection from the wallops superdarn radar at middle latitudes, *Journal of Geophysical Research*, *112*(A1), doi:10.1029/2006JA011982.

Baker, K., R. Greenwald, A. Walker, P. Bythrow, L. Zanetti, T. Potemra, D. Hardy, F. Rich, and C. Rino (1986), A case study of plasma processes in the dayside cleft, *Journal of Geophysical Research*, *91*(A3), 3130–3144, doi:10.1029/JA091iA03p03130.

Baker, K. B., J. R. Dudeney, R. A. Greenwald, M. Pinnock, P. T. Newell, A. S. Rodger, N. Mattin, and C. I. Meng (1995), HF radar signatures of the cusp and low-latitude boundary layer, *Journal of Geophysical Research*, *100*(A5), 7671–7695, doi:10.1029/94JA01481.

Barthes, L., R. André, J. C. Cerisier, and J. P. Villain (1998), Separation of multiple echoes using a high-resolution spectral analysis for SuperDARN HF radars, *Radio Science*, *33*(4), 1005–1017, doi:10.1029/98RS00714.

Bendat, J. S., and A. G. Piersol (1986), *Random data. Analysis and measurement procedures*, John Wiley & Sons, Inc., New York, Chichester, Brisbane, Toronto and Singapore.

Bilitza, D. (2001), International reference ionosphere 2000, *Radio Science*, *36*(2), 261–275.

Bilitza, D., L.-A. McKinnell, B. Reinisch, and T. Fuller-Rowell (2011), The international reference ionosphere today and in the future, *Journal of Geodesy*, *85*(12), 909–920, doi: 10.1007/s00190-010-0427-x.

Blanchard, G. T., S. Sundeen, and K. B. Baker (2009), Probabilistic identification of high-frequency radar backscatter from the ground and ionosphere based on spectral characteristics, *Radio Science*, *44*(5), RS5012.

Buonsanto, M., M. Hagan, J. Salah, and B. G. Fejer (1993), Solar cycle and seasonal variations in f region electrodynamics at millstone hill, *Journal of Geophysical Research*, *98*(A9), 15,677–15,683, doi:10.1029/93JA01187.

Burnside, R., J. Walker, R. Behnke, and C. Gonzales (1983), Polarization electric fields in the nighttime f layer at arecibo, *Journal of Geophysical Research*, *88*(A8), 6259–6266, doi:10.1029/JA088iA08p06259.

Chapman, S. (1931), The absorption and dissociative or ionizing effect of monochromatic radiation in an atmosphere on a rotating earth, *Proc. Phys. Soc.*, *43*, 26 -45.

Chisham, G., et al. (2007), A decade of the Super Dual Auroral Radar Network (SuperDARN): Scientific achievements, new techniques and future directions, *Surveys in Geophysics*, *28*(1), 33–109, doi:10.1007/s10712-007-9017-8.

de Larquier, S., J. Ruohoniemi, J. Baker, N. R. Varrier, and M. Lester (2011), First observations of the midlatitude evening anomaly using super dual auroral radar network (superdarn) radars, *Journal of Geophysical Research*, *116*(A10), A10,321.

de Larquier, S., P. Ponomarenko, A. Ribeiro, J. Ruohoniemi, J. H Baker, K. Sterne, and M. Lester (2013), On the spatial distribution of decameter–scale subauroral ionospheric irregularities observed by superdarn radars, *Journal of Geophysical Research*, doi:10.1002/jgra.50475.

Drayton, R., A. Koustov, M. Hairston, J.-P. Villain, et al. (2005), Comparison of dmsp cross-track ion drifts and superdarn line-of-sight velocities, in *Annales Geophysicae*, vol. 23, pp. 2479–2486.

Dubois, P. F., K. Hinsen, and J. Hugunin (1996), Numerical python, *Computers in Physics*, *10*(3).

Farley, D. (1972), Multiple-pulse incoherent-scatter correlation function measurements, *Radio Science*, *7*(6), 661–666, doi:10.1029/RS007i006p00661.

Fejer, B. G. (1991), Low latitude electrodynamic plasma drifts: A review, *Journal of Atmospheric and Terrestrial Physics*, *53*(8), 677–693.

Fejer, B. G. (1993), F region plasma drifts over arecibo: Solar cycle, seasonal, and magnetic activity effects, *Journal of Geophysical Research: Space Physics (1978–2012)*, *98*(A8), 13,645–13,652, doi:10.1029/93JA00953.

Fejer, B. G., and M. Kelley (1980), Ionospheric irregularities, *Reviews of Geophysics*, *18*(2), 401–454.

Gillies, R., G. Hussey, G. Sofko, K. McWilliams, R. Fiori, P. Ponomarenko, and J.-P. St-Maurice (2009), Improvement of superdarn velocity measurements by estimating the index of refraction in the scattering region using interferometry, *Journal of Geophysical Research: Space Physics (1978–2012)*, *114*(A7).

Greenwald, R. A., K. B. Baker, R. A. Hutchins, and C. Hanuise (1985), An HF phased-array radar for studying small-scale structure in the high-latitude ionosphere, *Radio Science*, *20*(1), 63–79, doi:10.1029/RS020i001p00063.

Greenwald, R. A., K. Oksavik, P. J. Erickson, F. D. Lind, J. M. Ruohoniemi, J. B. Baker, and J. W. Gjerloev (2006), Identification of the temperature gradient instability as the source of decameter-scale ionospheric irregularities on plasmapause field lines, *Geophysical research letters*, *33*(18), L18,105, doi:10.1029/2006GL026581.

Greenwald, R. A., K. Oksavik, R. Barnes, J. M. Ruohoniemi, J. Baker, and E. R. Talaat (2008), First radar measurements of ionospheric electric fields at sub-second temporal resolution, *Geophys. Res. Lett.*, *35*, L03,111, doi:10.1029/2007GL032164.

Hanisch, R. J., and G. H. Jacoby (2001), Astronomical Data Analysis Software and Systems X, *Publications of the Astronomical Society of the Pacific*, *113*(784), 772–773, doi:10.1086/320803.

Hanuise, C., J. P. Villain, D. Gresillon, B. Cabrit, R. A. Greenwald, and K. B. Baker (1993), Interpretation of HF radar ionospheric Doppler spectra by collective wave scattering theory, *Annales Geophysicae*, *11*(1), 29–39.

Hosokawa, K., T. Iyemori, A. S. Yukimatu, and N. Sato (2001), Source of field-aligned irregularities in the subauroral f region as observed by the superdarn radars, *Journal of Geophysical Research*, *106*(A11), 24,713–24,731, doi:10.1029/2001JA900080.

Hudson, M. K., and M. C. Kelley (1976), The temperature gradient drift instability at the equatorward edge of the ionospheric plasma trough, *Journal of Geophysical Research*, *81*(22), 3913–3918, doi:10.1029/JA081i022p03913.

Hunter, J. D. (2007), Matplotlib: A 2d graphics environment, *Computing In Science & Engineering*, *9*(3), 90–95.

Jones, E., T. Oliphant, P. Peterson, et al. (2001), SciPy: Open source scientific tools for Python.

Kelley, M. C. (2009), *The Earth's Ionosphere: Plasma Physics and Electrodynamics*, 2nd ed., Academic Press, Burlington, MA.

Keskinen, M. J., and S. Ossakow (1983), Theories of high-latitude ionospheric irregularities: A review, *Radio science*, *18*(6), 1077–1091, doi:10.1029/RS018i006p01077.

Lehtinen, M. S. (1986), *Statistical theory of incoherent scatter radar measurements*, EISCAT Scientific Ass.

Levenberg, K. (1944), A method for the solution of certain problems in least squares, *Quart. Applied Math*, *2*, 164–168.

Markwardt, C. B. (2009), Non-linear least-squares fitting in IDL with MPFIT, *Astron. Soc. Pac. Conf. Ser.*, *411*, 251–254.

Marquardt, D. W. (1963), An algorithm for least-squares estimation of nonlinear parameters, *Journal of the Society for Industrial and Applied Mathematics*, *11*(2), 431–441.

Milan, S., A. Grocott, S. Larquier, M. Lester, T. Yeoman, M. Freeman, and G. Chisham (2013), Traveling ionospheric disturbances in the weddell sea anomaly associated with geomagnetic activity, *Journal of Geophysical Research: Space Physics*.

Moorcroft, D. (2004), The shape of auroral backscatter spectra, *Geophysical research letters*, *31*(9), doi:10.1029/2003GL019340.

Mozer, F. (1973), Electric fields and plasma convection in the plasmasphere, *Reviews of Geophysics*, *11*(3), 755–765, doi:10.1029/RG011i003p00755.

Oliphant, T. E. (2006), *Guide to NumPy*, Provo, UT.

Peterson, P. (2009), F2PY: a tool for connecting Fortran and Python programs, *International Journal of Computational Science and Engineering*, *4*(4), 296, doi:10.1504/IJCSE.2009.029165.

Ponomarenko, P. V., and C. L. Waters (2006), Spectral width of SuperDARN echoes: measurement, use and physical interpretation, *Annales Geophysicae*, *24*(1), 115–128, doi:10.5194/angeo-24-115-2006.

Ponomarenko, P. V., C. L. Waters, and F. W. Menk (2007), Factors determining spectral width of HF echoes from high latitudes, *Ann. Geophys.*, *25*, 675–687, doi:10.5194/angeo-25-675-2007.

Ponomarenko, P. V., C. L. Waters, and F. W. Menk (2008), Effects of mixed scatter on SuperDARN convection maps, *Annales Geophysicae*, *26*(6), 1517, doi:10.5194/angeo-26-1517-2008.

Press, W. H., S. A. Teukolsky, W. T. Vetterling, and B. P. Flannery (1992), *Numerical recipes in C: the art of scientific computing*, 2nd ed., Cambridge University Press, New York, NY.

Ribeiro, A., J. Ruohoniemi, J. Baker, L. Clausen, R. Greenwald, and M. Lester (2012), A survey of plasma irregularities as seen by the midlatitude blackstone superdarn radar, *Journal of Geophysical Research: Space Physics (1978–2012)*, *117*(A2), doi: 10.1029/2011JA017207.

Ribeiro, A., J. Ruohoniemi, P. Ponomarenko, L. N Clausen, J. H Baker, R. Greenwald, K. Oksavik, and S. Larquier (2013a), A comparison of superdarn acf fitting methods, *Radio Science*.

Ribeiro, A., P. Ponomarenko, J. Ruohoniemi, J. Baker, L. Clausen, R. Greenwald, and S. Larquier (2013b), A realistic radar data simulator for the super dual auroral radar network, *Radio Science*.

Ribeiro, A. J., J. M. Ruohoniemi, J. B. H. Baker, L. B. N. Clausen, S. de Larquier, and R. A. Greenwald (2011), A new approach for identifying ionospheric backscatter in midlatitude SuperDARN HF radar observations, *Radio Science*, *46*(4), RS4011, doi: 10.1029/2002JD003026.

Richmond, A., S. Matsushita, and J. Tarpley (1976), On the production mechanism of electric currents and fields in the ionosphere, *Journal of Geophysical Research*, *81*(4), 547–555, doi:10.1029/JA081i004p00547.

Richmond, A., et al. (1980), An empirical model of quiet-day ionospheric electric fields at middle and low latitudes, *Journal of Geophysical Research*, *85*(A9), 4658–4664, doi: 10.1029/JA085iA09p04658.

Richmond, A., E. Ridley, and R. Roble (1992), A thermosphere/ionosphere general circulation model with coupled electrodynamics, *Geophysical Research Letters*, *19*(6), 601–604, doi:10.1029/92GL00401.

Rishbeth, H. (1971), The *F*-layer dynamo, *Planetary and Space Science*, *19*(2), 263–267.

Rishbeth, H., and O. K. Garriott (1969), *Introduction to Ionospheric Physics*, Academic Press, New York.

Robitaille, T. P., et al. (2013), Astropy: A community Python package for astronomy, *Astronomy & Astrophysics*, *558*, A33, doi:10.1051/0004-6361/201322068.

Roble, R., E. C. Ridley, A. Richmond, and R. Dickinson (1988), A coupled thermosphere/ionosphere general circulation model, *Geophysical Research Letters*, *15*(12), 1325–1328, doi:10.1029/GL015i012p01325.

Rodger, C. J., M. A. Clilverd, J. C. Green, and M. M. Lam (2010), Use of poes sem-2 observations to examine radiation belt dynamics and energetic electron precipitation into the atmosphere, *Journal of Geophysical Research*, *115*(A4), A04,202, doi:10.1029/2008JA014023.

Ruohoniemi, J., and K. Baker (1998), Large-scale imaging of high-latitude convection with super dual auroral radar network hf radar observations, *Journal of Geophysical Research: Space Physics (1978–2012)*, *103*(A9), 20,797–20,811, doi:10.1029/98JA01288.

Rytov, S. M., Y. A. Kravtsov, and V. I. Tatarskii (1988), *Principles of Statistical Radiophysics, Vol. 2, Wave Propagation Through Random Media*, Springer-Verlag, New York, NY.

Schunk, R., and A. Nagy (2009), *Ionospheres*, Cambridge University Press, Cambridge, UK.

Skolnik, M. L. (2001), *Introduction to radar systems*, 3rd ed., McGraw-Hill, New York, NY.

Sterne, K. T. (2010), Testing the re-designed superdarn hf radar and modeling of a twin terminated folded dipole array, Ph.D. thesis, Virginia Polytechnic Institute and State University.

Tsunoda, R. T. (1988), High-latitude f region irregularities: A review and synthesis, *Reviews of Geophysics*, *26*(4), 719–760, doi:10.1029/RG026i004p00719.

Tsyganenko, N. (1995), Modeling the earths magnetospheric magnetic field confined within a realistic magnetopause, *Journal of Geophysical Research*, *100*(A4), 5599–5612, doi:10.1029/94JA03193.

Uppala, S. V., and J. D. Sahr (1994), Spectrum estimation of moderately overspread radar targets using aperiodic transmitter coding, *Radio science*, *29*(3), 611–623, doi:10.1029/94RS00328.

Villain, J., R. André, C. Hanuise, and D. Grésillon (1996), Observation of the high latitude ionosphere by hf radars: Interpretation in terms of collective wave scattering and characterization of turbulence, *Journal of Atmospheric and Terrestrial Physics*, *58*(8), 943–958, doi:10.1016/0021-9169(95)00125-5.

Wand, R. H. (1981), A model representation of the ionospheric electric field over millstone hill (λ= 56), *Journal of Geophysical Research*, *86*(A7), 5801–5808, doi:10.1029/JA086iA07p05801.

Xu, L., A. Koustov, J. Xu, R. Drayton, and L. Huo (2008), A 2-d comparison of ionospheric convection derived from superdarn and dmsp measurements, *Advances in Space Research*, *42*(7), 1259–1266.